Energetics of Small Molecules and Molecular Fragments on Model Catalyst Surfaces: Adsorption Calorimetry on Pt(111) and Cu(111)

Griffin Ruehl

A dissertation

submitted in partial fulfillment of the

requirements for the degree of

Doctor of Philosophy

University of Washington

2022

Reading Committee:

Charles T. Campbell, Chair

Eric Stuve

David Castner

Program Authorized to Offer Degree:

Chemical Engineering

University of Washington

Abstract

Energetics of Small Molecules and Molecular Fragments on Model Catalyst Surfaces: Adsorption Calorimetry on Pt(111) and Cu(111)

Griffin Ruehl

Chair of the Supervisory Committee:
Professor Charles T. Campbell
Chemical Engineering

Heterogeneous catalysis is essential for the development and support of modern society, with the vast majority of chemical production processes reliant on catalysts. New catalysts and catalytic reactions constitute promising pathways forward in combatting the effects of climate change and transitioning human society off of our reliance on fossil fuels. However, there is an absence of a complete fundamental understanding of observed differences and trends in catalytic behavior that impedes the rapid, strategic development of new catalytic processes.

Computational modeling methods, such as Density Functional Theory (DFT), constitute powerful tools for the rapid screening of catalyst materials, but these methods have large errors in energy accuracy which severely limit their quantitative predictive abilities. These methods are dependent on experimentally determined benchmarks to guide modifications for improving their energy accuracy. The technique of single crystal adsorption calorimetry (SCAC) is uniquely able to study the energetics of irreversible adsorption processes on well-defined surface sites. SCAC

can therefore provide these key benchmarks and fundamental understandings of the energetics of molecular and dissociative adsorption into molecular fragments and other key surface reaction intermediates commonly seen in industrial catalytic applications.

This dissertation presents experimental SCAC results for the study of the energetics of adsorption of small molecules and molecular fragments on model catalyst surfaces, namely Pt(111) and Cu(111). This work builds upon previous efforts from the Campbell group to develop a systematic understanding of trends and observed differences in catalytic behavior on late-transition metal catalysts. Additionally, by employing models recently developed by this group, we are able to estimate the adhesion energies of liquid solvents to clean, single-crystal metal surfaces from the experimental calorimetry results. This allows for the estimation of the effects of each solvent on the energetics of adsorption and desorption for surface reactants and intermediates of interest.

The study of the energetics of acetonitrile and *n*-decane adsorption on Pt(111), two solvents of particular interest, are reported here. Acetonitrile an important solvent due to its unique, desirable properties which make it of particular interest for electrochemical applications and the engineering of mixed solvent environments. *n*-Decane is similarly of interest in catalysis as linear alkanes of that and similar size are commonly used as solvents in catalytic reactions over Pt-group metals. From the experimentally determined heat of adsorption versus coverage we estimate adhesion energies of these liquid solvents to the Pt(111) surface to be E_{adh} = 0.198 J/m^2 for acetonitrile and E_{adh} = 0.148 J/m^2 for *n*-decane. Additionally, the adhesion energy of liquid formic acid to Cu(111) is estimated to be E_{adh} = 0.271 J/m^2. These values can be used to quantify the solvent effects of these species on the local surface reaction environment.

The calorimetrically measured heats of adsorption versus coverage are reported here for acetonitrile on Pt(111) at 100 K and 180 K, *n*-decane adsorption on Pt(111) at 150 K, azulene adsorption on Pt(111) at 150 K, and for both the molecular and dissociative adsorption of formic acid on clean and oxygen-precovered Cu(111). In combination with previously reported experimental results and DFT simulations of these systems, a number of important fundamental insights are drawn. The analysis of the *n*-decane heats of adsorption in comparison to a previous TPD study of shorter linear alkanes extends the observed trends to larger species such as *n*-decane that desorb irreversibly. Namely, we report that the adsorption energy increases nearly proportionally to carbon number, and the adhesion energy remains nearly constant (for a given surface).

Naphthalene and azulene are of particular interest as representative molecules for the regular structure of graphene and the most common defect found in graphene sheets, respectively. Therefore the study of their adsorption energetics can inform experimental and computational systems involving graphene more broadly. Comparison of the heats of adsorption for azulene on Pt(111) first presented here with previous results for naphthalene and DFT simulations of both show that azulene binds significantly stronger to Pt(111) (by ~100 kJ/mol) than its isomer naphthalene. We show that DFT accurately predicts the adsorption energy of azulene but overestimates the binding energy of naphthalene, indicating that DFT is not accurately modeling the energy differences between these two systems.

We report here the dissociative adsorption of formic acid on oxygen-precovered Cu(111), which results in the formation of adsorbed bidentate formate and gaseous water at 240 K. Formic acid and formate are common intermediates in a variety of reactions on late transition metals, ranging from well-established industrial reactions to emergent clean energy technologies. From

the heats of this dissociative adsorption reaction, we extract a bond enthalpy of bidentate formate to Cu(111) of 335 kJ/mol, and an enthalpy of formation of bidentate formate on Cu(111) of -465 kJ/mol. We show that these enthalpies are slightly greater than those on Ni(111) (by ~15 kJ/mol) and significantly greater than those on Pt(111) (by ~85 kJ/mol). This is in opposition to the predicted order of bond strength from DFT, where Ni is predicted to bind formate more strongly than Cu, and indicates that DFT is not accurately modeling this trend in adsorption between these three surfaces. This study also constitutes the first experimental measurement of the energetics of *any* adsorbed molecular fragment on *any* Cu surface. In comparison to previous results on Pt(111) and Ni(111) this allows for the direct comparison of a single molecular fragment on all three surfaces for the first time. This forms a suite of key experimental benchmarks for improving the energy accuracy of computational models like DFT, as well as crucial fundamental insights into trends and observed differences in catalysis on late-transition metal surfaces.

Lastly, we report a detailed kinetics study of the aqueous-phase hydrogenation of phenol and benzaldehyde on Pt, Pd, and Rh using small-scale thermal and electrocatalytic reactors. These molecules represent common intermediates in the process of breaking down biomass and converting its constituents into biofuels and other value-added chemicals. This work shows that the observed catalytic behavior is well fit by a Langmuir-Hinshelwood mechanism with competitive adsorption (organic versus hydrogen adsorption) on terrace, or (111)-like, sites. Additionally, we report that adsorbed benzaldehyde inhibits the formation of a bulk Pd-hydride whereas phenol does not, explaining the extreme differences in observed catalytic activity between these two systems. This work informs efforts to correlate molecular structure of biomass intermediates of interest with catalytic activity on late-transition metal catalysts.

Table of Contents

List of Figures

List of Tables

Acknowledgements

First off, I would like to thank my advisor and mentor, Dr. Charles T. Campbell, for his support, assistance, and guidance throughout my graduate school experience. I would like to thank all of my committee members, Dr. Eric Stuve, Dr. Dave Castner, and Dr. Oscar Vilches for their additional support. I would like to thank Dr. Spencer Carey for training me on the calorimeter in a particularly short length of time. I would like to thank Elizabeth Harman for her collaboration in the experimental SCAC work; her collaboration, support, and encouragement have been invaluable over the last few years of working together and it has been an absolute pleasure. I would like to thank the rest of the Campbell group members, Dr. Jack Rumptz, Nida Janulaitis, Dr. Kun Zhao, Dr. Spencer Carey, Dr. Wei Zhang, Dr. Zhongtian Mao, and Dr. Wei Zhao. They have each provided immense support, advice, guidance, and, when necessary, commiseration to help carry me through my studies. I would like to thank the folks of the UW Chemistry Department's electronics shop, namely Lon Buck, Bill Beaty, and Rachel Huffman. I have come to each of you many times with a problem and no clue how to fix it, and you have ceaselessly helped figure out a solution. I would like to thank the folks of the UW Chemistry Department's machine shop as well, namely Eric Strakbein, Brian Wadey, and Kevin Soderlund for their assistance with repairs and custom solutions for the instrument. I would like to thank Loch Hickok and the rest of the folks in the chemistry store for their help and guidance in more things than I can list here. I would like to thank Jim Gladden for all of the work that he did to write, standardize, and update our data analysis program. And finally, I would like to thank my parents, Toni & Marty, my sisters Jessica & Janel, and my fiancée Tyler for their unending support that truly carried me through graduate school. I would not be where and who I am today without all of you, and I am truly indebted to each and every one of you.

Chapter 1 Introduction

Heterogeneous catalysis is fundamental to modern society and civilization, with approximately 90% of chemical production processes relying on catalysts[1]. Agriculture and food production is reliant on the catalyzed production of fertilizer, the energy sector relies on catalysis for fuel refining, pollution mitigation relies on catalysts to trap and react pollutants, and chemical production processes ranging from household plastics to industrial solvents require catalysts in order to be feasible and economically profitable[1–7]. The development of the Haber-Bosch catalytic process for fertilizer production in the early 20th century propelled society beyond previously perceived sustainability limits, and by a century later half of the world population is sustained by Haber-Bosch nitrogen[8].

Human civilization now finds itself at a similar precipice of sustainability, with the rapid accumulation of greenhouse gasses as a result of our reliance on fossil fuels for running modern society[9]. As the effects of climate change quickly worsen, the development of sustainable new pathways for our energy and transportation infrastructures are crucial. Again, catalysis holds an immense amount of promise for sustainable paths forward via the development of new catalysts and catalytic processes. However, historically catalysts have been developed largely through trial-and-error methods[10–12], a time-consuming process that is compounded by the complexity of reaction chemistries required by next-generation clean energy technologies. The absence of a complete, fundamental understanding of the basis for observed differences in catalytic activity amongst different transition metal catalysts and reaction pathways further inhibits efforts to rapidly develop new processes. The bond strengths of a few important catalytic intermediates and transition states to the metal catalyst surface constitute the most important parameters for understanding desired catalyst properties such as activity, selectivity, and poison resistance.

Consequently, fundamental energetic measurements such as bond energies of surface adsorbates and enthalpies of formation of reactants and intermediates on catalyst surfaces are crucial to elucidating surface phenomena and in turn building a systematic understanding of catalyst efficacy for desired chemistries. Additionally, as electrocatalytic and other liquid-phase heterogeneous catalytic processes continue to show promise for new catalytic pathways, fundamental measurements that elucidate solvent effects such as the adhesion energy to the catalyst surface are increasingly valuable.

Within the last few decades, computational modeling methods, primarily Density Functional Theory (DFT), have arisen as a powerful tool for the aims of both rapidly screening potential new catalysts and systematically understanding trends in catalytic activity[13–20]. However, these tools have well known large errors in energy accuracy, which severely inhibit the predictive abilities of these methods[21]. Further, the accuracy required for these methods to be quantitatively exact is extremely demanding. When one considers that an error of 20 kJ/mol in the rate limiting step of a 400 °C reaction translates to a 400-fold error in the predicted reaction rate, common margins of error in energy accuracy on the order of 20-60 kJ/mol are really quite debilitating[21]. The truly transformative capabilities of these computational methods continue to be limited by these errors, and in the absence of any computational techniques that provide the desired accuracy must rely on experimental measurements for benchmarks.

These experimental measurements of fundamental energetic values are therefore crucial to improving the energy accuracy of these computational methods. Efforts to this aim have long outdated these computational developments, such as Temperature Programmed Desorption (TPD). These traditional methods access the energetics of adsorption indirectly (often via studying desorption), which requires that adsorption and desorption are reversible processes[22].

However, it is most often the energetics of molecular fragments and other reaction intermediates on the catalyst surface that are most valuable as benchmarks and fundamental insights, and the vast majority of these species require dissociation or other irreversible adsorption processes for their formation.

In order to be able to study the energetics of these irreversible adsorption processes, Sir David King pioneered the first single crystal adsorption calorimeter (SCAC) in the 1990's[23,24], which continues to be the only technique that is able to perform these measurements. While powerful in the access it provided to study new systems of interest, the original instrument was constrained by design limitations that restricted possible systems to high vapor pressure molecules and a narrow range of experimental temperatures. The temperature accuracy of the calorimeter was also limited by the use of an optical pyrometer as the heat detector. Since then, a number of instrumental improvements have been developed, including by the Campbell group which most notably pioneered the use of a pyroelectric, β-poly(vinylidene fluoride) ribbon pressed gently against the back of the sample as the heat detector[25]. This improved the sensitivity in temperature by orders of magnitude, and enabled a much wider range of experimental conditions down to cryogenic temperatures[25,26]. Additionally, the development of a molecular beam used for low vapor pressure molecules greatly expanded the range of potential adsorbates to study[26]. This improved instrument is employed in the experiments described in this dissertation. More details about the specifics of the instrument and experimental techniques can be found in **Chapter 2**.

This technique revolves around the use of single crystals, which offer a number of advantages over powdered or polycrystalline alternatives that mirror the more complex structures of commercial catalysts used in industrial applications. The simplified surface structure and

homogeneity of surface sites makes it much easier to determine and analyze the structure and chemistry of adsorbates on the catalyst surface. Additionally, they constitute the most direct experimental comparison to theoretical models, since the most accurate DFT techniques utilize periodic boundary conditions, as are intrinsic to extended single crystal surfaces. By eliminating the effects of varying heterogeneous catalyst surface structures and supports, these model catalyst systems can provide deep fundamental insights in order to elucidate trends in surface reactivity on a broad scale across transition metal catalysts. Further, the (111) crystal facet is used as the model catalyst here, since it is the most thermodynamically stable and therefore dominates the surface of catalysts as long as the metal catalyst particles are sufficiently large.

Efforts by the Campbell group over the last few decades have utilized this technique to greatly expand both fundamental systematic understandings of late transition metal catalysts as well as construct databases of experimental benchmarks for computational models[21,27,36–41,28–35]. Prior to this work, experimental measurements of the energetics of molecular fragments and other irreversibly adsorbed species on transition metal catalyst surfaces were limited almost entirely to Pt(111). Consequently, these efforts have focused on expanding these measurements to other surfaces, namely Ni(111) and Cu(111). These two surfaces were chosen due to that fact that, in addition being commonly used in industrial catalysis, DFT models predict these surfaces to show large differences in adsorbate bond energies in comparison to Pt and each other. Therefore, the collection of these three surfaces constitute catalyst metals that are sufficiently different to elucidate trends over a wide range of desired reactions on a variety of transition metal catalysts, but not so different as to be irrelevant to common industrial applications. The main suite of adsorbates selected for study on these surfaces were strategically chosen to represent the simplest examples of a variety of the most common surface fragments, including

hydroxyls, alkoxys, carboxylates, alkyls, and carbynes. These are formed via the dissociative adsorption of water, methanol, formic acid, and methyl iodide (and further dissociation of adsorbed methyl in the case of carbynes).

In addition to quantifying the energetics of the adsorption of reactants and intermediates on the surface of the catalyst, the growing importance of electrocatalysis and liquid-phase heterogeneous catalytic systems has driven an interest in elucidating the energetics of solvent molecule adsorption to these surfaces. In these applications, adsorption of the reactant or intermediate of interest is often in competition with the solvent and requires the displacement of solvent molecules from the surface in order to free up a site for adsorption. Consequently, the strength of these solvent/catalyst interactions can directly alter the reaction environment and the energetics of adsorption for reactants and intermediates of interest. By quantifying these energetics, this work enables the intelligent selection among solvents, or mixtures thereof, to tune this environment to have more desirable energetics for surface adsorption or desorption for these species of interest. Recent work by this group has developed a model to estimate the difference in the adsorption energy of an adsorbate in a solvent versus its adsorption energy in the gas phase[42]. The energy in gas phase is much easier to measure and calculate, so knowing how to estimate this difference provides a lot of predictive ability of importance to catalysis research. This model utilizes the adhesion energy of the solvent to the metal surface, E_{adh}, and surface energy of the solvent, $\gamma_{S(liq)}$, to quantify the solvent effects. The surface energy is a tabulated value for common solvents of interest, but currently there is no way to directly measure the adhesion energy of a liquid solvent to a clean metal surface. To this end, this group also recently developed a model that used a standard thermodynamic cycle to derive a relationship between the adhesion energy of a solvent and the experimentally determined differential heat of

adsorption data collected via SCAC[43,44]. This enables us to estimate the adhesion energy for solvents of interest, and in turn quantify their effects on the reaction environment, by studying the adsorption energetics of these solvents using our calorimeters.

Acetonitrile is an important solvent of interest, because of its wide use for a number of applications ranging from batteries to electrocatalysis to biofuels synthesis[45–49]. It has a number of unique, desirable properties including its high dielectric constant, aprotic nature, low viscosity, and high miscibility with other polar solvents, which makes it of particular interest for electrochemical applications and the engineering of optimal mixed solvent environments[50–54]. Additionally, as the simplest example of an organic nitrile, a fundamental understanding of its interactions with Pt(111) is of general interest to surface chemistry and catalysis. The measurement of the adhesion energy of acetonitrile to a Pt-group metal, and the use of that value to estimate the adsorption energetics of catalytic and electrocatalytic reaction intermediates on that and other Pt-group metal surfaces, which generally have similar molecular adsorption and adhesion energies to Pt[27,40,44], will aid in developing a basic understanding of those important reactions, their mechanisms, and their reaction energy diagrams. Platinum is also a common electrode used in electrocatalysis, making this solvent/metal pair even more relevant to these systems. Previous experimental results from TPD and vibrational spectroscopy (RAIRS) studies on Pt(111) have shown that acetonitrile adsorbs and forms multilayers at low temperatures (<150 K), but only forms a single, molecularly adsorbed adlayer from 150 to ~ 200 K[55].

This dissertation reports the enthalpies of adsorption for acetonitrile to clean Pt(111) at 100 K and 180 K, measured in ultrahigh vacuum using SCAC. These adsorption energies are reported as a function of coverage, and from that, the adhesion energy of liquid acetonitrile to Pt(111) is estimated to be E_{adh} = 0.198 J/m^2. The saturation coverage is also shown to be higher

at 100 K than 180 K, which is attributed to the formation of a less stable adsorbate configuration at 100 K. The quantification of the adhesion energy allows for the estimation of this important solvent on the adsorption energies of catalytic reaction intermediates. Additionally, these are the first reported adsorption energy values for any nitrile-containing molecule on any Pt-group metal surface, and as such, they serve as important benchmarks for validating the energy accuracy of computational methods like DFT for nitrile adsorption.

Similarly, the adhesion energy of *n*-decane to Pt(111) is of great interest in catalysis since linear alkanes of that and similar size are commonly used as solvents in catalytic reactions over Pt-group metals. Its adsorption energy onto Pt(111) is also of fundamental interest since hydrocarbon reactions on Pt surfaces are common in petroleum and biomass catalysis. The desorption energy of shorter linear alkanes (C_6 and smaller) on Pt(111) was previously measured using TPD[56], but *n*-octane and *n*-decane dissociate upon desorption, and therefore their desorption energetics could not be measured (using TPD). That previous study elucidated trends amongst these smaller hydrocarbons, namely that the desorption energy increases nearly proportionally to carbon number while the adhesion energy remains nearly constant (holding the surface constant). It has been shown previously that the heat of adsorption of neutral reaction intermediates decreases in a particular solvent by an amount equal to the adhesion energy per unit area, E_{adh}, of that liquid solvent to the surface times the area on the surface occupied by that adsorbed intermediate[42–44,57]. Therefore, quantifying the adhesion energy of *n*-decane on Pt(111) can provide insight into whether these trends in adhesion energy extend to larger hydrocarbon molecules that desorb irreversibly, and consequently enable the estimation of the effects of these larger species more broadly on the adsorption energetics of reaction intermediates. This work reports the enthalpy of adsorption for *n*-decane to clean Pt(111) at 150 K, measured using SCAC.

Again, by using the adsorption energy out to bulk, multilayer coverages, we estimate the adhesion energy of liquid *n*-decane to Pt(111) to be E_{adh} = 0.148 J/m^2. This work shows that the adsorption and adhesion energies of *n*-decane align with those observed via TPD for smaller linear alkanes, and now extends this understanding to systems that desorb irreversibly. In addition, this work provides highly accurate adsorption energy values for *n*-decane, one of the largest commonly studied hydrocarbon molecules in surface science. This provides important fundamental insight into the catalysis of hydrocarbon species on Pt-group metals, which are ubiquitous in a number of industrial catalytic processes. Further, in comparison to other SCAC studies from the Campbell group with unsaturated hydrocarbon adsorbates[34,58–61], this work more generally elucidates the energetics differences of saturated and unsaturated hydrocarbons on Pt-group metals, which is relevant to a wide range of industrial and emergent applications.

Naphthalene and azulene are the simplest examples of multiple-ring aromatic hydrocarbons with structural features common to adsorbed aromatic species on catalyst surfaces during hydrocarbon conversion reactions by late transition metal surfaces. They are also of current interest as model compounds for the local structure at the surface of graphene-based systems, which have promise for wide ranging applications from catalysis to microelectronics, optoelectronics, and quantum technologies. Naphthalene, a pair of C_6 aromatic rings, is a representative molecule for the regular graphene structure. Azulene, the C_5-C_7 isomer of naphthalene, represents the most common defect found in graphene sheets (often called the 5-7 defect). Graphene is well known as one of the most prominent 2-D materials due to the unique and desirable electronic and mechanical properties of its ideal lattice[62]. However, large-scale graphene samples are typically polycrystalline and contain topological defects, of which the 5-7 defect is most common[63–69]. These defects have strong influences on the physical and chemical

properties of the larger graphene sheets, affecting chemical reactivity[70,71], mechanical strength[68,69,72,73], electron transport[64,66], and magnetism[74]. Additionally, the contacts between graphene and metals, formed during the epitaxial growth of graphene sheets on metallic substrates, play an important role in controlling performance-determining parameters in graphene-based electronic devices[75,76]. Given the substantial influence defect sites can have on the overall properties of a graphene sample, it is very likely that they have a large effect on the interactions of this graphene/metal interface. However, these defects are embedded in graphene sheets in low concentrations, making these interactions extremely difficult to study experimentally. By comparing the energetic differences between these two representative molecules we are able to gain insight into how these defect sites interact with the metal surface on which graphene is grown, and how they alter the physical and electronic properties of the graphene sheet.

To date, comparative studies of naphthalene and azulene on Pt(111) have not been reported. Limited studies of each species individually are reported in literature, using low-energy electron diffraction (LEED)[77–80], TPD[78,79], and scanning tunneling microscopy (STM)[81–83]. Further studies of naphthalene on Pt(111) were performed using work function (WF) measurements[80], adsorption calorimetry[60], and DFT calculations[84,85]. This dissertation reports the study of azulene adsorption on Pt(111) at 150 K measured by SCAC, and compares these results to previous SCAC results for naphthalene on Pt(111)[60] and DFT simulations of both systems. We show that azulene binds much more strongly to the surface (by ~100 kJ/mol) than naphthalene, which confirms the extremely strong interactions of these defect sites with the underlying metal surface. This is also an important fundamental insight for the energetics of hydrocarbon species on Pt-group surfaces, as it constitutes the first experimental measurement of any non-alternant

aromatic molecule on any metal surface and compares it to its alternant isomer. (Non-alternant refers to molecules where the carbon atoms cannot be labeled in alternating fashion, which is the case for azulene, versus molecules where the carbon atoms can be, which is the case for naphthalene. See *Figure 5-1b,c* for a visual representation of this.)

When comparing to DFT models of both systems[61,86,87], we show that DFT overestimates the binding energy of naphthalene, but quite accurately calculates the binding energy of azulene to the Pt(111) surface. This quantifies the energy accuracy of both systems and provides benchmarks for computational models of graphene-based systems more broadly. This works also identifies that DFT is not accurately capturing the difference in energetics between these two adsorbates, and thus the difference in energetics between defect sites and graphene sheets more generally. It should be noted that I was not a primary author on the paper summarizing the research of Chapter 4, and the published paper has been shortened to have a focus on the calorimetry research that I collected, as opposed to the DFT results that were conducted by Klein and Ruppenthal[61].

The work presented in this dissertation also continues the previous efforts of the Campbell group to measure the adsorption energetics of select molecular fragments on late-on transition metal catalysts. For the first time, these studies are extended in this dissertation to now include adsorption on Cu, by studying formate's adsorption energy on Cu(111), produced by the dissociative adsorption of formic acid gas to an oxygen-predosed Cu(111) surface. Formic acid and formate are common and important intermediates in a variety of reactions on late transition metal catalysts. In addition to more well-established industrial reactions such as methanol synthesis, water-gas shift, and steam reforming of methane[88–91], this includes reaction chemistries of interest to emergent clean energy applications such as biomass reforming, fuel cell

feeds, and a potential hydrogen carrier[92–96]. The relevance of formate to CO_2 hydrogenation catalytic processes, particularly in electrocatalysis, is currently the subject of intense study, particularly via computational models[92,93,95–102]. Notably, Cu is the most promising monometallic catalyst for CO_2 reduction chemistries[98,103–105], making this surface/adsorbate pair extremely relevant to efforts to elucidate the mechanisms and reaction pathways within this extremely complex reaction network. Thus, this work is crucial to both better understanding historically observed catalytic trends in well-established industrial processes, as well as the development of new catalytic processes to combat climate change.

To date, the heat of formation of adsorbed formate has only been measured for two surfaces, Pt(111)[30] and Ni(111)[35], both previously reported by this group. In this work, we report the SCAC study of the heat of molecular adsorption of formic acid onto clean Cu(111) at 120 K, and the heat of dissociative adsorption of formic acid onto oxygen-precovered Cu(111) at 240 K. For the case of adsorption on oxygen-precovered Cu, formic acid dissociatively adsorbs to form bidentate formate and desorbed gaseous water. From these experimental values, we extract a bond energy of bidentate formate to the Cu(111) surface of 335 kJ/mol, and an enthalpy of formation of bidentate formate on Cu(111) of -465 kJ/mol. We show that these enthalpies are slightly greater than those on Ni(111) (by ~15 kJ/mol) and significantly greater than those on Pt(111) (by ~85 kJ/mol). This is similar to the predicted order of bond strength from DFT, where Ni and Cu are predicted to bind formate with similar strengths[35,102], while Pt is predicted to bind formate ~60 kJ/mol more weakly[106]. These DFT bond energies are uniformly ~54 kJ/mol too weak compared to SCAC results on these three surfaces.

This study constitutes the first experimental measurement of the adsorption energy of *any* molecular fragment on *any* Cu surface, and for the first time completes the study of one of the

selected adsorbate fragments on Pt(111)[30], Ni(111)[35], and Cu(111) surfaces. This allows for the direct comparison of a single adsorbate fragment on all three metals for the first time. This constitutes a key suite of experimental benchmarks for computational models of catalysis on late-transition metals, and also expands the systematic understanding of fundamental adsorption energetics that elucidate observed differences and trends in catalytic activity. These insights are crucial to the intelligent, rapid development of new catalysts and catalytic processes that can enable the transition of human society off of fossil fuels.

This dissertation presents a suite of experimental systems that contribute to a broader understanding of the energetics of heterogeneous catalysis on late transition metals. **Chapter 2** discusses the single crystal adsorption calorimetry apparatus and experimental procedures. **Chapter 3** presents the study of the energetics of acetonitrile adsorption on Pt(111), and its resulting insights into the solvent effects of this system. **Chapter 4** reports the study of *n*-decane adsorption on Pt(111) and the analysis of adsorption and adhesion energy trends amongst linear alkanes on catalytically relevant surfaces. **Chapter 5** presents the study of azulene adsorption on Pt(111), its comparison to naphthalene and DFT, and the resulting insights into graphene-based systems. **Chapter 6** presents the study of the energetics of molecular and dissociative adsorption of formic acid on clean and oxygen-precovered Cu(111), the resulting extracted values for the energetics of the formate fragment on the surface, and its comparison to Pt(111), Ni(111), and DFT calculations on all three systems.

In addition, **Chapter 7** presents a kinetic and surface-spectroscopic study of aqueous thermal and electrocatalytic hydrogenation of phenol and benzaldehyde on late transition metal catalysts, namely Pt, Pd, and Rh, supported as nanoparticles on powdered carbon. These molecules represent common intermediates in the process of breaking down biomass and

converting its constituents into biofuels or other biomass-derived chemicals. This work preceded my decision to focus my research on single crystal adsorption calorimetry, and was part of a prior project in collaboration with the Chemical Transformations Initiative at Pacific Northwest National Laboratory. Consequently, this work does not utilize SCAC, but instead uses small-scale, liquid-phase thermal and electrocatalytic reactors to elucidate observed differences in catalytic activity for these metals and small, aromatic molecules. It should be noted that I was not the primary author of the paper summarized in Chapter 7 (that was a postdoc, Dr. Nirala Singh) nor did I contribute to the collection and analysis of the X-ray scattering studies in that chapter. However, those portions have been included for completeness of narrative and the full context of the conclusions of that research. Fundamentally, however, Chapter 7 also seeks to further the broad experimental goals discussed above, namely developing a systematic understanding of the catalysis of these representative molecules by correlating molecular structure, particularly functional groups bound to aromatic rings, with reactivity and selectivity on transition metal catalysts.

The complexity of products that results from the breakdown of biomass and particularly lignin, the most energy dense constituent, inhibits the development of new catalytic reactions to enable the replacement of fossil fuel feedstocks with biomass derived alternatives[107–109]. Lignin is composed of a heterogeneous network of aromatic rings, which break apart into a complex suite of small, functionalized, aromatic molecules[110,111]. Simple changes in the adsorbate's structure can drastically alter the observed reactivity on a particular catalyst of interest. For example, benzaldehyde undergoing electrocatalytic hydrogenation on Pd exhibits a turnover frequency that is several orders of magnitude higher than that for phenol in equivalent conditions[112]. The work presented in Chapter 7 studies the kinetics of the hydrogenation reaction

of these representative molecules, through both thermal and electrocatalytic pathways, in order to develop rate laws and fundamental mechanistic insights that explain the observed trends in reactivity. We show that the observed catalytic behavior is well fit by a Langmuir-Hinshelwood mechanism with competitive adsorption (organic versus hydrogen adsorption) on terrace, or (111)-like, sites. Additionally, X-ray scattering studies and cyclic voltammetry are conducted to elucidate these competitive interactions of surface adsorbates, as well as their interactions with both the surface and bulk phase of the metal catalysts. A portion of these results show that adsorbed benzaldehyde inhibits the migration of H adatoms into the bulk Pd metal, whereas phenol does not. This greatly increases the surface coverage of H adatoms that are able to react for benzaldehyde hydrogenation, and explains the extreme difference in observed reaction rates. This study, along with a suite of similar studies from the CTI at PNNL[112–120], provides systematic insights into the fundamental energetics of biomass intermediates on transition metal catalyst surfaces that can explain observed differences in catalytic activity. This in turn informs efforts towards the strategic development of new catalytic pathways for the conversion of biomass into fuels and other value-added chemicals.

Table 1-1 lists the publications reprinted or in preparation in this dissertation and their corresponding chapters. To summarize, this work provides a suite of experimental studies that contribute to a deeper fundamental understanding of trends in reactivity and selectivity in late transition metal catalysis. Importantly, these results also provide key experimental benchmarks to improve the energy accuracy of computational chemistry models such as DFT.

Table 1-1. Publications reprinted or in preparation in this dissertation and their corresponding chapters.

Chapter	**Publication**
Chapter 3	**Ruehl, G.** and Harman, S. E., Arnadottir, L., & Campbell, C. T. Acetonitrile Adsorption and Adhesion Energies onto the Pt (111) Surface by Calorimetry. *ACS Catalysis* **12**, 156–163 (2022).
Chapter 4	Harman, S. E. and **Ruehl, G.**, & Campbell, C. T. Adsorption and Adhesion Energies of n-Decane on the Pt(111) Surface by Calorimetry. *In preparation.*
Chapter 5	Klein, B. P., Harman, S. E., Ruppenthal, L., **Ruehl, G.**, Hall, S. J., Carey, S. J., Herritsch, J., Schmid, M., Maurer, R. J., Tonner, R., Campbell, C. T., & Gottfried, J. M. Enhanced Bonding of Pentagon − Heptagon Defects in Graphene to Metal Surfaces: Insights from the Adsorption of Azulene and Naphthalene to Pt(111). *Chemistry of Materials* **32**, 1041–1053 (2020).
Chapter 6	**Ruehl, G.** and S. E. Harman, Gluth, O., LaVoy, D., & Campbell, C. T. Energetics of Adsorbed Formate and Formic Acid on Cu(111) by Calorimetry. *Submitted.*
Chapter 7	Singh, N., Sanyal, U., **Ruehl, G.**, Stoerzinger, K. A., Gutiérrez, O. Y., Camaioni, D. M., Fulton, J. L., Lercher, J. A., & Campbell, C. T. Aqueous phase catalytic and electrocatalytic hydrogenation of phenol and benzaldehyde over platinum group metals. *Journal of Catalysis* **382**, 372–384 (2020).

Chapter 2 Instrumentation

The single-crystal adsorption calorimetry (SCAC) experiments are performed in a custom ultrahigh vacuum chamber with a typical base pressure < 2 x 10^{-10} Torr. The chamber is subdivided into three separate sections, the analysis chamber, the experimental chamber, and the molecular beam, with the molecular beam being separated by a gate valve. Figure 2-1 presents an overview of the exterior of the calorimeter. The experimental chamber is where absorption experiments are carried out and contains the necessary components for those runs, the analysis chamber contains multiple *in situ* analytical instruments used for surface characterization and assessment, and the molecular beam houses the adsorbate molecule of interest and creates the directed beam of molecular flux necessary for experiments. The apparatus and its procedures have been described in detail previously in two *Review of Scientific Instruments* publications[25,26], but this chapter will briefly discuss the sample preparations, instrumentation, and methods. The SCAC apparatus is unique in its ability to measure the heat released during irreversible adsorption processes (dissociation, degradation upon desorption, etc.), which sets it apart from traditional techniques such as temperature programmed desorption (TPD).

The analytical chamber is equipped with *in situ* X-ray photoelectron spectroscopy (XPS), low-energy electron diffraction (LEED), Auger electron spectroscopy (AES), low-energy ion-scattering spectroscopy (LEIS), and an ion gun used for Ar^+ sputtering procedures. These are used to clean and characterize the surface and crystal structure, in order to ensure proper conditions for experiments and validate cleaning procedures for sample cleanliness. The experimental chamber is equipped with the heat detector, the sample holder, a quadrupole mass spectrometer (QMS), a quartz-crystal microbalance (QCM), and a resistive heater. The molecular beam houses a glass bulb with the adsorbate of interest, a gas manifold to control gas flux, a

glass-capillary array that is heated to prevent dimerization of the adsorbate molecules, a series of liquid nitrogen cooled orifices to collimate the beam of flux, and a chopper to pulse the beam into 102 ms pulses every 3 seconds. The vacuum of the chamber is maintained through the use of 3 rough pumps, 3 turbo pumps, and a titanium sublimation pump.

2.1 Sample Preparation

The crystals used were supplied by Jaques Chevallier and Bine Hansen at Aarhus University in Denmark. For experiments on Pt(111) a 1 μm crystal foil was used, while experiments on Cu(111) used a 2 μm crystal foil in order to improve rigidity of the sample and consequent contact quality with the heat detector, as Cu has a significantly higher ductility than previous samples of Pt and Ni. The samples are atomically deposited and supplied on a salt block, which is first carefully washed off of the sample. Then the foil is spot welded between tantalum rings and mounted on a copper sample holder that interfaces with the sample mount in the chamber. The samples are cleaned in vacuum by repeated cycles of 1.25 kV Ar^+ ion sputtering to remove any contaminants. Pt samples were then annealed in 1 x 10^{-7} O_2 at 600 K to remove carbon contaminants, followed by annealing in the absence of O_2 at 1050 K to remove any oxygen. An exact annealing temperature could not be determined for the Cu samples due the high optical reflectivity of Cu inhibiting the use of an optical pyrometer, so the sample was annealed at a repeated temperature (based on power supplied to the heater) that was high enough to establish a well ordered (111) LEED pattern. These treatments were repeated as necessary until impurities were below the detection limit of XPS and the surface gave a sharp (111) LEED pattern. In order to prepare oxygen-precovered Cu(111) for the formic acid experiments, the clean Cu(111) surface was exposed at 240 K to 30 Langmuir of O_2 gas.

2.2 Heat Measurements

Calorimetry experiments were performed by exposing the metal crystal surface to a pulsed molecular beam of the adsorbate of interest (azulene, decane, acetonitrile, and formic acid). Each pulse was 102 ms in length and repeated every 3 s. In the case of adsorbate molecules that are liquid at room temperature (decane, acetonitrile, and formic acid) the liquid reservoir of the molecule was outgassed with repeated cycles of freeze-pump-thaw, until gaseous impurities were no longer evolved out of the liquid solution upon melting. In the case of azulene, which remains solid until 99 °C, the glass reservoir was replaced by a metal reservoir that was heated, along with the gas manifold, with heat tapes to evaporate sufficient flux for experiments. The purity of each molecular beam was verified by mass spectrometry. The beam was created expanding ~1-4 mbar (depending on the molecule) of the molecule of interest through a glass microchannel array at a sufficiently high temperature to prevent dimerization of the gas molecules (see individual chapters for details specific to each molecule). After leaving the array, the beam is collimated through a series of five liquid-nitrogen-cooled orifices with progressively smaller diameters, as described in-depth previously[26]. A chopper is then used to pulse the beam into the 102 ms pulses, which and are directed at the surface of the sample with a final circular beam diameter of 4.36 mm. The flux of the beam is quantified using a liquid-nitrogen-cooled quartz crystal microbalance (QCM), where the beam is impinged onto the QCM surface and a rate of adsorption can be quantified (the calibration of the QCM has been described in detail previously[26]). Coverages are reported in monolayers (ML) and are defined as the number of molecules that adsorb to the surface, normalized by the number of surface atoms (1.50×10^{19} atoms/m^2 for Pt(111) and 1.77×10^{19} atoms/m^2 for Cu(111)).

The sample is held on a fixed thermal reservoir by grooves in the sample holder that interface with the reservoir. The hollow reservoir is cooled by flowing liquid-nitrogen-cooled N_2 gas through it, which transfers heat to the sample via thermal contact. The flow rate of the N_2 gas is moderated to achieve the desired sample temperature. As the foil is too thin to directly mount a thermocouple to, a sample temperature is determined to be the average of two thermocouples spot-welded to the two closest locations: one is spot-welded to the fixed reservoir and the other to heat detector housing. For all of the experimental systems in this work the readings of these two thermocouples differed by ~ 10 K on average.

The heat detector is a pyroelectric polyvinylidene fluoride (PVDF) ribbon that is translated into contact and gently pressed against the back of the sample. The ribbon is painted on opposite sides with two metal leads which, when connected to the circuit discussed below, translate input heat into a dielectric response that is measured and recorded. The heat detector response is calibrated in each run by pulses from a HeNe laser (632.8 nm) with known power. Before each calorimetry run, the heat detector is rolled out of contact, the sample is flash heated (<2 s) to either 1050 K (Pt) or the established power that gives a sharp LEED pattern (Cu), and the heat detector is rolled back into contact and allowed to reestablish thermal equilibrium (< 5 mins). An internal view of these components in the experimental chamber is shown in Figure 2-2. The absolute accuracy of the calorimetric heats is estimated to be better than 4%, based on comparison of the experimentally measured heats for the formation of multilayers to literature values for standard enthalpies of sublimation of the bulk solids.

For the formic acid on Cu(111) experiments, the heat detector was rebuilt to more gently press against the back of the sample. This was done in order to improve contact without causing permanent deformation of the sample as a result of copper's high ductility. To do so, the detector

housing was disassembled and rebuilt. Figure 2-3 shows a close up look at the detector housing (the "cal head") with the ribbon seen arcing in front of the housing itself. Inside of the housing, the ribbon is held in place by a stack of sapphire and copper blocks that constitute a circuit for the dielectric response to be measured and recorded. Figure 2-4 shows a schematic of this stack. By changing the thickness of the center copper block (labeled t in Figure 2-4), the diameter of the ribbon arc can be adjusted. By changing the diameter of that arc from 3 mm to 6 mm, the signal was increased by ~4-fold.

Sticking probabilities were measured simultaneously with calorimetric measurements via the King and Wells method[121]. A mass spectrometer without line of sight to the sample measured the background pressure increase of the molecule of interest in the chamber (for example: formic acid, HCOOH, m/z = 46). In order to calibrate this signal, a room temperature gold flag was rolled in front of the sample surface and molecules were dosed in an identical manner as during experiments. All incoming molecules reflected off of the gold flag, and a "zero-sticking" signal was collected on the mass spectrometer which corresponds to full reflection of the molecules. The sticking probability is then calculated as the ratio of the integrated mass spectrometer signal for an individual pulse, over the integrated mass spectrometer signal for the average of 30 zero-sticking pulses. We report two types of sticking probabilities in our work, the long-term (S_∞) and short-term (S_{102ms}) sticking[58]. The long-term sticking is defined as the probability that a gas molecule strikes the sample surface, sticks, and remains until the start of the next gas pulse 3 s later. This is used to calculate the adsorbate coverage remaining at the start of the next gas pulse. The short-term sticking probability is defined as the probability that a gas molecule strikes the sample surface, sticks, and remains at least throughout the time window of the heat measurement (i.e., the first 102 ms). This is used to calculate the number of moles of gas-phase reactants that

contribute to the measured heat of adsorption. When there is no desorption between pulses, the two sticking probabilities are the same.

2.3 Figures

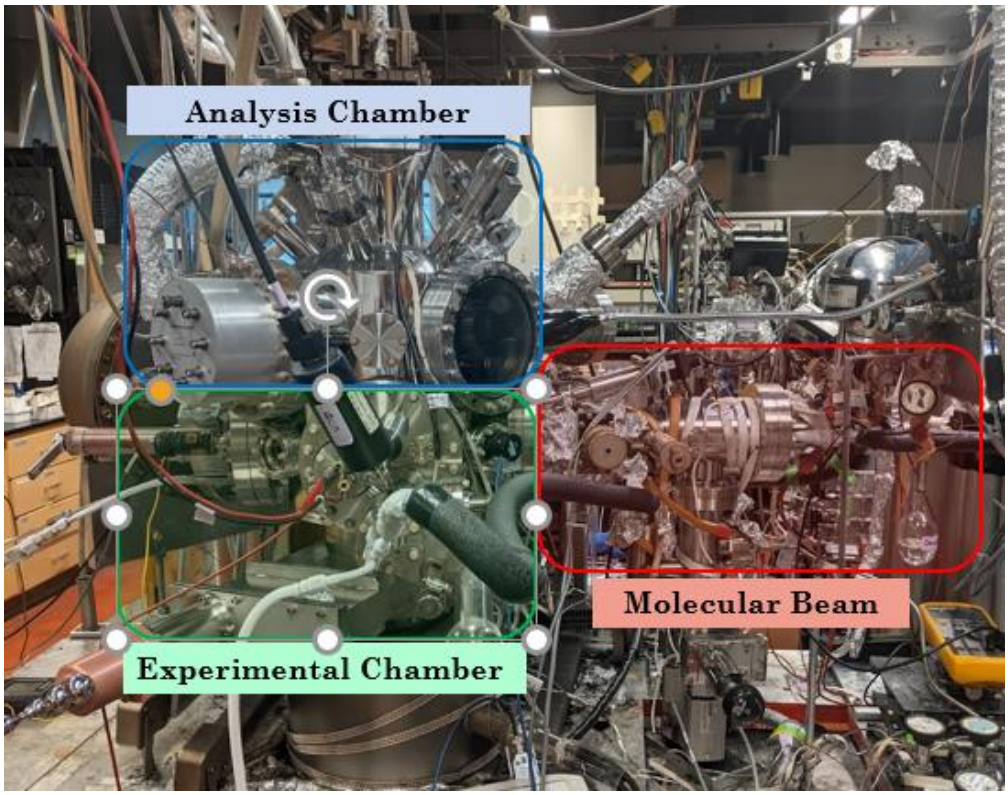

Figure 2-1. An external view of the calorimeter with the three subsections of the instrument highlighted: the analysis chamber, the experimental chamber, and the molecular beam.

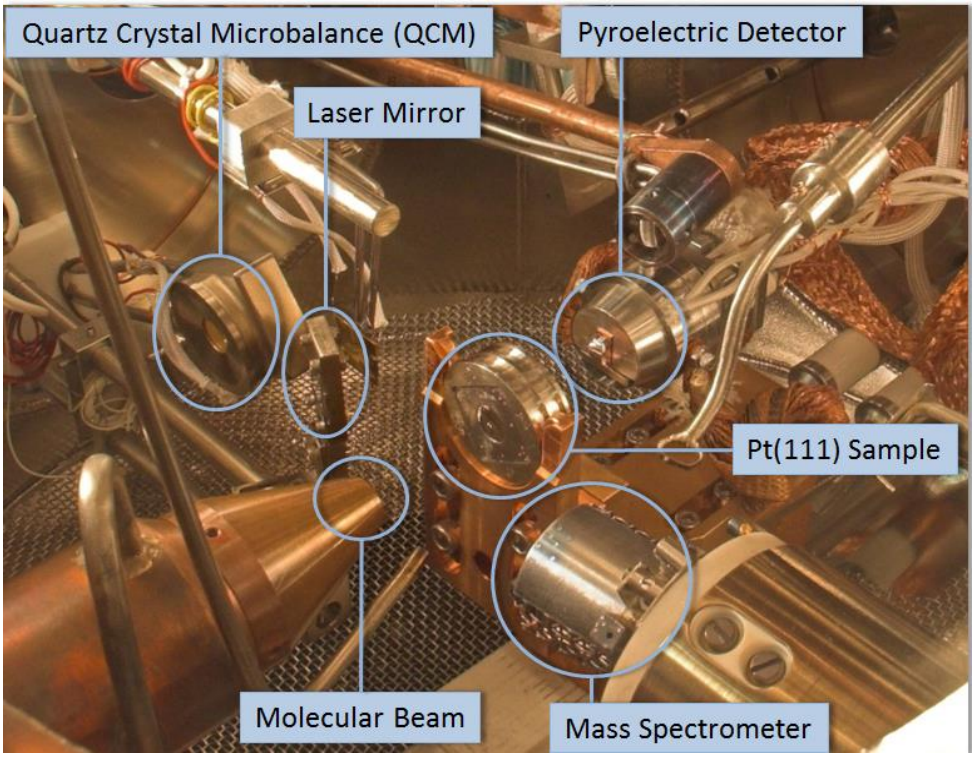

Figure 2-2. An internal view of the experimental chamber of the calorimeter, with the outlet of the molecular beam, mass spectrometer, sample and sample holder, heat detector, quartz crystal microbalance labeled.

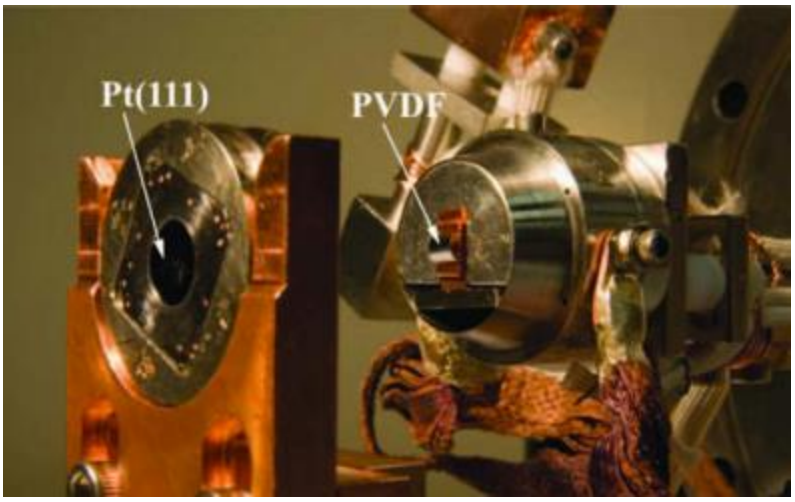

Figure 2-3. A close-up view of the heat detector, rolled out of contact with a Pt(111) sample. The PDVF ribbon is highlighted, and the copper components it is connected to constitute the stack of copper and sapphire blocks that form the circuit it is housed in. Taken from ref.[25].

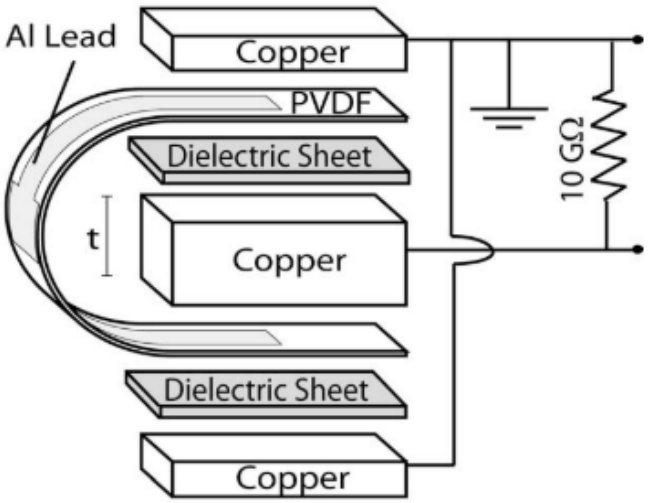

Figure 2-4. A schematic of the stack of copper and dielectric (sapphire) sheets used to form the circuit for the heat detector. The thickness, t, of the central copper block can be changed in order to alter the diameter of the ribbon's arc. Taken from ref.[25].

Chapter 3 Acetonitrile Adsorption and Adhesion Energies onto the Pt(111) Surface by Calorimetry

This chapter has reprinted with permission from reference[122]:

Ruehl, G., Harman, S. E., Arnadottir, L., & Campbell, C. T. Acetonitrile Adsorption and Adhesion Energies onto the Pt (111) Surface by Calorimetry. *ACS Catalysis* **12**, 156–163 (2022).

Chapter Abstract

Acetonitrile is a common solvent for heterogeneous catalysis and electrochemical applications, as well as the simplest example of an organic nitrile. Understanding the energetics and nature of its interactions with Pt(111) is of interest for a wide array of applications, especially for estimating the effect of acetonitrile as a solvent on the adsorption energies of catalytic and electrocatalytic reaction intermediates on Pt-group metals. Here, the heat of adsorption of molecular acetonitrile on clean Pt(111) was measured by single crystal adsorption calorimetry (SCAC) as a function of coverage, and from that, the adhesion energy of liquid acetonitrile to Pt(111) was estimated. At 180 K, the differential heat of adsorption is initially 82.9 kJ/mol, decreasing to 63.2 kJ/mol by a saturation coverage of 0.25 ML. The integral (average) heat of adsorption at 180 K is 74.3 kJ/mol at a saturation coverage of 0.25 ML. At 100 K, the heat of adsorption is 84.5 kJ/mol initially, decreases to ~45 kJ/mol after the completion of the first layer (0.35 ML), and finally reaches a constant multilayer heat of 43.4 kJ/mol at

coverages higher than 0.7 ML. (Errors bars on all heats are ±4%.) The saturation coverage is higher at 100 K than 180 K, attributed to the formation of a less stable adsorbate configuration at 100 K due to lower surface mobility. Using the heats of adsorption at 100 K up to bulklike multilayer coverages, we estimate the adhesion energy for liquid acetonitrile to Pt(111) to be 0.198 J/m^2, which can be used to estimate the effect of acetonitrile as a solvent on the adsorption energies of catalytic reactants relative to the gas phase. This adhesion energy is considerably lower than those for water, benzene, and phenol on Pt(111) but slightly greater than those for methanol and formic acid.

3.1 Introduction

Due to its wide use as a solvent, the interactions of acetonitrile with Pt surfaces are important in electrochemistry and electrocatalysis. As the simplest example of an organic nitrile, a fundamental understanding of its interactions with Pt(111) is also of general interest to surface chemistry and catalysis. Here, we report calorimetric measurements of adsorption energies versus coverage of molecularly adsorbed acetonitrile on clean Pt(111) at 100 and 180 K and estimate from these the adhesion energy of liquid acetonitrile to Pt(111) at room temperature. Most importantly, this adhesion energy can be used to estimate the adsorption energies of catalytic reaction intermediates on Pt(111) in an acetonitrile solvent based on energies measured (or calculated) in the gas phase. This is done using an equation we recently developed that shows that the difference in adsorption energy in a liquid solvent relative to the gas phase is dominated by the product of this solvent adhesion energy times the footprint area of the adsorbed intermediate on the surface[42,123]. Since there is vast knowledge already of adsorption energies on Pt-group metals in the gas phase, but very few such energies are known in liquid solvents, this opens up important new opportunities to gain fundamental insights into catalysis in liquid solvents and electrocatalysis.

Acetonitrile is a polar, organic solvent commonly used in a number of chemical reactions and synthesis processes. Its high dielectric constant and aprotic nature make it an attractive electrolyte solvent in electrochemical reactions and electrocatalysis[124–129], as well as in batteries and capacitors[45–49]. Its low viscosity and high miscibility with a wide variety of polar solvents and solutes makes it promising for applications in many other areas of heterogeneous catalysis including biofuels synthesis and biomass-based chemical upgrading, as well as the engineering of optimal mixed solvent environments[50–54]. The measurement here of its adhesion energy to a

Pt-group metal, and the use of that value to estimate the adsorption energies of catalytic and electrocatalytic reaction intermediates on that and other Pt-group metal surfaces, which generally have similar molecular adsorption and adhesion energies to Pt[27,40,44], will aid in developing a basic understanding of those important reactions, their mechanisms, and their reaction energy diagrams.

Platinum, in addition to its widespread use as a heterogeneous catalyst in numerous industrial processes, is a common electrode material for electrochemical applications. Therefore, elucidating the energetics and nature of the interaction between acetonitrile and the Pt surface is of great interest. Pt(111) is the most thermodynamically stable face of platinum and is consequently commonly used as a model catalyst. Previously, experimental results from temperature- programmed desorption (TPD) and vibrational spectroscopy (RAIRS) studies have shown that acetonitrile will form multilayers at low temperatures (<150 K) but only forms a single, molecularly adsorbed adlayer from 150 to ~200 K[55]. The adsorption of acetonitrile on Pt(111) has also been studied by density functional theory (DFT)[130–132]. Here, we report the enthalpies of adsorption for acetonitrile to clean Pt(111) at 100 and 180 K, determined in ultrahigh vacuum conditions using single-crystal adsorption calorimetry (SCAC). These results, when combined with those recent RAIRS, TPD, and DFT studies, provide detailed insight into the nature and energy of surface adsorption and interaction of acetonitrile with Pt(111). Enthalpies of adsorption for acetonitrile to clean Pt(111) have also been studied by SCAC previously, but only at 298 K[131], where later TPD studies show that the first layer is already desorbed almost completely[55]. The highly accurate adsorption energy and estimated adhesion energy of acetonitrile on Pt(111) reported here are the first such values reported for any nitrile-containing molecule on any Pt-group metal surface, and as such, they serve as important

benchmarks for validating the energy accuracy of computational methods (like density functional theory) used to estimate these energies when nitrile groups are involved. In addition, a recently developed method by this group has enabled the extraction of solvent adhesion energies from SCAC measurements of adsorption energies in ultrahigh vacuum (UHV)[44]. Below, we use this method to extract and report the adhesion energy of liquid acetonitrile to the Pt(111) surface. This adhesion energy can in turn be used to quantitatively estimate the effect of this important solvent on the adsorption energies of catalytic reaction intermediates, as described previously[42,123]. This knowledge is of interest for efforts to utilize solvent properties to tune intermediate energetics and interactions with the catalyst surface and consequently affect reaction rates and selectivities in liquid solvents.

3.2 Experimental Methodology

The experiments were performed in an ultrahigh vacuum (UHV) chamber (base pressure $<2 \times 10^{-10}$ mbar) designed for single-crystal adsorption calorimetry (SCAC). The chamber is also equipped with X-ray photoelectron spectroscopy (XPS), low-energy electron diffraction (LEED), Auger electron spectroscopy (AES), low-energy ion-scattering spectroscopy (LEIS), a quadrupole mass spectrometer (QMS), and a liquid-nitrogen-cooled quartz crystal microbalance (QCM). The SCAC apparatus and experimental procedures for the molecular beam flux, sticking probability, and heat measurements have been described in depth previously[25,26,58].

To briefly summarize, the Pt(111) sample used was a 1 μm thick single-crystal foil provided by Bine Hansen at Aarhus University. The surface was cleaned by repeated cycles of Ar^+ ion sputtering and annealing to 1120 K. The Pt(111) surface was exposed to a pulsed, collimated molecular beam of acetonitrile, and the heat of adsorption and sticking probability

were recorded simultaneously. The sticking probability was measured with a QMS using the King and Wells method[121], and the heat of adsorption was measured by a pyroelectric ribbon pressed against the back of the Pt(111) crystal. The molecular beam was created by expanding approximately 1.5 mbar of acetonitrile through a glass capillary array and collimated through a series of orifices that are cooled with liquid nitrogen. The resulting molecular beam is then chopped into 102 ms pulses every 3 s.

Here, one monolayer of coverage is defined as the number of molecules of acetonitrile adsorbed to the surface per unit area, normalized to the density of Pt atoms on the (111) surface (1.50×10^{19} atoms/m^2). A typical dose is 0.005 ML ($\sim 1.0 \times 10^{12}$ molecules within the beam diameter of ~4 mm) per acetonitrile gas pulse.

3.3 Results

3.3.1 Sticking Probabilities

Figure 3-1 shows the average long-term (S_∞) and short-term (S_{102ms}) sticking probabilities versus coverage for acetonitrile adsorption on clean Pt(111) at 180 K. The long-term sticking probability is the probability that a gas molecule strikes the sample surface, sticks, and remains until the next gas pulse starts 3 s later. This is used to calculate the adsorbate coverage remaining at the start of the next gas pulse. The short-term sticking probability is the probability that a gas molecule strikes the sample surface, sticks, and remains at least throughout the time window of the heat measurement (i.e., the first 102 ms). This is used to calculate the number of moles of gas-phase reactants that contribute to the measured heat of adsorption.

At 180 K, the long-term and short-term sticking probabilities were indistinguishable below 0.23 ML. They both start at a probability of ~0.98 and decrease with coverage to ~0.88

by 0.23 ML. Past this coverage, the long-term sticking probability drops off rapidly, reaching zero by 0.25 ML, while the short-term sticking probability remains high (>0.80). This indicates that the adsorption of acetonitrile on Pt(111) saturates by a coverage of 0.25 ML at 180 K; however, acetonitrile continues to transiently adsorb on that adlayer with a high probability but desorbs again completely (but slowly) before the next pulse starts 3 s later.

Accurate determination of the long-term sticking probabilities at 180 K and high coverage was complicated by adsorption and desorption of acetonitrile on the walls of the vacuum chamber. Molecules that did not adsorb left the Pt surface and adsorbed transiently on the chamber walls, with a residence time on the same scale of the 3 s pulse period. This resulted in a mass spectrometer signal that was a combination of the "real" signal coming from molecules directly leaving the Pt surface and the "background" signal of molecules desorbing from the chamber walls. Accurately distinguishing between these two signals was impossible without using a simple assumption based on previous TPD measurements. Those TPD results showed that more than a single layer will not build up at 180 K[55], and therefore the long-term sticking probability must drop to zero upon saturation of the first layer at 180 K. We used this to more accurately estimate the background signal of the mass spectrometer, chosen such that the long-term sticking probability decreases to zero after saturation at 180 K. As seen in Figure 3-1, this steep drop occurs at a coverage of ~0.25 ML. This measured long-term sticking probability was then applied to the heat measurements to calculate accurate coverages.

At 100 K, the short-term sticking probability starts at 0.98 and increases to unity within <1% by 0.15 ML. The long-term sticking probability is the same as the short-term sticking probability within error bars (~1%) at all coverages. As this temperature is cold enough to form

multilayers of acetonitrile on the Pt(111) surface, the sticking probabilities remain at unity through the formation of at least five multilayers.

3.3.2 Heats of Adsorption

In this paper, the term "heat of adsorption" is defined as the negative of the standard molar enthalpy change for the adsorption reaction, with the gas and the sample surface being at the same temperature. As explained in detail previously, this requires a small enthalpy correction on the measured heat since the gas molecule's enthalpy at this temperature is slightly different than a Boltzmann distribution at the sample temperature due to the actual experimental molecular beam conditions[133]. The differential heat of adsorption is the heat released per mole when a small increment of adsorbate is added to the surface at nearly fixed coverage, as occurs in one of our molecular beam pulses during SCAC. The integral heat of adsorption is the integral of the differential heat versus coverage from zero up to the coverage of interest, divided by that coverage, and is thus the average heat for that coverage range. Figure 3-2 shows the differential heat of adsorption for acetonitrile on Pt(111) at 180 K (red) and 100 K (blue) (after this small correction to the raw heats) as a function of total acetonitrile coverage, along with the integral heat of adsorption at 180 K (black). These are the averages of eight and six runs at 100 and 180 K, respectively.

Previous results from literature show that acetonitrile molecularly adsorbs on Pt(111) below ~250 K, and multilayers will adsorb to the surface below 150 K[55]. Thus, calorimetric measurements here correspond to molecular adsorption on Pt(111), with multilayers of acetonitrile forming during the 100 K experiments but not at 180 K. The initial heat of adsorption at 100 K is 84.5 kJ/mol, which decreases until reaching ~45 kJ/mol by ~0.35 ML. The heat then remains constant through ~0.7 ML, before dropping slightly to a final multilayer

heat of 43.4 ± 1.7 kJ/mol. (This is the run-to- run average and standard deviation of the multilayer heats of the eight runs.) Each run's multilayer heat is the pulse-to-pulse average heat for coverages above 0.8 ML. This average multilayer heat is close to the heat of sublimation of bulk acetonitrile of 46.8 kJ/mol at 100 K, estimated from literature values for the enthalpies of phase transitions[134,135] along with heat capacities of solid, liquid, and gaseous acetonitrile[136], as a heat of sublimation at 100 K was not available in literature. Given the error bars in this estimate, the measured heat is probably within the combined error bars. This multilayer heat is also within the error bars of the value from the activation energy of desorption of 44 ± 3 kJ/mol calculated from TPD (discussed further below)[55]. The agreement with these values provides some estimation of the absolute accuracy of the results in Figure 3-2. This is consistent with our previous estimate of the accuracy of the absolute calibration of this calorimeter's heat measurement of 3%[40].

The heat of adsorption at 180 K is initially 82.9 kJ/mol, decreasing to 63.2 kJ/mol by a coverage of ~0.25 ML. After this point, the long-term sticking probability has dropped to zero, indicating that the monolayer of adsorbed acetonitrile has become saturated. Any additional molecules that impinge on the surface adsorb transiently (as indicated by the high short-term sticking probability) but fully desorb before the start of the next pulse 3 s later. The integral heat of adsorption at 180 K is shown in black versus coverage, as fit by (82.9−34.4θ) kJ/ mol, where θ is coverage in ML, with a heat of 74.3 kJ/mol at saturation (0.25 ML).

We estimate the saturation coverage of the adsorbate layer at 180 K to be 0.25 ML. (The midpoint of the steep drop off in the long-term sticking probability in Figure 3-1 occurs at 0.248 ML.) This is in excellent agreement with the coverage of one-fourth that corresponds to an ideal (2 × 2) overlayer with one acetonitrile molecule for every four Pt surface atoms. This is

supported by a previous study that used low-energy electron diffraction (LEED) and found the presence of a (2 × 2) overlayer for acetonitrile adsorbed on Pt(111) up through the coverages of 0.19 ML, though this pattern was replaced by the absence of long-range order by the next coverage studied of 0.36 ML and the experimental temperature was not reported[137]. Additionally, the Somorjai group found the acetonitrile saturation coverage on Ni(111) at 190 K to also be a (2 × 2) overlayer using LEED[138]. As seen in Figure 3-2, the first layer seems to complete at 100 K at a higher coverage, or ~0.35 ML.

Although the initial heat of adsorption is slightly higher at 100 K than at 180 K (84.5 vs 82.9 kJ/mol), the difference is within the error bars associated with absolute heat calibration (<±4%), and thus, the heat capacity is too small to measure accurately.

3.4 Discussion

3.4.1 Comparison to Temperature-Programmed Desorption

Figure 3-3 compares the activation energy for desorption (E_{des}) of acetonitrile from Pt(111) versus acetonitrile coverage as determined from the heats measured here at 180 K from Figure 3-2 (black dots, corrected as needed by subtracting *1/2RT* [23]) to that from the TPD study of Tylinski et al.[55]. (The temperature *T* we used for this *1/2RT* correction was 220 K, the midpoint of the monolayer TPD peak.) The smooth curve was determined by Tylinski et al. from the inversion of their TPD spectra for acetonitrile desorption from Pt(111) at different coverages, assuming the Polanyi−Wigner rate equation with a prefactor of $\nu = 10^{16}$ s^{-1} (which they assumed to be the same as that obtained from the Arrhenius fit of their multilayer desorption rates in TPD).

The bottom x-axis coverage (per Pt surface atom) here is defined relative to the surface density of Pt atoms on the (111) surface (1.50×10^{19} atoms/m^2), as in Figures 3-1 and 3-2. The top x-axis coverage ($ML_{Tylinski}$) was defined by Tylinski et al. such that 1.0 $ML_{Tylinski}$ is the highest coverage of acetonitrile before the multilayer peak first appears in the TPD spectra after dosing at 20 K. (One can see this was their definition of "ML" by inspection of the TPD spectra in Figure 2 of their paper.) Even though the submonolayer peak is near saturation at that coverage, it is clear from careful inspection that it continues to grow at higher coverages, so that the first layer is not complete until a higher coverage than 1.0 $ML_{Tylinski}$. Instead, it seems more logical that in that study, the first layer was completed at the midpoint of the 10−15 kJ/mol drop in E_{des} with coverage they reported at 1.2−1.5 $ML_{Tylinski}$. As shown above, the first layer completes at a coverage of ~0.25 acetonitrile molecules per Pt surface atom. We have thus adjusted the coverage axes in the two curves in Figure 3-3 such that 1.28 $ML_{Tylinski}$ corresponds to 0.25 acetonitrile molecules per Pt surface atom.

As seen, with this adjustment, desorption energies versus coverage from the calorimetry results are in excellent agreement with those determined by TPD. The discrepancy at very low coverages is likely due to a higher concentration of surface defects (step sites) for the Pt(111) surface used for TPD than that used for calorimetry. Further, the multilayer heat of 43.4 ± 1.7 kJ/mol obtained from calorimetry is within the error bars of the activation energy of 44 ± 3 kJ/mol determined by Tylinski et al. from leading-edge analysis of the multilayer desorption peak (which can be corrected to a heat of adsorption by adding $1/2RT$ = 0.47 kJ/mol with T = 140 K). The strong agreement of these results provides a convincing confirmation of each study. Collectively, the combination of energetic data from calorimetry and structural information from

RAIRS performed by Tylinski et al. provides detailed insight into the nature and energy of surface adsorption and interaction of acetonitrile with Pt(111).

The adsorption of acetonitrile on Pt(111) was studied previously by SCAC but only at 298 K by Shayeghi et al[131]. The initial heat of adsorption reported there at 298 K (87 kJ/mol) is very close to that measured here at 100 and 180 K in Figure 3-2 (83−85 kJ/mol). However, the heat drops much more rapidly with coverage in those results at 298 K, and the saturation coverage (~0.18 ML) is lower. It is very clear from looking at the TPD spectra for acetonitrile on Pt(111) presented in Tylinski et al.[55] that most of the first layer of molecularly adsorbed acetonitrile desorbs well below 298 K, so it is not clear what species Shayeghi et al. were producing above ~0.05 ML. That SCAC study at 298 K[131] did not present the long-term and short-term sticking probabilities versus coverage, so it is difficult to assess how to interpret those data.

3.4.2 Monolayer Saturation Coverages

In the heats of Figure 3-2, saturation of the first layer appears to occur much later in the 100 K data, at a coverage of~0.35 ML, than at 180 K (0.25 ML). This can be explained by a closer analysis of acetonitrile adsorbate configurations, along with the lower surface mobility at 100 K which limits the ability for adsorbed molecules to arrange themselves in the most energetically stable configurations compared to those at 180 K. This also explains why the heat from ~0.2 to 0.25 ML is lower at 100 K than at 180 K in Figure 3-2.

Previous work using RAIRS[55,124,139], EELS[140], and computational methods[130–132] showed that the most stable orientation of the adsorbed acetonitrile molecule on Pt(111) is a bridged structure, referred to as the μ-configuration. This configuration was observed at temperatures as low as 60 K but is the dominant surface configuration observed above 110 K in vacuum[55]. In this

configuration, the C≡N triple bond becomes a C=N double bond, and new C−Pt and N−Pt bonds are formed, leaving the methyl group oriented away from the surface. Further, DFT calculations[130–132] suggest that the second most stable orientation, referred to as the N-top configuration, is bound to a single Pt surface atom via the lone pair on the N atom, with the acetonitrile molecule oriented perpendicularly to the plane of the surface. The N-top configuration thus requires a smaller area on the surface than the μ-configuration. The N-top configuration was observed from 60 to 110 K by RAIRS but was only present above 110 K in vacuum at coverages nearing and above saturation of the first layer (above 1 $ML_{Tylinski}$ or 0.19 ML per Pt surface atom)[55]. At the highest temperature they studied by RAIRS below 110 K (i.e., 60 K), there is not enough thermal energy for the adsorbates to overcome the activation barrier for the formation of the μ-configuration, and by coverages nearing the completion of the first layer, stearic constraints are present[55]. Additionally, SFG measurements for acetonitrile in the liquid phase at a Pt electrode interface also observed the formation of the N-top configuration due to stearic constraints introduced by the presence of solvents (ethanol, methanol, or water)[125,141].

At 100 K in UHV, all incoming acetonitrile molecules adsorb when they hit the surface, regardless of the local surface coverage where they hit, as evidenced by the unity sticking probability at high coverage. The heat stays much higher than in the second layer up to at least 0.25 ML (Figure 3-2), implying that they transiently adsorb when landing on top of preexisting adsorbates and diffuse rapidly to find an adsorbate-free site to bind strongly to the Pt atoms below, as commonly occurs when organic molecules adsorb on late transition-metal surfaces[2]. As the first adsorbate layer nears saturation, stearic constraints arise which inhibit the formation of the μ-configuration, which requires multiple adjacent, unoccupied Pt surface atoms. This

surface temperature is apparently cold enough to both prevent desorption as well as prevent μ-bonded molecules from moving apart to create larger free metal sites to accommodate the more favorable μ-configuration. So, some molecules only have enough space to form the N-top configuration. The resulting surface adlayer is a combination of μ and N-top configurations, enabling the formation of a higher-density first layer that saturates by ~0.35 ML. This is consistent with RAIRS data showing the presence of both configurations on Pt(111) at 120 K at coverages near and above saturation of the first layer[55].

In contrast, the saturation coverage at 180 K is only 0.25 ML. As the first layer nears saturation at 180 K, any incoming adsorbate molecules that land at a less favorable site can migrate to a more favorable site or wait until thermal fluctuations create more open space to allow it to convert to the most stable μ-configuration. Again, RAIRS data observed the formation of the N-top configuration only below 110 K or at coverages higher than a single layer, but never at 180 K, which is too hot to form more than a single layer[55]. Thus, thermal motion at 180 K enables the formation of an adsorbate layer dominated by the more stable μ-configuration, as seen in literature for adlayers deposited over the range of 120−140 K[55]. This results in a less densely packed first layer that not only saturates by 0.25 ML but also makes the higher temperature (180 K) results in Figure 3-2 a more accurate approximation of the most stable structure of the first layer and its heat versus coverage. DFT calculations have shown that the μ-configuration is stable at a coverage of 0.25 ML (i.e., one per 2 × 2 unit cell)[130–132], consistent with the saturation coverage we measure here at 180 K of 0.25 ML. This is further supported by LEED studies that have observed a (2 × 2) overlayer structure for acetonitrile adsorbed on Pt(111) and Ni(111). On Pt(111), the (2 × 2) overlayer was observed up through coverages of

0.19 ML but was no longer present by a coverage of 0.36 ML[137]. For Ni(111), the acetonitrile saturation coverage at 190 K was found to be a (2 × 2) overlayer[138].

3.4.3 Adhesion Energy

Given how commonly acetonitrile is used as a solvent, determination of the adhesion energy of liquid acetonitrile on Pt(111) can provide valuable insight into the energetics of the liquid−solid interface. It has been shown that solvent−metal adhesion energies are the dominating factor that determines differences in reactant adsorption energies in different solvents or in any solvent relative to gas-phase adsorption energy measurements[44,123]. Solvent adhesion energies allow one to quantitatively estimate the effects of different solvents on the adsorption energies of catalytic reaction intermediates[123]. Thus, it is highly desirable to measure the adhesion energy of acetonitrile to Pt(111) to enable the prediction of adsorption energies of molecules to Pt(111) in an acetonitrile solvent. However, there is currently no way to directly measure the adhesion energy of a liquid solvent to a clean metal surface.

To estimate this adhesion energy, we will employ a recently developed method from this group[44,123]. This method used a standard thermodynamic cycle to derive a relationship between the adhesion energy of a solvent and the experimentally determined differential heat of adsorption data like that in Figure 3-2. Notably, this requires heat versus coverage measurements out to multilayer coverages of the solid solvent and that the coverage has known absolute units. This derived relationship is presented in Equation 3-1, where $E_{adh,S(liq)/M(s)}$ is the adhesion energy of the liquid solvent to the solid metal and $\gamma_{S(liq)}$ is the surface energy of the liquid solvent at its gas or vacuum interface[44]

$$E_{adh,S(liq)/M(s)} = \frac{\left[Q_{adsorption} - n \cdot \Delta H_{vap,S}\right]}{A} + 2 \cdot \gamma_{S(liq)} \quad (3\text{-}1)$$

As shown in this derivation[44], $\gamma_{S(liq)}$ is multiplied by 2 here because, in the thermodynamic cycle used there, the first step is to produce (from gas molecules) a free-standing liquid slab, whose energy is higher than bulklike liquid by $\gamma_{S(liq)}$ times the area of both the top and the bottom surfaces of the slab. The term $[Q_{adsorption} - n \cdot \Delta H_{vap,S}]/A$ here is equal to the integrated area from zero coverage up to a (bulklike) multilayer coverage (with n moles adsorbed per area A) of the heat-versus-coverage curve ($Q_{adsorption}$) minus n/A times the molar heat of vaporization of the liquid solvent ($\Delta H_{vap,S}$). Ideally, these values would all be measured at room temperature to provide the adhesion energy at room temperature. Since $Q_{adsorption}$ can only be measured on a clean metal surface in ultrahigh vacuum, which is only possible for acetonitrile at temperatures where the solvent grows as solid films rather than liquid films, the assumption was made that the term $[Q_{adsorption} - n \cdot \Delta H_{vap,S}]/A$ at room temperature is approximately equal to the analogous quantity at experimental temperatures where the solvent is a solid, or $[Q_{adsorption} - n \cdot \Delta H_{sub,S}]/A$, where $\Delta H_{sub,S}$ is the heat of sublimation of bulk acetonitrile (see references[44,123] for justification of this assumption). We evaluate this quantity from the heat data in Figure 3-2 at 100 K as its integrated area above the solid horizontal line shown (at the bulk heat of sublimation). This is equivalent to assuming that the difference in the heat capacities (including the heat of fusion) between the first and subsequent layers of acetonitrile is negligible when heating from 100 to 300 K.

Using this method and the reported surface tension of bulk, liquid acetonitrile of $\gamma_{S(liq)}$ = 0.02866 J/m^2 [142], we calculate the adhesion energy of liquid acetonitrile to the Pt(111) surface at 100 K to be E_{adh} = 0.198 J/m^2. Comparatively, this value is slightly greater than the adhesion energies of formic acid and methanol to Pt(111) (0.162 and 0.168 J/m^2, respectively) but considerably below that of water, benzene, and phenol (0.273, 0.447, and 0.468 J/m^2,

respectively)[44]. Understanding this adhesion energy, and particularly how it compares to other common solvents, could enable the intelligent selection among these solvents, or mixtures thereof, to tune reaction environments to have more desirable energetics for surface adsorption or desorption for catalytic reactants and intermediates. We note that these adhesion energies were all estimated using the same assumption of a negligible difference in heat capacities (including the heat of fusion) between the first and subsequent layers, and the errors associated with this assumption are possibly large (~25%). However, all of these errors are probably qualitatively similar, so these trends in E_{adh} values will remain. It is expected that computational approaches could provide estimates of the corrections needed for this heat capacity approximation.

We next show that this acetonitrile/Pt(111) adhesion energy can be used to estimate the adsorption energy of uncharged adsorbed catalytic reaction intermediates on Pt(111) in liquid acetonitrile solvent based on their far better-known values in the gas phase. The adsorption energy in acetonitrile is approximately equal to the gas-phase adsorption energy minus this adhesion energy times the area occupied on the surface per mole of the adsorbate. This is based on a bond-additivity type model which was used recently to derive a relationship between the adsorption energy of an adsorbate in a gas phase and the adsorption energy of that adsorbate in a liquid solvent[123]. Utilizing a thermodynamic cycle, a constant was derived to quantify the difference in these adsorption energies as a result of the presence of a solvent. This model was originally only for flat adsorbates (like benzene and phenol), but it was recently extended to adsorbates of arbitrary shape[42]. This relationship is presented below in Equation 3-2, where $\Delta U_{ads,R(solvent)}$ is the adsorption energy of the adsorbate in a solvent, $\Delta U_{ads,R(gas)}$ is its adsorption energy in a gas phase, and the remaining bracketed term is the constant[42]

$$\Delta U_{ads,R(solvent)} = \Delta U_{ads,R(gas)} + \left[E_{adh,S/M} - \frac{\Delta U_{solvation,R(gas)}}{\sigma_{tot}} - \gamma_{S(liq)} \right] \sigma_R \qquad (3\text{-}2)$$

The difference in adsorption energy is composed of the adhesion energy of the solvent to the surface ($E_{adh,S/M}$), the gaseous adsorbate's solvation energy per unit molecular area ($\Delta U_{solvation,R(gas)}/\sigma_{tot}$), and the solvent's surface energy ($\gamma_{S(liq)}$), all multiplied by the footprint area of the adsorbate on the surface (σ_R). This equation is independent of the shape of the adsorbate other than the fact that the shape determines the ratio of the total outer surface area of the adsorbate (σ_{tot}) and the footprint of the adsorbate on the surface upon adsorption (σ_R). This constant is dominated by the solvent adhesion energy term, as the remaining terms are smaller, opposite in sign, and nearly cancel. The errors on this estimated constant are probably rather large (up to 30%), but we expect that it will capture the trends with changing solvents and adsorbates reasonably well. The determination of the adhesion energy of acetonitrile on Pt(111) therefore allows for the quantification of this constant and consequently the effect of acetonitrile as a solvent on the adsorption energy of any adsorbing species on Pt(111) for which the gas-phase adsorption energy is known. This model, combined with this adhesion energy, provides a powerful tool for improving the understanding and computational models for liquid-phase reactions on Pt(111) that use acetonitrile as a solvent, and in combination with previously published values for other solvents and catalyst surfaces[42,44], liquid-phase heterogeneous catalysis in general.

3.5 Conclusions

The energetics of molecular adsorption of acetonitrile on Pt(111) were measured by SCAC, as a function of coverage. At 180 K, the integral heat of adsorption is 74.3 kJ/mol at a saturation coverage of 0.25 ML and well fit at lower coverages by (82.9−34.4θ) kJ/mol. At 180 K, the initial differential heat of adsorption is 82.9 kJ/mol, which decreases to 63.2 kJ/mol by

0.25 ML. At 100 K, the initial heat of adsorption is 84.5 kJ/ mol, which decreases to ~45 kJ/mol at the completion of the first layer (0.35 ML), and finally drops to a multilayer heat of 43.4 kJ/mol above coverages of 0.7 ML. This difference in saturation coverage of the first layer at 100 versus 180 K is a result of the formation of two different surface adsorbate configurations, μ and N-top, with the former being more energetically favorable but the latter arising in the presence of stearic constraints, which are present at 100 K due to lower adsorbate mobility across the surface. These present results agree well with recent TPD and RAIRS studies, and collectively these results provide a clear understanding of the nature of the interaction between acetonitrile, the simplest organic nitrile, and Pt(111).

Using the 100 K heat of adsorption curve measured out to multilayer coverages, we estimate the adhesion energy for liquid acetonitrile to Pt(111) to be 0.198 J/m^2. This is slightly higher than that of formic acid and methanol to Pt(111) but considerably lower than that of water, benzene, and phenol. This adhesion energy is useful for estimating the effects of acetonitrile as a solvent on the adsorption energies of catalytic reaction intermediates of interest in liquid-phase catalytic and electrocatalytic reactions.

3.6 Figures

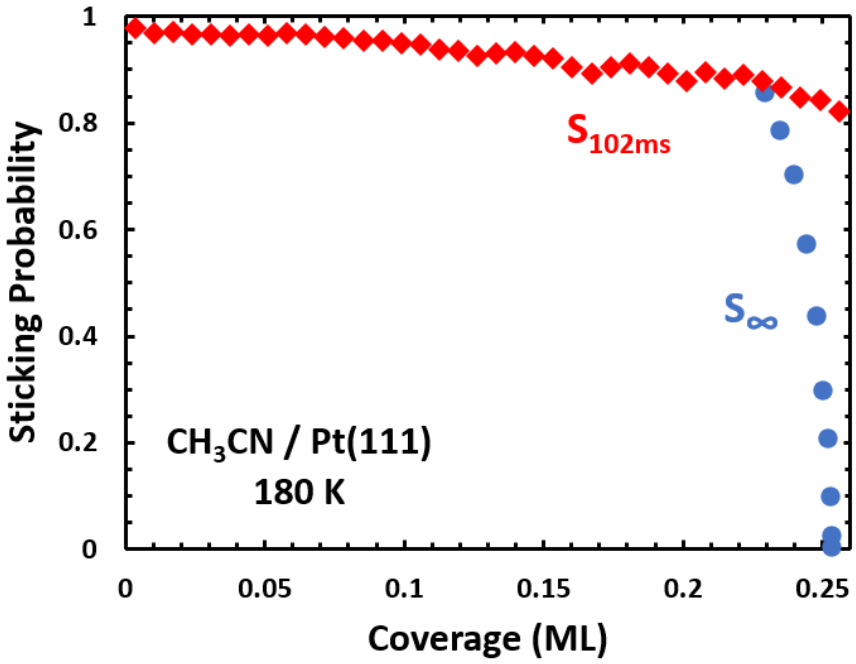

Figure 3-1. Average short-term (red, S_{102ms}) and long-term (blue, S_{∞}) sticking probabilities of acetonitrile on Pt(111) at 180 K as a function of acetonitrile coverage. A coverage of 1 ML is defined as one adsorbate per Pt(111) surface atom, or 1.50 x 10^{19} adsorbates/m^2. The short-term and long-term sticking probabilities were indistinguishable (within the noise) below 0.23 ML, so only one is shown.

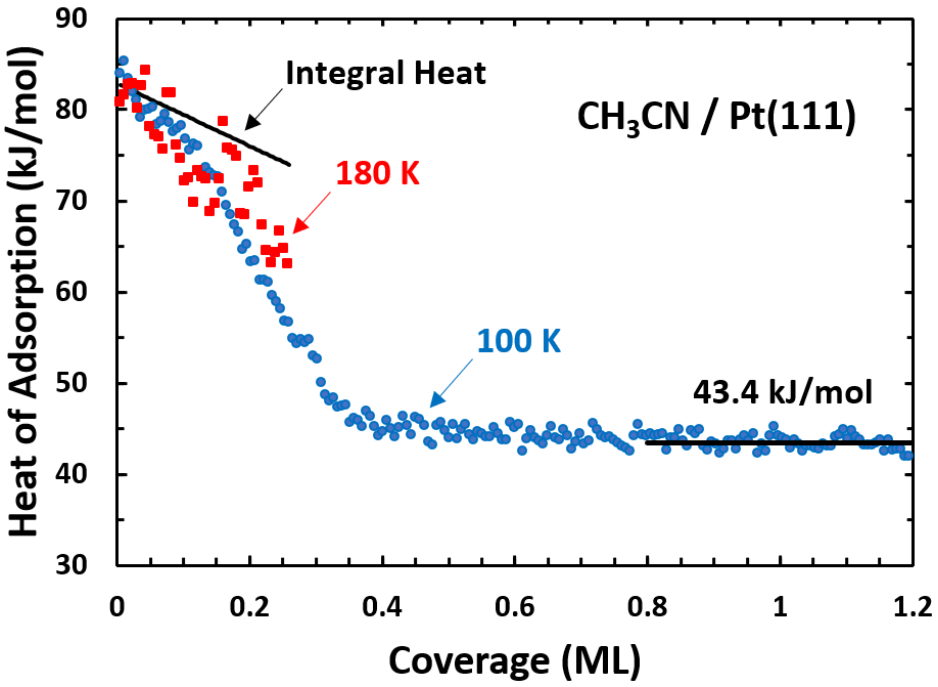

Figure 3-2. Differential heats of adsorption of acetonitrile on Pt(111) at 100 K (blue circles) & 180 K (red squares) as a function acetonitrile coverage. The average heat of adsorption reached at the multilayer limit is shown by the black line through the 100 K data. The integral heat of adsorption for 180 K is shown in black from the low coverage limit, fit by (82.9 – 34.4θ) kJ/mol and giving 74.3 kJ/mol at saturation (θ = 0.25 ML). 1 ML = 1.50 x 10^{19} molecules/m^2.

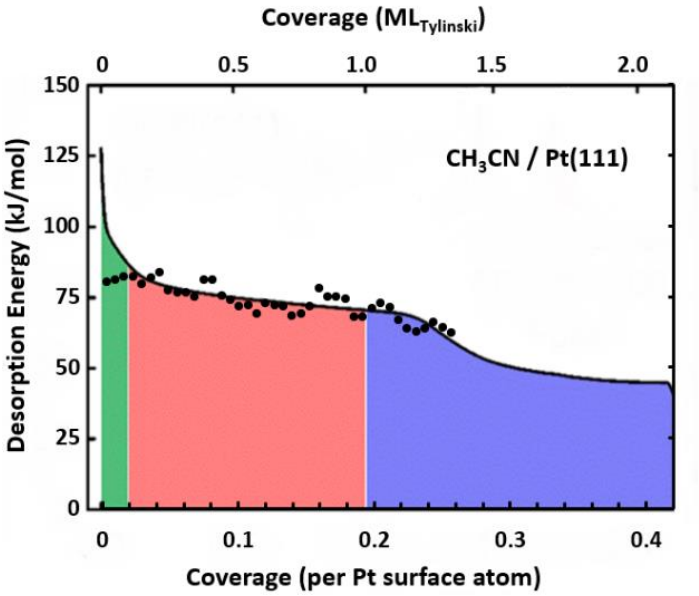

Figure 3-3. Comparison of the desorption energy of acetonitrile from Pt(111) as a function of acetonitrile coverage as determined from the differential heats measured in this work (black points) to the values determined by Tylinski et al.[55] in a very careful TPD study (solid curve). The bottom x-axis coverage is defined as in Figures 3-1 and 3-2, i.e., relative to the density of Pt atoms on the (111) surface (1.50×10^{19} atoms/m^2), while the top x-axis is in units as defined by Tylinski et al., where 1 ML$_{Tylinski}$ was the highest coverage of acetonitrile that showed no multilayer desorption peak in TPD. In this plot, we adjusted 1.0 ML$_{Tylinski}$ to correspond to 0.195 ML (per Pt surface atom) to align the steepest (broadened steplike) drop in desorption energy versus coverage in Tylinski's data with the saturation coverage at 180 K (black points), which we assumed here to correspond to completion of the first layer of adsorbed acetonitrile at 0.25 ML (see text). The green, red, and blue shadings are from Tylinski et al. and were intended to separate the regions where TPD features were seen associated with step sites, (111) terraces in the first layer, and coverages where the multilayer TPD peak was also seen, respectively. We note that the TPD peak area associated with terrace sites continued to grow considerably in this blue region, which explains why 1.0 ML$_{Tylinski}$ corresponds to a lower coverage than 0.25 ML.

Chapter 4 n-Decane Adsorption and Adhesion Energies on the Pt(111) Surface by Calorimetry

Chapter Abstract

The heat of adsorption of *n*-decane molecularly adsorbed on Pt(111) at 150 K was measured by single crystal adsorption calorimetry. The heat of adsorption was initially 151.8 kJ/mol on terrace sites up to a coverage of $\theta = 0.045$ ML . A heat of 169 kJ/mol was measured on defect sites, likely due to adsorption at step edges. At coverages above $\theta = 0.27$ ML the multilayer heat of adsorption was 84.9 kJ/mol. This was compared to TPD measurements of the desorption energy of *n*-alkanes on Pt(111) (C_1 to C_6) and the predicted value for the desorption energy of *n*-decane which was found to be in good agreement with SCAC measurements. Using the heat of adsorption at 150 K up through the bulk-like multilayer coverages we estimate the adhesion energy of liquid *n*-decane on Pt(111) to be 0.148 J/m^2. This is very similar to the adhesion energy per unit area of liquid *n*-hexane on Pt(111) which shows that while adsorption energy increases with the number of CH_2 groups, as adhesion energy is a per unit area value the adhesion energy is nearly a constant (0.15 J/m^2).

4.1 Introduction

It is of great interest to understand the energetics of solvent bonding to catalytically relevant materials, since these energetics to a larger extent determine how different solvents affect the heats of adsorption of catalytic reaction intermediates to the catalyst surface. It has been shown, for example, that the heat of adsorption of neutral reaction intermediates decreases in a particular solvent (relative to the gas phase) by an amount equal to the adhesion energy per unit area (E_{adh}) of that liquid solvent to the surface times the area on the surface occupied by that adsorbed intermediate (i.e., the area where solvent can no longer bind to the surface due to blocking by the adsorbate).[42,44,57,143] Understanding how different solvents affect adsorption energies of intermediates aids in our fundamental understanding of solvent effects on catalytic activity and selectivity, and in the improvement and design of catalytic processes. Here we report calorimetric measurements of adsorption energy versus coverage for *n*-decane on Pt(111) at 150 K, and use these gas phase measurements to estimate the adhesion energy of liquid *n*-decane on Pt(111) at room temperature. We compare this adhesion energy to the estimated energies of other linear alkanes on the Pt(111) surface to examine the relationships between adsorption energy, adhesion energy and size of these linear alkanes. The adsorption energy is nearly proportional to chain length, whereas E_{adh} is nearly independent of chain length.

The adsorption energy of *n*-decane on Pt(111) is also of fundamental interest since hydrocarbon reactions on Pt catalysts are ubiquitous in petroleum and biomass catalysis, and the Pt(111) surface is the most widely studied model of Pt catalyst surfaces. Neither its adsorption energy nor desorption activation energy were previously known. While the desorption energy of shorter linear alkanes (C_6 and smaller) on Pt(111) was previously measured using temperature programmed desorption (TPD), *n*-octane and *n*-decane did not desorb completely reversibly

(they partially dissociated instead), and thus their desorption energies could not be measured using TPD.[144] Single crystal adsorption calorimetry (SCAC) allows for the direct measurement of the heat of adsorption versus coverage of molecules that do not desorb reversibly.[22] With a small correction, this heat of adsorption can be converted to the desorption activation energy that is measured by TPD.[23]

4.2 Experimental Methodology

The experiments were conducted in an ultrahigh vacuum (UHV) chamber (base pressure $<2 \times 10^{-10}$ mbar) designed for single-crystal adsorption calorimetry (SCAC). The chamber also has in-situ instrumentation for X-ray photoelectron spectroscopy (XPS), low-energy electron diffraction (LEED), Auger electron spectroscopy (AES), low-energy ion-scattering spectroscopy (LEIS), a quadrupole mass spectrometer (QMS), and a liquid-nitrogen cooled quartz crystal microbalance (QCM). The SCAC apparatus and experimental procedures for the molecular beam flux, sticking probability, and heat measurements have been described in detail previously.[26,145,146]

In brief, the 1μm thick Pt(111) single crystal sample was provided from Bine Hansen at Aarhus University. The crystal surface was cleaned by repeated cycles of Ar^+ ion sputtering and annealing to 1120 K, which was proven in earlier studies with this same apparatus to give a clean and well-ordered Pt(111) surface.[147] The Pt(111) surface was exposed to a pulsed, collimated molecular beam of *n*-decane, and the heat of adsorption and sticking probability were recorded simultaneously. The sticking probability was measured by the King and Wells method with a QMS, and the heat of adsorption was measured using a pyroelectric polymer ribbon in contact with the back of the Pt(111) crystal. The molecular beam was created by expanding 1.0 mbar of

n-decane through a glass capillary array heated to 335 K and collimated via a series of liquid-nitrogen cooled orifices. This beam was then chopped into 102 ms pulses every 3 s.

Here, one monolayer (ML) of coverage is defined as the number of molecules of *n*-decane adsorbed to the surface per unit area, normalized to the surface density of Pt(111) atoms (1.50×10^{19} molecules/m^2). A typical beam pulse consists of approximately 0.002 ML (~4.7 x 10^{11} molecules within the beam diameter of ~4 mm) per *n*-decane gas pulse.

4.3 Results

4.3.1 Sticking Probabilities

Long-term and short-term sticking probabilities of *n*-decane on Pt(111) were found to be unity at 150 K. The long-term sticking probability refers to molecules that initially adsorb and remain adsorbed for the entire duration of the 3 s pulse window and contribute to the build-up of coverage of *n*-decane on the surface. The short-term sticking probability refers to the molecules that initially adsorb and contribute to the measured heat of adsorption during the 102 ms pulse, but then desorb before the next pulse and do not add to the coverage. When both sticking probabilities are unity, as with *n*-decane on Pt(111) at 150 K here, all incoming molecules adsorb to the surface and remain adsorbed until the next pulse, fully contributing to the both the measured heat and coverage increase.

4.3.2 Heats of Adsorption

We define here the "heat of adsorption" as the negative of the standard molar enthalpy change for the adsorption reaction, with the gaseous molecules and single crystal surface being the same temperature. As explained in detail in previous papers, this requires a small enthalpy correction on the measured heat as the gas molecule's enthalpy at this temperature is slightly

different than a Boltzmann distribution at the sample temperature due to the actual molecular beam conditions.[146] The differential heat of adsorption measured is the heat released per mole when a pulse from the molecular beam is dosed onto the crystal surface at nearly fixed coverage, as is the case during our SCAC experiments here since the gas pulses contain only ~0.2 % of a ML. Figure 4-1 shows the differential heat of adsorption of *n*-decane on Pt(111) at 150 K as a function of *n*-decane coverage. This is the average of 6 experimental runs. After the first two gas pulses, the heat of adsorption at 150 K is nearly constant at 151.8 ± 5.4 kJ/mol up to 0.045 ML. The heat is slightly higher (~169 kJ/mol) in the first two points, which has often been seen in SCAC measurements on the Pt(111) surfaces we studied in this apparatus. This has been attributed to defect sites on the surface, likely step edges.[38] Above 0.06 ML, the heat of adsorption drops rapidly to ~90 kJ/mol at ~0.09 ML. It stays near 90 kJ/mol until above ~0.20 ML, then decreases to a constant multilayer heat of 84.9 ± 5.5 kJ/mol above 0.27 ML which corresponds to coverage of more than three layers of *n*-decane on the Pt(111) surface.[27] There error bars here reflect the run-to-run standard deviation on the average multilayer heat measured above 0.27 ML. Since there were six runs, the error bar on the average multilayer heat is smaller (~± (5.5 kJ/mol)/(6-1)$^{1/2}$ = ± 2.5 kJ/mol). This multilayer heat can be compared to the bulk heat of sublimation of n-decane at this temperature, which we estimate to be 87.4 kJ/mol at 150 K based on literature values for the heat capacities of solid, liquid and gaseous *n*-decane, and the enthalpies of vaporization and fusion[134,136].

Linear n-alkanes on Pt(111) have first-layer packing densities that depend on the number of carbons per alkane, n, whereby 1/(n + 1) is the coverage (per Pt surface atom) of the first layer of adsorbate.[27] For *n*-decane, where n = 10, this predicts a coverage of 1/11= 0.091 ML for completion of the first layer. This is in excellent agreement with the abrupt change in the slope

of heat versus coverage, where the high heat measured in the first layer has deceased rapidly to 90 kJ/mol (at completion of the first layer), and then quickly becomes nearly constant with coverage at ~90 kJ/mol (in the second layer).

4.4 Discussion

4.4.1 Comparison to TPD

Previously Tait et.al.[144] measured the desorption energy of various *n*-alkanes on Pt(111), C(0001)/Pt(111) and MgO(100). However, on Pt(111) the longest alkane that that reversibly desorbed without significant dissociation was *n*-hexane, so no longer alkanes were studied there. Here, measuring the heat of adsorption of *n*-decane on Pt(111), and correcting for comparison to desorption energy values measured from TPD by subtracting ½ RT, we can compare these experimental results to the value predicted in that work. Taking the linear trend line reported by Tait et al. for the desorption energies for *n*-alkanes (from C_1 to C_6) on Pt(111) at a coverage of 0.5 "ML" versus chain length we can predict a desorption energy of *n*-decane on Pt(111) of 129.5 kJ/mol. It's important to note that Tait et al. defined 1 "ML" as their highest measured coverage where they saw only the monolayer desorption peak with no multilayer peak visible, which is close to one complete layer of *n*-alkanes adsorbed on the surface. We define 1 ML here differently, as one molecule of *n*-decane adsorbed to the surface per surface Pt atom (or 1.50×10^{19} molecules/m^2). As Tait et al. measured desorption energies at 0.5 "ML" by their definition, this corresponds to 0.5 x 0.091 ML =0.0455 ML of decane in our ML units here.

We measured a differential heat of adsorption at 0.0455 ML of 151.8 kJ/mol, which corresponds to a desorption energy of 151.2 kJ/mol after applying the -1/2RT correction for direct comparison to TPD measurements.[23] This is 21.7 kJ/mol higher than the desorption energy

of 129.5 kJ/mol predicted above at this coverage (i.e., half the coverage which completes the first layer) based on those TPD studies of shorter alkanes by Tait et al. Those TPD studies indicates that near the peak temperature for desorption, these alkanes make close-packed 2D islands over nearly the full first-layer coverage range, where their desorption energy remains nearly constant with coverage. Our measured integral heat at completion of the first layer (0.091 ML) is 132.7 kJ/mol, which corresponds to a desorption energy of 132.1 kJ/mol. This average heat for the first layer is very close to the average value of 129.5 kJ/mol measured by TPD.

The nearly constant heat of adsorption observed up to 0.045 ML (except defect effects) seen in Figure 4-1 suggests adsorption of *n*-decane in 2D islands, which was observed for the other shorter *n*-alkanes studied on Pt(111), and also up to decane on MgO(100) and graphene, by Tait et al.[144] The decrease in heat seen here above 0.06 ML (~2/3 of the first layer completion) may be due to the lower temperature studied here (150 K, versus 200 and 250 K for MgO and graphene, respectively). Decane molecules on Pt(111) at 150 K here may not be mobile enough at high coverages to achieve their optimum packing configuration to maximize decane-decane attractions. Note too that decane's higher heat of adsorption on Pt(111) suggests that it will have higher surface diffusion barriers than on MgO and graphene.

4.4.2 Adhesion Energy

There is great interest in understanding the energetics of solvents at the liquid-solid interface. The adhesion energy at the solvent-metal interface is the controlling factor in the differences between reactant adsorption energies in various solvents relative to its gas-phase adsorption energy.[42,44,57,143] Using the method previously described by Rumptz et al.,[44] we can estimate the adhesion energy of bulk liquid *n*-decane to Pt(111) at room temperature from the heats of adsorption in Figure 4-1 at 150 K. Equation 4-1 shows how the adhesion energy of the

liquid solvent to the solid metal surface ($E_{adh,S(liq)/M(s)}$) is estimated in that method from the integrated heat of adsorption of the solvent (*S*), here *n*-decane on the Pt(111) surface:

$$E_{adh,S(liq)/M(s)} = \frac{\left[Q_{adsorption} - n \cdot \Delta H_{vap,S}\right]}{A} + 2 \cdot \gamma_{S(liq)} \quad (4\text{-}1)$$

In the first term, the integrated heat of adsorption at a thick multilayer coverage ($Q_{adsoprtion}$) minus the number of moles adsorbed (*n*) times the molar heat of vaporization of the solvent ($\Delta H_{vap,S}$) is divided by area covered by the adsorbed film (*A*). The second term is twice the surface energy of the solvent (decane here) as a bulk liquid ($\gamma_{S,liq}$). For this, we use the reported surface tension of bulk, liquid decane at 298 K, $\gamma_{S,liq}$ = 0.02383 J/m^2.[57] It is only possible to form multilayers of *n*-decane on Pt(111) in ultrahigh vacuum at low temperatures (here 150 K), where the incoming molecules adsorb to form a solid instead of a liquid. We make the assumption that $[Q_{adsorption} - n\Delta H_{vap,S}]$ at room temperature is approximately equal to $[Q_{adsorption} - n\Delta H_{sub,S}]$ measured at our lower experimental temperature of Figure 4-1 (150 K), where $\Delta H_{sub,S}$ is the heat of sublimation of bulk *n*-decane at this same temperature (taken to equal the limiting multilayer differential heat measured in Figure 4-1 at thick multilayer coverages, 84.9 kJ/mol). This assumes that the molar heat capacity of the solvent molecules in the first adsorbed layer equals that in the bulk multilayer at all temperatures between 150 K and 298 K (including the contributions from their heats of fusion).[44,57] Thus, we estimate from the data in Figure 4-1 that the adhesion energy of *n*-decane on Pt(111) is 0.148 J/m^2.

In Figure 4-2 we plot the adhesion energies of various *n*-alkanes on Pt(111), graphene on Pt(111), and MgO(100) surfaces versus chain length, n. Except for decane on Pt(111), these points are all taken from Rumptz et al.,[57] who extracted them from TPD measurements[144] also using Equation 4-1.

Based on the trends seen in Figure 4-2 for MgO and graphene and as discussed by Rumptz et al.,[57] we expected that the adhesion energy of linear alkanes would be approximately constant as chain length increases. Though the adsorption energy of *n*-decane is higher than that of the shorter alkanes,[144] adhesion energy is a per area value (J/m^2), and the adhesion energy does indeed remain the nearly the same for decane as seen for *n*-hexane on Pt(111).

This work now extends this understanding to systems that desorb irreversibly, by filling in the missing *n*-decane on Pt(111) adhesion energy. Not only do we see the expected independence of adhesion energy from chain length, but we also confirm that both TPD and experimental heats of adsorption can be used to determine the adhesion energies of bulk liquids on a surface. As there is no way to currently directly measure adhesion energies on clean metal surfaces, this indirect technique used in Figure 4-2 has great value in providing new insights using previously measured heats of adsorption, or desorption energies, of solvent molecules at lower temperature.

4.5 Conclusions

The heat of adsorption of *n*-decane on Pt(111) versus coverage was measured using SCAC at 150 K. The initial heat of adsorption was nearly constant at 152 kJ/mol though 0.0455 ML (except for the first two points below 0.004 ML, which were ~17 kJ/mol higher and attributed to defect sites). The heat then dropped to ~90 kJ/mol by 0.091 ML, then decreased to the multilayer heat of adsorption of 84.9 kJ/mol above 0.27 ML. The integral heat of adsorption at the saturation coverage of the first layer of adsorbed *n*-decane (0.091 ML) was 132.7 kJ/mol. This was close to that predicted based on desorption energies measured by TPD for shorter *n*-

alkane on Pt(111) (C_1-C_6), which were found by Tait et al.[144] to increase nearly proportional to carbon number.

Using the experimentally measured heat of adsorption versus coverage out to a bulk-like multilayer coverage, we estimate the adhesion energy of liquid *n*-decane on Pt(111) to be 0.148 J/m^2. This is very close to the adhesion energy per unit area of *n*-hexane on Pt(111) estimated based on TPD desorption energies. Thus, linear alkanes have average heats of adsorption in close-packed islands on Pt(111) which approximately equal to a constant (13.3 kJ/mol per C atom) times their total number of CH_2 plus CH_3 groups, but because each CH_2 and CH_3 group occupies nearly the same area on the surface, the adhesion energy per unit area is also nearly a constant (0.15 J/m^2).

4.6 Figures

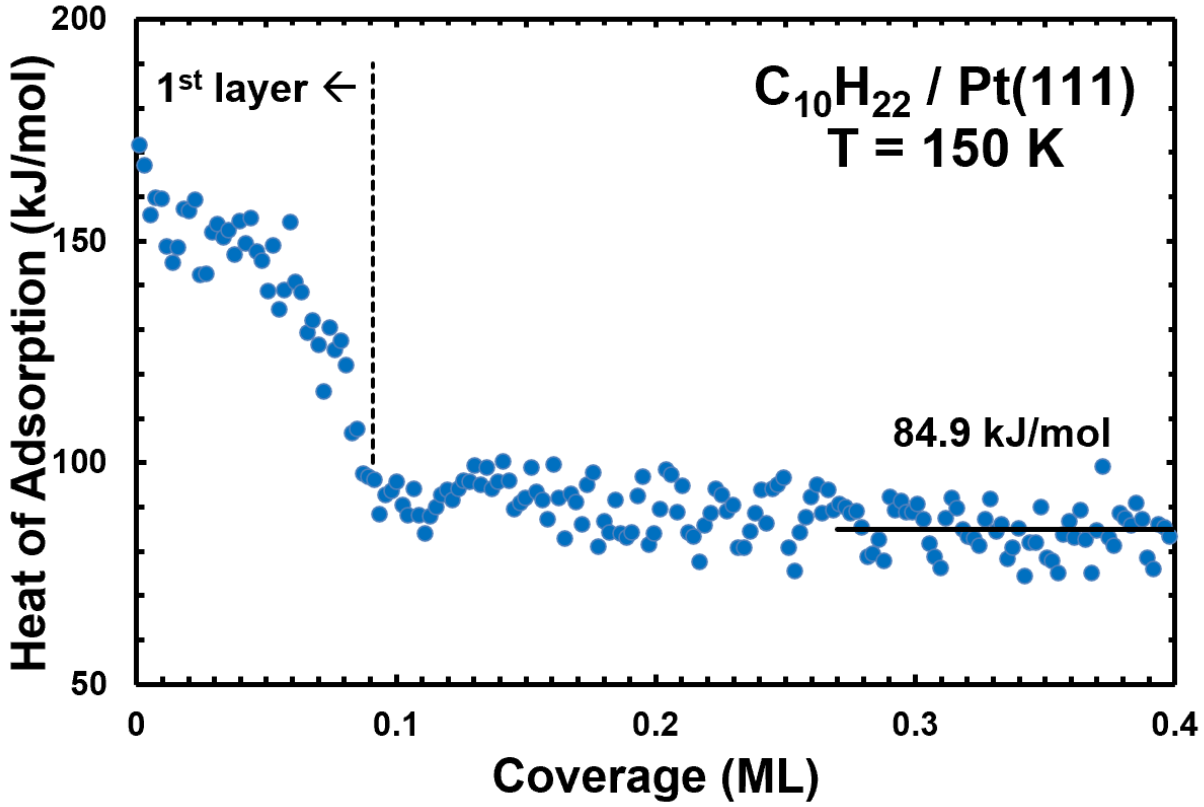

Figure 4-1. Differential heat of adsorption of n-decane on Pt(111) at 150 K as a function of n-decane coverage. The average heat of adsorption reached at the thick multilayer limit is shown by the black line. (1 ML = 1 molecule per Pt surface atom, or 1.50 x 10^{19} molecules/m^2.

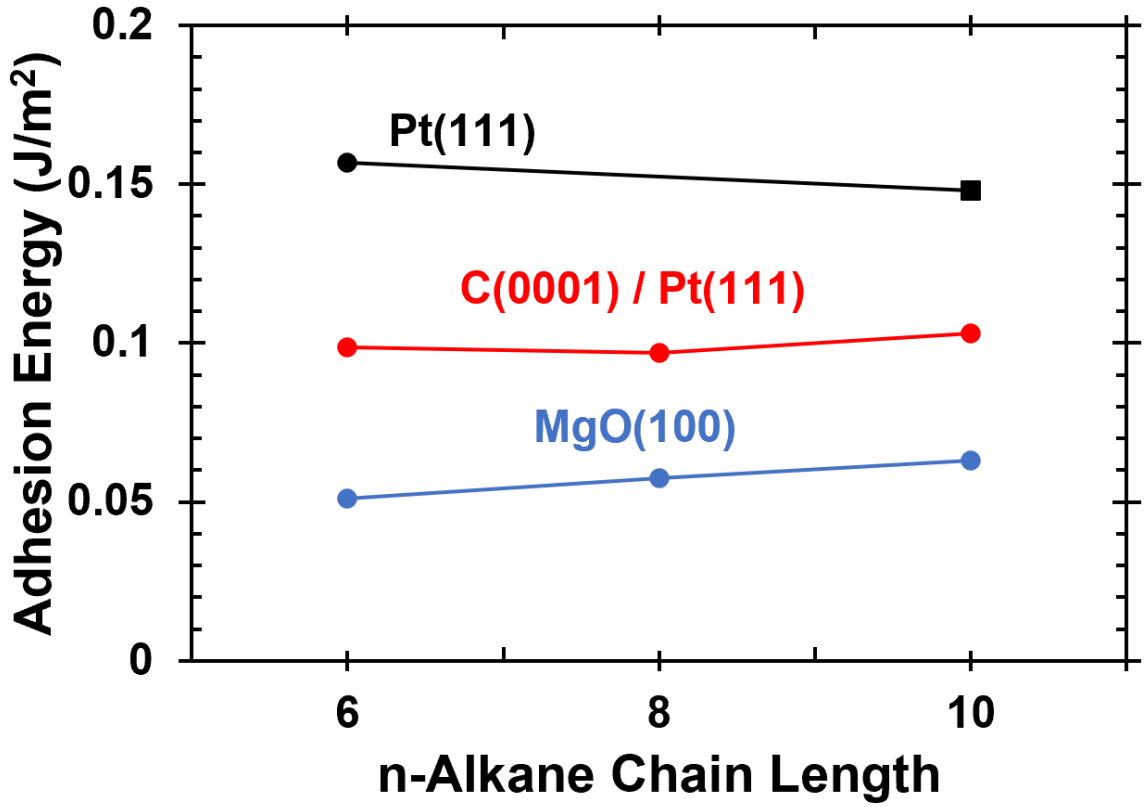

Figure 4-2. Adhesion energies of liquid n-alkanes versus chain length on three surfaces, estimated from low-temperature measurements of heats of adsorption versus coverage using Equation 4-1. Circular points were determined previously[57] using published TPD desorption energies,[144] while the square point is determined from the calorimetrically measured heat of adsorption of n-decane on Pt(111) in this work.

Chapter 5 Energetics of Adsorbed Azulene on Pt(111) by Calorimetry

This chapter has reprinted with permission from reference[61]:

Klein, B. P., Harman, S. E., Ruppenthal, L., Ruehl, G., Hall, S. J., Carey, S. J., Herritsch, J., Schmid, M., Maurer, R. J., Tonner, R., Campbell, C. T., & Gottfried, J. M. Enhanced Bonding of Pentagon − Heptagon Defects in Graphene to Metal Surfaces: Insights from the Adsorption of Azulene and Naphthalene to Pt(111). *Chemistry of Materials* **32**, 1041–1053 (2020).

Chapter Abstract

The performance of graphene-based (opto)electronic devices depends critically on the graphene/metal interface formed at the metal contacts. We show here that the interface properties may be controlled by topological defects, such as the pentagon−heptagon (5−7) pairs, because of their strongly enhanced bonding to the metal. To measure the bond energy and other key properties not accessible for the embedded defects, we use azulene as a molecular model for the 5−7 defect. Comparison to its isomer naphthalene, which represents the regular graphene structure, reveals that azulene interacts more strongly with a Pt(111) surface. Its adsorption energy, as measured by single-crystal adsorption calorimetry (SCAC), exceeds that of naphthalene by up to 116 kJ/mol (or up to 50%). Both isomers undergo hybridization of their frontier orbitals with metal states, as indicated by X-ray and ultraviolet photoelectron spectroscopy (XPS/UPS) and near-edge X-ray absorption fine structure (NEXAFS) spectroscopy combined with molecular orbital (MO) projection analysis through dispersion-corrected, periodic density functional theory (DFT) calculations. Based on the NEXAFS/DFT analysis, the stronger

bond of the 5−7 system is attributed to the different energetic response of its unoccupied frontier orbitals to adsorption. Adsorption-induced bond-length changes show substantial topology-related differences between the isomers. Electron transfer occurs in both directions through donation/back-donation, resulting in the partial occupation (deoccupation) of formerly unoccupied (occupied) orbitals, as revealed by periodic energy decomposition analysis (pEDA) for extended systems. Our model study shows that the topology of the π-electron system strongly affects its bonding to a transition metal and thus can be utilized to tailor interface properties.

It should be noted that I was not the primary author on the paper summarizing the research of this chapter. In this case, the published paper has been shortened to have a focus on the calorimetry research that I collected, as opposed to the DFT results that were conducted by Klein & Ruppenthal.

5.1 Introduction

Graphene as one of the most prominent two-dimensional (2D) materials is known for the exceptional electronic and mechanical properties of its ideal lattice[62]. Large-scale graphene samples, however, are typically polycrystalline and contain topological defects, such as pentagons, heptagons, and pentagon−heptagon (5−7) pairs (Figure 5-1a)[63], especially at grain boundaries[64–69]. These defects, which are induced by rearrangement of carbon−carbon (C−C) bonds, strongly influence the chemical and physical properties of graphene, including chemical reactivity[70,71], mechanical strength[68,69,72,73], electron transport[64,66], and magnetism[74]. Their utilization for tailoring the properties of graphene through topological design has been proposed[148].

Interfaces between graphene and metals are formed during the epitaxial growth of the 2D material on metallic substrates[75]. They also play a prominent role in graphene-based electronic devices, where metal contacts are necessary[76]. The properties of the resulting graphene/metal interfaces control important performance-determining parameters such as the contact resistance[149]. Considering the substantial influences of defects on the properties of graphene, it is likely that they also affect the interfacial interaction, as indicated by the reduced resistances observed for contacts to graphene edges[76]. However, the bonding of intrinsic graphene defects to metals is largely unexplored, mainly due to the experimental challenges arising from the investigations of embedded defects in low concentrations. Expanding on a recently introduced approach[86], we use here a molecular model system to study the bonding of 5−7 graphene defects to the reactive Pt(111) surface. In this model, azulene with its 5−7 ring structure represents the defect, whereas its isomer naphthalene is the reference molecule representing the hexagonal rings of defect-free graphene (Figure 5-1b,c). The 5−7 motif was chosen because it is the most

abundant building block for topological defects. It occurs in isolated 5−7 defects, in pairs as Stone−Wales defects, or in chains at grain boundaries. In addition, the 5−7 motif represents a class of defects for which a molecular model can be contrived, unlike vacancies. The model system approach allows for the application of laterally integrating techniques and thus provides unique access to parameters that cannot be measured for the real embedded defects, such as bond energies. Even though naphthalene is strongly chemisorbed on Pt(111)[60], we find here that azulene binds even stronger with adsorption energies that are up to 50% higher.

To concisely describe the topological properties of the defect, we use here the established concept of alternant versus nonalternant topology[150]. In the alternant conjugated system of naphthalene (and regular graphene), the carbon atoms can be labeled in an alternating fashion (e.g., red and green as in Figure 5-1b,c), while this is not possible for a nonalternant system like azulene (or the 5−7 defect). The nonalternant topology leads to the violation of the Coulson−Rushbrooke pairing theorem and thus to a distinctly different valence electronic structure[151]. In our model molecules, this electronic difference is manifested in the large dipole moment (0.8 D)[142] and intense blue color of azulene, whereas naphthalene has no dipole moment and is colorless.

The importance of nonalternant aromatic structures extends far beyond their role as graphene defects. Recently, they have found attention for application as molecular or polymeric organic semiconductors in organic (opto)electronic devices because of their low band gaps and high charge carrier mobilities[152]. Their interfaces to metal electrodes, which are known to strongly influence the properties of the device[153], have only rarely been studied, unlike interfaces to alternant aromatic systems[153]. Comparative studies of azulene and naphthalene on Pt(111) have not been reported. Limited work for the isolated systems was done with low-energy

electron diffraction (LEED)[77,79,80], temperature-programmed desorption (TPD)[77,79], and scanning tunneling microscopy (STM)[81–83]. Work function (WF) measurements[80], adsorption calorimetry[60], and density functional theory (DFT) calculations[85] were until now only performed for naphthalene on Pt(111). For the more weakly interacting Cu(111) surface, it was recently shown that naphthalene is physisorbed, while azulene is chemisorbed[86], raising the question whether differences in the interaction strength persist when both molecules are strongly chemisorbed.

In this study, we present a comprehensive multimethod comparison of the bonding of naphthalene and azulene to Pt(111). Using single−crystal adsorption calorimetry (SCAC), we measure the first reliable adsorption energies for any nonalternant aromatic molecule on any metal surface and show that it bonds stronger than its alternant isomer. Temperature-programmed desorption (TPD) cannot be applied here because the molecules do not desorb intact from Pt(111). DFT calculations including a dispersion-correction scheme (PBE-D3) and applying periodic boundary conditions are used to interpret the experimental data and to gain detailed insight into the underlying mechanisms of the enhanced bonding at the defect/metal interface.

5.2 Experimental Methodology

The adsorption of azulene and naphthalene on Pt(111) was studied under ultrahigh vacuum (UHV) conditions at base pressures below 2×10^{-10} mbar. Coverages are given in the unit monolayer (ML) defined as the number of molecules per platinum atom in the Pt(111) surface [atomic density of the Pt(111) surface: 1.50×10^{19} atoms/m^2]. If a “full monolayer” is

mentioned, this corresponds to one complete layer of molecules on the surface (which corresponds to 0.111 ML for azulene).

The SCAC experiments were performed in a UHV chamber equipped with facilities for XPS, LEED, Auger electron spectroscopy (AES), and low-energy ion-scattering spectroscopy (LEIS). The apparatus and procedures for SCAC have been described in extensive detail previously[25,26,58]. Briefly, the Pt(111) samples used in the SCAC experiments were 1 μm thick single-crystal foils and were provided by Jacques Chevallier at Aarhus University. The sample was cleaned by gentle Ar^+ sputtering, followed by repeated cycles of O_2 treatment at 10^{-6} mbar and 873 K and annealing at 1123 K in UHV. After this treatment, impurities were below the Auger and XPS detection limits, and LEED showed the spots expected for Pt(111). The heats of adsorption and sticking probability were measured simultaneously as a pulsed molecular beam of azulene was dosed onto the Pt surface. The molecular beam was created by expanding azulene vapor (0.2−0.9 mbar) through a glass capillary array, collimating it through a series of five orifices that were cooled with liquid nitrogen, and then chopping it into 102 ms pulses. The heats were measured with a pyroelectric ribbon gently pressed on the backside of the Pt crystal. The sticking probabilities were measured with a quadrupole mass spectrometer (QMS) using the King and Wells method[121].

Instrumental changes to the SCAC apparatus were required in order to sustain a constant flux of azulene, which remained solid substantially above room temperature with a melting point of 99° C. The normal glass reservoir for molecules of interest, which is attached to the molecular beam, had to be replaced by an entirely metal reservoir. Constant heating via heat tapes was applied to the reservoir and gas manifold through which azulene vapor traveled to reach the glass capillary array in the molecular beam. Even with these instrumental changes, the maximum

obtained vapor flux was still 2-4 fold less than any previous flux used for this apparatus. Collectively these changes expanded the potential systems that can be studied on the SCAC apparatus to include molecules with melting points substantially above room temperature.

5.3 Results and Discussion

5.3.1 Heat of Adsorption Measurements

The most important single parameter in this study is the heat of adsorption as a direct quantitative measure for the strength of the adsorbate−substrate bond. It is defined here as the negative of the differential standard molar enthalpy change for the adsorption reaction, $-\Delta H_{ads}$, with the gas having the same temperature as the surface. "Standard" here implies only an ideal gas at 1 bar pressure. Figure 5-2 shows the molar heat of adsorption of azulene on Pt(111) at 150 K as a function of coverage. These heats were calculated from the measured absolute calorimetric heats by averaging over five individual measurements, dividing by the number of moles adsorbed in each pulse (given by flux times pulse duration times sticking probability) and adding $RT_{source}/2$, as described previously[154]. No detectable mass spectrometer signal was present due to any nonsticking fraction of the azulene molecular beam, indicating that its sticking probability is always ≥0.995. Consequently, both the short- and long-term sticking probabilities were concluded to be unity.

As described previously, a small enthalpy correction on the measured heat is necessary because the standard enthalpy of a gas at the temperature of the surface differs slightly from that of the actual experimental molecular beam's gas at this surface temperature[155]. Specifically, the temperature of the source, T_{source}, and thus the temperature of the molecules impinging on the sample, is 382 K, which deviates from the sample temperature of 150 K. Therefore, we had to

take the additional contribution from the extra thermal energy of the gas molecules into account. We estimated this heat contribution by integrating the experimental heat capacity of the gas (C_p) versus T curve[58] between the sample and source temperature. The resulting heat, 29 kJ/mol, was subtracted from the directly measured heat. The thus corrected heat of adsorption is plotted versus coverage in Figure 5-2. It is equal to the standard (1 bar) molar enthalpy of adsorption and the isosteric differential heat of adsorption. Figure 5-2 shows that the heat of adsorption decreases with coverage. We attribute this decrease to repulsive lateral interactions among the adsorbed azulene molecules. The solid line is a second-order polynomial fit of the experimental data and is described by the equation $-\Delta H_{ads} = (416 - 1370 \cdot \theta - 13100 \cdot \theta^2)$ kJ/mol where θ is the coverage in monolayers (ML, given as molecules per surface atom).

The heat of adsorption of naphthalene on Pt(111) was already measured in previous work with the same instrument[60]. For a direct comparison with the new data, the old measurements for naphthalene were also fitted with a second-order polynomial and follow the equation $-\Delta H_{ads} = (300 - 330 \cdot \theta - 18758 \cdot \theta^2)$ kJ/mol. As can be seen, azulene has a substantially higher heat of adsorption than naphthalene over the whole coverage range, close to that expected for the larger anthracene[60].

Also shown in Figure 5-2 is the heat of sublimation of bulk azulene at 150 K. The literature value for the sublimation enthalpy of azulene is 74.2 ± 2.2 kJ/mol at 298 K[156]. This was adjusted to account for the lower temperature of the Pt(111) sample at 150 K by integrating the heat capacities (C_p) for gaseous and solid azulene over this temperature range. For gaseous azulene, values are available between 200 and 1000 K[157]. The third-order polynomial fit relating C_p to temperature was extrapolated to 150 K and integrated between 150 and 298 K. The only available value for C_p of solid azulene is given at 298 K[158]. To determine the C_p of solid azulene

at a lower temperature, we assessed the solid C_p values for the similar molecules naphthalene and benzene. The heat capacities for each molecule showed a linear relationship for the entire temperature range of interest, with an average decrease of 50 ± 5% from 298 to 150 K. Consequently, the heat capacity of solid azulene at 298 K was assumed to decrease by 50% between 298 and 150 K. The resulting linear relationship was integrated over this range. The correction to the sublimation enthalpy of azulene between 150 and 298 K is +3.92 kJ/mol, resulting in a sublimation enthalpy of 78.1 ± 2.2 kJ/mol at 150 K.

The heat of adsorption of azulene on Pt(111) at 150 K decreased to a relatively constant value of 92.7 kJ/mol between 0.12 and 0.17 ML, when the second layer was growing (with an average heat in this range that varied by ±3.4 kJ/mol among runs). Above 0.2 ML, the heat of adsorption reached a nearly constant value, which averaged 80.6 ± 1.6 kJ/mol, within error bars of the bulk sublimation enthalpy at 150 K of 78.1 ± 2.2 kJ/mol. The higher heat at coverages in the second layer (~0.1 to 0.2 ML) indicates that the Pt(111) surface is still close enough to interact with azulene, in spite of the presence of an intervening layer of adsorbed azulene.

5.3.2 Adsorption Energies

DFT calculations of adsorbed large organic molecules are often performed for only one, rather high coverage to reduce the unit cell size and thus the computational effort. This restriction ignores the coverage dependence of many properties, including the adsorption energy. For comprehensive comparison with the coverage-dependent SCAC data, we calculated six different adsorbate structures in a wide range of coverages.

The DFT adsorption energies for the lowest calculated coverage [(7 × 7) structure, coverage of 0.020 ML] are −389 kJ/mol for azulene and −345 kJ/mol for naphthalene. These values decrease to −308 and −258 kJ/mol at the highest coverage [(3 × 3) structure, 0.111 ML],

respectively. The adsorption energies for all calculated structures are compared to the experimental SCAC values in Figure 5-3. The SCAC data for naphthalene are taken from the literature[60].

For a meaningful comparison of the integral electronic adsorption energies from theory with the differential experimental energies, the second-order polynomials obtained by fitting the experimental data were integrated. For a coverage of 0.083 ML, harmonic zero-point vibrational energy (ZPVE) and harmonic thermodynamic corrections for the DFT-derived values were performed, yielding the adsorption enthalpy in addition to the electronic adsorption energy directly produced by DFT.

For azulene, the calculated and measured adsorption energies agree remarkably well and deviate by an average of only 8 kJ/mol over the coverage range. In contrast, the adsorption energy of naphthalene is overestimated by an average of 53 kJ/mol. An overestimation by theory is expected, since the D3 dispersion correction is known for this shortcoming[86,159,160]. In previous work, DFT-D3 overestimated the adsorption energies of azulene and naphthalene on Cu(111) by 28 and 45 kJ/mol, respectively[86]. Considering the finite temperature of the measurements, neglecting anharmonicities in the calculations may additionally contribute to this overestimation: the vertical potential of the molecule on the surface is strongly anharmonic, resulting in an increased adsorption height and decreased adsorption energy at elevated temperatures[160]. The literature SCAC data for naphthalene were measured at 300 K[60], whereas the SCAC data for azulene in this work were measured at 150 K. Therefore, the lowering effect of the elevated temperature on the adsorption energy should be stronger for naphthalene. It is, however, impossible to distinguish between these effects and the inherent limitations of DFT-D3.

The calculations correctly reproduce the higher adsorption energy of azulene and the general coverage dependences for both isomers. Considering their almost identical adsorption heights, it may be concluded that the latter (and the WF changes) are mainly determined by Pauli repulsion, whereas the extra adsorption energy of azulene is structurally mainly expressed in the larger deformations of the molecule and the surface. However, the theoretical adsorption energies of the two isomers differ by 37−50 kJ/mol over the whole coverage range, which is distinctly smaller than the experimental difference of 85−116 kJ/mol. The harmonic zero-point vibrational and thermodynamic corrections change the adsorption energy only slightly to larger values (ZPVE: 1−2 kJ/mol, thermodynamic corrections: 5−7 kJ/mol). As shown in the bottom part of Figure 5-3, previous theoretical studies without dispersion corrections strongly underestimated the adsorption energy of naphthalene on Pt(111)[84,85]. These deviations illustrate that dispersion corrections are also necessary in the case of chemisorption[160]. In our case, the dispersion attraction accounts for approximately one-third of the interaction energy.

5.4 Conclusions

The isomers azulene and naphthalene constitute a versatile molecular model system to study interfacial interactions of the topological pentagon−heptagon (5−7) defects in graphene. The experimental and theoretical analyses reveal that both molecules are chemisorbed on Pt(111) but azulene forms the stronger bond. Its differential adsorption energy, as measured by SCAC, is larger by 68 to 116 kJ/mol, depending on the coverage, and reaches 416 kJ/mol at zero coverage, compared to 300 kJ/mol for naphthalene. The stronger bond of azulene and the coverage dependencies of the adsorption energies are qualitatively correctly predicted by dispersion-corrected DFT calculations. DFT reveals rehybridization toward sp^3 and a partially localized σ-

character of the molecule−metal bond. The interfacial electron transfer occurs in both directions through donation and back-donation, resulting in the partial occupation (deoccupation) of orbitals that are unoccupied (occupied) in the free molecules, as shown by pEDA. Interpretation of the UP and NEXAFS spectra with an MO projection analysis supports the occupation/deoccupation mechanism of the surface chemical bond. It also reveals that the molecular orbitals of azulene and naphthalene respond differently to adsorption. This observation connects the topology-related differences in the electronic structure (especially the HOMO−LUMO gap) with the different bonds to the surface. Our analysis shows that the π-topology of an aromatic ring system substantially influences its interaction at a metal/organic interface in the regime of strong chemisorption. Topology-related effects are therefore relevant for various applications, including metal/organic interfaces in organic (opto)electronic devices or catalytic reactions of aromatic hydrocarbons on transition-metal surfaces.

5.5 Figures

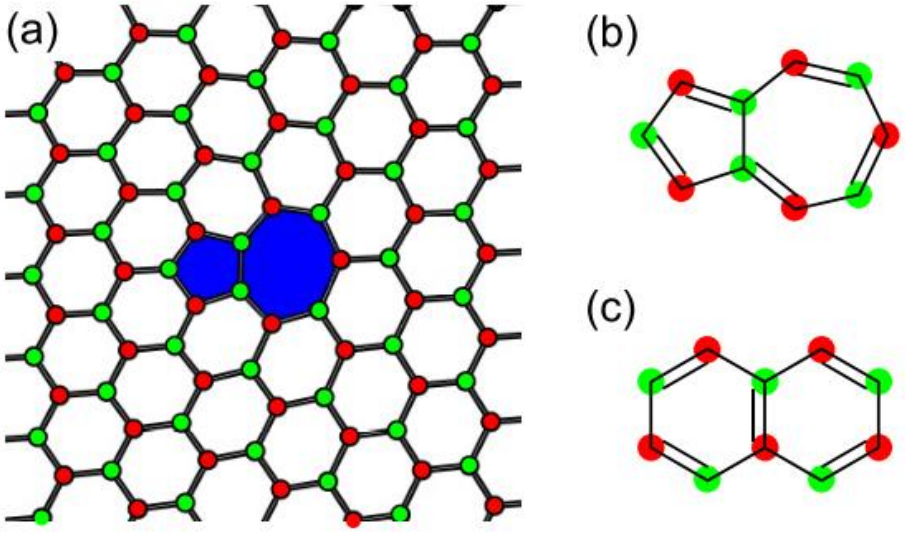

Figure 5-1. (a) Graphene sheet with an embedded pentagon−heptagon (5−7) defect (blue). Molecular structures of (b) azulene and (c) naphthalene. The different topologies of the two isomers are illustrated by the color schemes: naphthalene has an alternant topology (only alternating or differently colored C centers are connected), whereas azulene has a nonalternant topology (two atoms with the same color are connected). As shown in (a), the 5−7 defect locally interrupts the alternant topology of regular graphene.

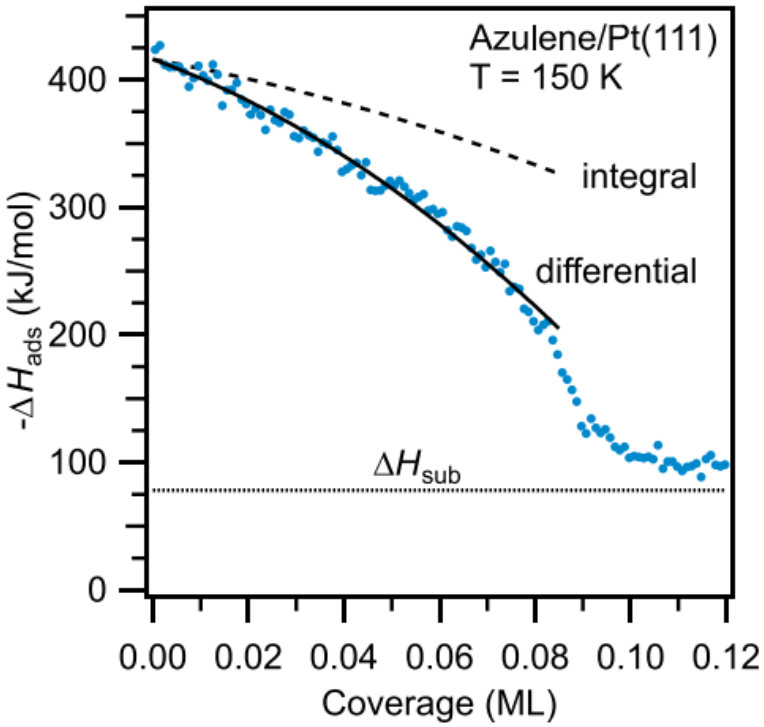

Figure 5-2. Heat of adsorption of azulene on Pt(111) at 150 K as a function of coverage. Blue dots, experimental data; solid black line, fit function of the differential heat; dashed black line, integrated fit function. The dotted line shows the sublimation enthalpy (ΔH_{sub} = 78.1 ± 2.2 kJ/mol) reported in the literature[156] adjusted for the temperature of 150 K.

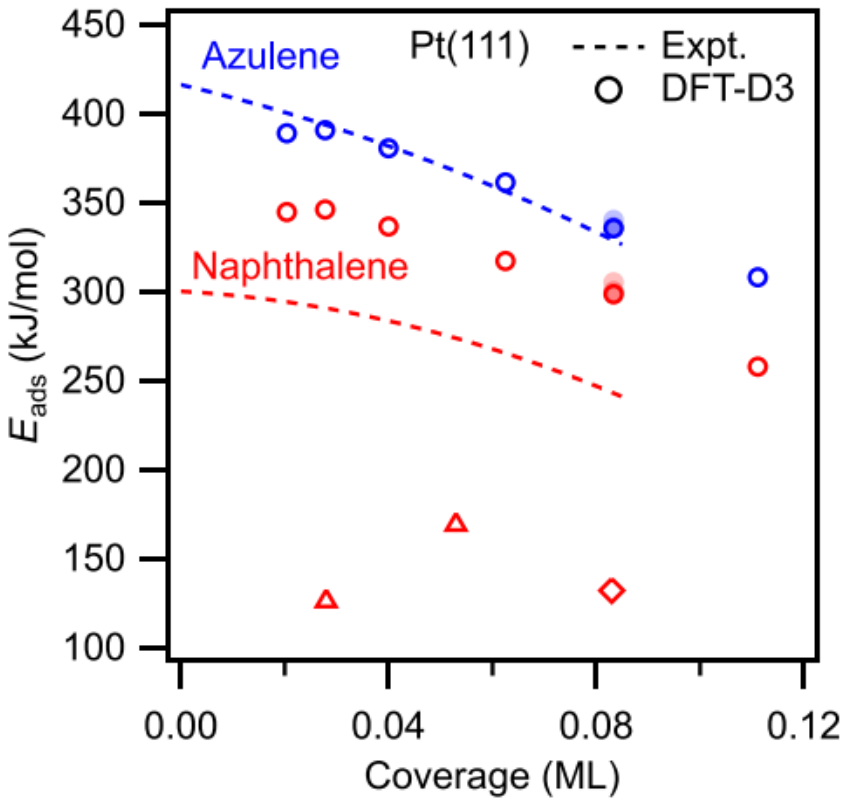

Figure 5-3. Integral adsorption energies for azulene (blue) and naphthalene (red) on Pt(111). Experiment (Expt., dashed lines): second-order polynomials for the measured integral heats of adsorption taken from Figure 5-2 (azulene) and the literature (naphthalene)[60]. Theory: adsorption energies for the six coverages calculated on the PBE-D3 level (open circles). Also included are previous DFT results for naphthalene (triangles[84] and diamonds[85]). The corrected DFT values for the coverage of 0.083 ML (harmonic zero-point vibrational energy, ZPVE and enthalpies) are plotted in progressively lighter colors (filled circles, overlapping).

Chapter 6 Energetics of Adsorbed Formate and Formic Acid on Cu(111) by Calorimetry

Chapter Abstract

The heats of adsorption of formic acid molecularly adsorbed on clean Cu(111) and dissociatively adsorbed onto oxygen-precovered Cu(111) were measured by single-crystal adsorption calorimetry. The dissociative adsorption of formic acid on oxygen-precovered Cu(111) produces adsorbed bidentate formate and gaseous water at 240 K. For this dissociative adsorption at 240 K, the differential heat of adsorption is initially 99.1 kJ/mol, decreasing approximately linearly to 80.4 kJ/mol by a coverage of ~0.20 ML. The integral (average) heat of adsorption at 240 K is well fit by (99.1 – 46.8θ) kJ/mol, giving an integral heat of 89.7 kJ/mol at a coverage of θ = 0.20 ML. From this, the heat of formation of adsorbed bidentate formate on Cu(111) and the bond enthalpy of bidentate formate to the Cu(111) surface were determined to be -465 kJ/mol and 335 kJ/mol, respectively. Corresponding values were estimated for monodentate formate on Cu(111), giving -437 kJ/mol for the enthalpy of formation and 307 kJ/mol for the bond enthalpy. We compare these results to reported DFT calculations and find that DFT systematically underestimated these bond enthalpies and enthalpies of formation on Cu(111). These values are also compared to previous calorimetric results for dissociative formic acid adsorption on Pt(111) and Ni(111), which shows that the bond enthalpies and enthalpies of formation of mono- and bidentate formate on Cu(111) are slightly greater than those on Ni(111) (by ~15 kJ/mol) and significantly greater than those on Pt(111) (by ~85 kJ/mol). This is (to our

knowledge) the first experimental measurement of the energy of *any* molecular fragment bonded to *any* Cu surface, making these results important benchmarks for validating the energy accuracy of computational models for a wide range of adsorbed species on Cu catalysts. For the molecular adsorption of formic acid on clean Cu(111) at 120 K, the differential heat of adsorption is initially 80.9 kJ/mol, which drops to ~70 kJ/mol by ~0.50 ML, before decreasing to a multilayer energy of 64.3 kJ/mol by a coverage of 1.75 ML. Using the heat of adsorption at 120 K up through bulk-like multilayer coverages, we estimate the adhesion energy for liquid formic acid to Cu(111) to be 0.271 J/m^2.

6.1 Introduction

Understanding the energetics of small molecules and molecular fragments on transition metal surfaces is crucial for advancing fundamental insights into catalysis, the development of new catalysts and catalytic processes, and improving the energy accuracy of methods like density functional theory (DFT) used for computational modeling of these systems. Here, we expand upon the previous work of the Campbell group that measured the energetics of irreversible adsorption for molecular fragments on Pt(111) and Ni(111) to now include adsorption on the Cu(111) surface[28,30,133,161,162,31,33,35,37–39,60,122]. In this paper, we use calorimetry under ultrahigh vacuum conditions to directly measure the heat of molecular adsorption of formic acid onto clean Cu(111), and the heat of dissociative adsorption of formic acid onto oxygen-precovered Cu(111). We compare and contrast these heats on Cu(111) with those measured for the same adsorbates on Pt(111) & Ni(111), and with DFT predictions of these heats on Cu(111).

Formic acid and adsorbed formate are considered important intermediates for many reactions on late transition metal catalysts. This includes well-established industrial reactions such as methanol synthesis, water-gas shift, and steam reforming of methane[88–91], as well as more emergent applications such as biomass reforming, fuel cell feeds, and a potential hydrogen carrier[92–96]. The surface interactions of organic molecules containing -COO^- or -COOH groups such as peptides, proteins, and amino acid residues are also important for a wide variety of applications ranging from medical implants[163,164] to the controlled synthesis of nanoparticles and nanostructures[165,166]. More recently, formate has emerged as an adsorbed intermediate of interest in thermal and electrocatalytic processes for the reduction of CO_2[97–99]. However specific mechanisms and reaction pathways within this context are still unclear and the subject of intense

study[92,93,95,96,100–102]. The results reported here provide important benchmarks to improve the energy accuracy of computational models that seek to elucidate these processes.

Formate is the simplest example of a carboxylate adsorbate, and can consequently act as a prototype for understanding the bonding energetics for more complex examples of this class of adsorbates. However, since the dissociative adsorption of formic acid is an irreversible adsorption process, traditional methods for studying the energetics of surface adsorbates, such as Temperature Programmed Desorption (TPD), cannot be used. To date, the heat of formation of adsorbed formate has only been measured for two surfaces, Pt(111)[30] and Ni(111)[35], both previously reported by this group. This work not only expands these results to the Cu(111) surface, but constitutes (to our knowledge) the first measured heat of formation for *any* molecular fragment on *any* Cu surface.

Copper is an important transition metal catalyst for a number of chemical applications where formate and more complex carboxylates are adsorbed intermediates, including water-gas shift, methanol synthesis, partial oxidation of methanol, and the conversion between esters and alcohols[88–91,167]. It has also garnered interest as the most promising monometallic catalyst for CO_2 reduction chemistry, particularly in electrocatalytic applications[98,103–105]. Formate is commonly seen in these reactions as an intermediate in either preferred or competing reaction pathways[97–99]. Additionally, Cu is predicted by DFT to show large differences in adsorbate bond energies in comparison to Ni and Pt. Thus in combination with previous studies from this group on Pt(111) and Ni(111), these measurements on Cu(111) provide a set of key experimental benchmarks on these three surfaces. As all three of these metals are widely used in industrial catalytic reactions, this suite of benchmarks can expand our fundamental understanding of observed differences in catalytic activity between them. The (111) surface is chosen for all three

metals as it is the most thermodynamically stable facet and thus is expected to dominate the surfaces of these metal catalysts, at least when particle size is large. Consequently, the (111) surface has been widely studied as a well-defined model for Cu, Ni, and Pt catalysts.

Here, we use calorimetry under ultra-high vacuum conditions to directly measure the heat of molecular adsorption of formic acid onto clean Cu(111), and the heat of dissociative adsorption of formic acid onto oxygen-precovered Cu(111). This allows for the extraction of the bond enthalpy and enthalpy of formation of adsorbed bidentate formate on Cu(111), along with estimates of the equivalent values for monodentate formate. These values not only serve as important benchmarks for computational models, but also clarify the energetics of important elementary reaction steps that occur in catalysis on Cu surfaces.

6.2 Experimental Methodology

The experiments were performed in an ultra-high vacuum (UHV) chamber (base pressure $<2 \times 10^{-10}$ mbar) designed for single-crystal adsorption calorimetry (SCAC). The chamber is also equipped with X-ray photoelectron spectroscopy (XPS), low-energy electron diffraction (LEED), Auger electron spectroscopy (AES), low-energy ion-scattering spectroscopy (LEIS), a quadrupole mass spectrometer (QMS), and a calibrated liquid-nitrogen-cooled quartz crystal microbalance (QCM), used to measure the absolute flux of the HCOOH molecular beam. The SCAC apparatus and experimental procedures for the molecular beam flux, sticking probability, and heat measurements have been described in depth previously[25,26,133].

To briefly summarize, the Cu(111) sample used was a 2 μm thick single-crystal foil provided by Bine Hansen at Aarhus University. The surface was cleaned by repeated cycles of Ar^+ ion sputtering and annealing until a well-ordered (111) LEED pattern was obtained. (Due to

the high reflectivity of Cu, the exact annealing temperature of the sample surface could not be determined using an optical pyrometer.) The oxygen-precovered surface was prepared by exposing the clean Cu(111) surface at 240 K to 30 Langmuir of O_2 gas, which we show below produces atomically-adsorbed oxygen at a coverage of ~0.10 ML O adatoms per Cu surface atom. The clean or O-precovered Cu(111) surface was exposed to a pulsed, collimated molecular beam of formic acid, and the heat of adsorption and sticking probability were recorded simultaneously. The sticking probabilities (both long-term (S_∞) and short-term (S_{102ms})) were measured with a QMS using the King and Wells method[121], and are as defined previously[26,133] to relate to the fraction of molecules in the gas pulse that stick to and remain on the surface until the start of the next pulse (S_∞), and those that stick long enough to contribute to the heat signal (S_{102ms}, which is measured only in the first 102 ms here). The heat of adsorption was measured by a pyroelectric ribbon pressed against the back of the Cu(111) crystal. The molecular beam was created by expanding approximately 4.0 mbar of formic acid through a glass capillary array held at 360 K and collimated through a series of orifices that are cooled with liquid nitrogen. The resulting molecular beam is then chopped into 102 ms pulses every 3 s.

Here, one monolayer of coverage is defined as the number of molecules of formic acid adsorbed to the surface per unit area, regardless of the product produced, normalized to the density of Cu atoms on the (111) surface (1.77×10^{19} atoms per m^2). A typical dose is 0.010 ML (~4.5×10^{12} molecules within the beam diameter of ~4 mm) per formic acid gas pulse.

Light pulses from a HeNe laser (632.8 nm) were used to calibrate the heat detector sensitivity, as described previously for studies on Pt(111)[28–30,33,60,122,133,161] and Ni(111)[35,37–39]. Since Cu(111) has a much higher reported optical reflectivity for this wavelength (0.973)[168] than Pt (0.76) and Ni (0.65)[169], the accuracy of the laser calibration of the heat signal is less reliable

than for Pt and Ni. (Any small relative difference between our samples' reflectivity and this literature value we assume for calibration leads to ~10-fold larger error in the heat adsorbed.) These SCAC experiments on Cu also had ~10-fold lower heat signal and poorer heat signal-to-noise ratio than was typical for experiments from this group on Pt and Ni. We think this may also be due to the much lower infrared optical emissivity (absorptivity) of Cu, which might make a large contribution to the heat transfer rate from the metal crystal to the heat detector.

6.3 Results

6.3.1 Sticking Probabilities

Recent experiments have shown that formic acid will not dissociatively adsorb on clean Cu(111) except to a small extent attributed to the step edge defect density[94,170]. This produces low coverages of adsorbed formate, which takes on the monodentate structure ($HCOO_{mono,ad}$) at low temperatures but converts to bidentate ($HCOO_{bi,ad}$) at 200 K and above[94,170]. Higher coverages of monodentate formate can be formed by extended HCOOH gas dosing (10 to 30 minutes) at 150-160 K[171]. Early reports of rapid dissociative adsorption of HCOOH on Cu(111)[172,173] may have been due to X-ray beam damage.

Dissociative adsorption of HCOOH does occur rapidly on oxygen-predosed Cu(111), resulting in the formation of adsorbed formate in the bidentate structure, $HCOO_{bi,ad}$, with coverages up to 0.33 formate molecules per Cu surface atom[174]. That reaction was characterized at 330 K by the net stoichiometry[174]:

$$2\ HCOOH_g + O_{ad} \rightarrow 2\ HCOO_{bi,ad} + H_2O_g \quad . \qquad (6\text{-}1)$$

However, this probably involves the step:

$$HCOOH_g + O_{ad} \rightarrow HCOO_{bi,ad} + OH_{ad} \quad , \qquad (6\text{-}2)$$

which is known to occur on Cu(110) and Cu(111)[175,176], and then the two hydroxyls thus produced convert to water and O_{ad} via:

$$2\ OH_{ad} \rightarrow H_2O_g\ +\ O_{ad}\ . \qquad (6\text{-}3)$$

Reaction 6-3 is known to occur on Cu(111) already at 160 K during TPD after producing OH_{ad} by dosing methanol to a surface at 110 K with pre-adsorbed O_{ad} [177]. Interestingly, Reaction 6-3 only occurs at much higher temperatures on the other widely-studied Cu faces: 220 K on Cu(100)[178] and 290 K on Cu(110)[179,180]. We note that Reaction 6-2 above may occur in two steps, whereby the less stable monodentate formate forms first but converts to bidentate formate (as noted in literature cited farther above).

Given these results from the literature, one expects that when we dose HCOOH to O pre-dosed Cu(111) at 240 K, we get the same net reaction as Reaction 6-1.

Figure 6-1 shows the average long-term (S_∞) and short-term (S_{102ms}) sticking probabilities versus coverage for formic acid adsorption on O-precovered Cu(111) at 240 K. The HCOOH-derived coverages reported throughout this paper represent the amount of formic acid permanently adsorbed, regardless of the product produced (i.e., formate or molecularly adsorbed HCOOH). We will use "O-precovered Cu(111)" throughout to refer to a Cu(111) surface with ~0.10 ML of oxygen adatoms. The long-term sticking probability (S_∞) is the probability that a gas molecule strikes the sample surface, sticks, and remains until the next gas pulse starts 3 s later. This is used to calculate the adsorbate coverage at the start of the next gas pulse. The short-term sticking probability (S_{102ms}) is the probability that a gas molecule strikes the sample surface, sticks, and remains at least through the time window of the heat measurement (i.e., the first 102

ms). This is used to calculate the number of moles of gas-phase reactants that contribute to the measured heat signal for that gas pulse, and thus the heat of adsorption per mole adsorbed.

At 240 K, both the long-term and short-term sticking probabilities start high at ~0.90 initially and increase quickly with coverage, reaching near unity within 0.03 ML. The sticking probabilities then remain at unity (within the noise) through a coverage of ~0.15 ML. Past this coverage, the long-term sticking probability drops off rapidly, reaching zero by 0.20 ML, while the short-term sticking probability remains high (>0.90). After this coverage, formic acid continues to transiently adsorb on the saturated adlayer with a high probability, as evidenced by the high short-term sticking probability, but desorbs again completely (but slowly) before the next pulse starts 3 s later. This suggests that the O adatoms are fully reacted in the dissociative adsorption reaction, and no further dissociative adsorption can occur. We note that the temperature here is above that necessary for multilayer adsorption (~150 K[170]), so no molecular adsorption beyond the first layer is expected.

The inset in Figure 6-1 shows the HCOOH dosage at which its long-term sticking probability at 240 K drops to 0.50 as a function of the amount of pre-exposure of the clean Cu(111) surface at 240 K to O_2 gas. As seen, this HCOOH dosage increases steeply with O_2 pre-dose, from nearly zero with no pre-dose of O_2, and quickly saturates at ~0.18 ML after ~20 L of O_2. Similarly, the HCOOH dosage at which its S_∞ dropped below 0.1 saturated at ~0.20 ML after ~20 L of pre-dosed O_2 (not shown). Assuming a 2:1 stoichiometric ratio in Reaction 6-1 proposed above based on prior literature ($2\ HCOOH_g + O_{ad} \rightarrow 2\ HCOO_{bi,ad} + H_2O_g$), we take this to indicate that the 30 L O_2 pre-exposure at 240 K used in Figure 6-1, which gives a saturation formate coverage of 0.20 ML, corresponds to about 0.10 ML of O adatoms. This is about 10-fold smaller O_2 dose than was reported to produce this same coverage on Cu(111) at 296 K[181]. The

~4-fold smaller apparent saturation coverage of O_{ad} seen here than reported at 296 to 600 K (~0.44 ML[181]) may indicate that defects such as step edges may aid in O_2 dissociation, especially at the lower temperature used here.

Based on the prior literature summarized above, we concluded that when we dose HCOOH to O-predosed Cu(111) at 240 K, we get the same net reaction as Reaction 6-1. This also means that gaseous H_2O should have evolved simultaneously with the dissociation of HCOOH. We attempted to detect this H_2O_g by averaging the QMS signal at m/e = 18 for the pulses below 0.2 ML dose, but were unable to see signal above the noise due to H_2O evolution. However, given the high background signal of water in the chamber (and associated large noise at m/e = 18), the expected water peak intensity (~1/2 the QMS signal for formic acid at zero-sticking probability, according to the stoichiometry of Reaction 6-1) would not have been visible above the noise in the background signal. Thus, we still believe Reaction 6-1 dominates at 240 K.

At 120 K on clean Cu(111), where formic acid adsorbs molecularly, the short-term and long-term sticking probabilities are both unity (within the pulse-to-pulse noise similar to that in Figure 6-1) at all coverages, so they are not shown here. As this temperature is cold enough to form multilayers of formic acid on the Cu(111) surface, the sticking probability was found to remain at unity through at least five layers of coverage.

6.3.2 Heats of Adsorption

In this paper, the term “heat of adsorption” is defined at the negative of the standard molar enthalpy change for the adsorption reaction, with the gas and the sample surface being at the sample temperature. As explained in detail previously, this requires a small enthalpy correction on the measured heat since the gas molecule’s enthalpy in the molecular beam is

slightly higher than a Boltzmann distribution at the Cu(111) temperature due to the actual experimental molecular beam conditions[133]. The differential heat of adsorption is the heat released per mole when a small increment of adsorbate is added to the surface at nearly fixed coverage, as occurs in one of our molecular beam pulses during SCAC. The integral heat of adsorption is the integral of the differential heat versus coverage from zero up to the coverage of interest, divided by that coverage, and is thus the average heat for that coverage range.

Figure 6-2 shows the differential heats of adsorption for formic acid on clean Cu(111) at 120 K (blue) and on O-precovered Cu(111) at 240 K (red) (after this small correction to the raw heats noted above) as a function of adsorbate coverage. The integral heat of adsorption at 240 K is also shown in black from the low coverage limit. These are averages of three and nine runs at 120 K and 240 K, respectively. For both the 120 K and 240 K data, the first two data points are significantly higher than subsequent points and are attributed to adsorption on defect sites on the surface, likely at step edges. These two points are excluded from integral heat and initial heat determinations so that these values correspond to adsorption on terraces and are not inclusive of these defect sites that bind more strongly.

Previous results from literature show that formic acid molecularly adsorbs on clean Cu(111) below ~250 K, and multilayers will adsorb to the surface below 150 K[170]. Thus, calorimetric measurements at 120 K on clean Cu(111) correspond to molecular adsorption of formic acid in the first layer, with the formation of multilayers at higher coverages.

At 120 K, the initial heat of adsorption is 80.9 kJ/mol (excluding the first two points, which are higher, and may be due to adsorption at defects, likely step edges). The heat decreases approximately linearly with coverage until reaching ~70 kJ/mol by 0.50 ML, where the first adlayer of formic acid appears to be completed. Beyond this point, the heat of adsorption stays

constant at ~68.5 kJ/mol through ~1.5 ML, before decreasing to the multilayer energy value of 64.3 ± 2.9 kJ/mol. (This is the run-to-run average and standard deviation of the multilayer heats of the three runs.) Each run's multilayer heat is the pulse-to-pulse average heat for coverages above 1.75 ML. The heat of sublimation of bulk formic acid was estimated to be 61.9 kJ/mol at 120 K, using literature values for the enthalpies of phase transitions[134] along with heat capacities of solid, liquid, and gaseous formic acid[136], as a heat of sublimation at 120 K was not available in literature. The bulk heat of sublimation at 120 K was also estimated using the same heat capacities but instead starting from a reported bulk heat of sublimation at 200 K (60.5 kJ/mol[182]), which gives a very similar value of 61.3 kJ/mol. The average of these two bulk literature values (61.3 and 61.9 kJ/mol) falls within the error bars of the multilayer heat measured here (61.4-67.2 kJ/mol). This close agreement provides an estimate of the absolute accuracy of the results in Figure 6-2.

At 240 K, the initial heat of adsorption on the O-precovered Cu(111) surface is 99.1 kJ/mol (again excluding the first two points, which are higher, and may be due to adsorption at defects, likely step edges). The heat decreases approximately linearly with coverage until reaching 80.4 kJ/mol by a coverage of ~0.20 ML. Past this point, the long-term sticking probability has dropped to zero, indicating that surface O adatoms have been fully consumed by the dissociation reaction and the surface adlayer is saturated. Any additional formic acid molecules that impinge on the surface adsorb transiently (as indicated by the high short-term sticking probability), but fully desorb before the next pulse begins 3 s later. The integral heat of adsorption at 240 K is shown in black versus coverage up to saturation, and is well fit by (99.1-46.8θ) kJ/mol, where θ is coverage in ML, with an integral heat of 89.7 kJ/mol at saturation (0.20 ML).

Above saturation on O-precovered Cu(111) at 240 K, the transiently adsorbed HCOOH has a constant heat of adsorption at saturation ($\Delta H_{ad,sat}$) of 72.5 ± 3.3 kJ/mol. By averaging the mass spectrometry pulse line-shapes (signal versus time) after saturation and fitting an exponential decay function to the post-pulse signal decay, we obtained a decay constant, τ, which is equal to the reciprocal of the first-order desorption rate constant, k_{des}, given by[183]:

$$\frac{1}{\tau} = k_{des} = \nu_{des} \cdot exp\left[\frac{-E_{des}}{RT}\right] \quad (6\text{-}4)$$

where ν_{des} is the prefactor for desorption, E_{des} is the activation energy of desorption, R is the gas constant, and T is the temperature. Using the values of τ = 0.85 s and k_{des} = 0.173 s^{-1} determined from this exponential decay fit, along with E_{des} = 71.5 kJ/mol determined from the measured heat after saturation ($E_{des} = \Delta H_{ad,sat} - 1/2RT$ [155]), a prefactor for desorption can be calculated. In that way, we determined an experimental prefactor for HCOOH desorption of ν_{des} = 4.3 x 10^{15} s^{-1}. This can be compared to the prefactor for desorption estimated by the method of Campbell & Sellers[183], which gives ν_{des} = 2.4 x 10^{15} s^{-1} for molecularly adsorbed HCOOH at 240 K. This good agreement indicates that the transiently adsorbed HCOOH is molecularly adsorbed and not, for example, transiently dissociated and then recombined.

6.4 Discussion

6.4.1 Energetics of Adsorbed Formate on Cu(111) at 240 K

As discussed above, our calorimetric measurements on the O-precovered Cu(111) surface at 240 K represent the heats of dissociative formic acid adsorption onto Cu(111), via Reaction 6-1 above: $2\ HCOOH_g + O_{ad} \rightarrow 2\ HCOO_{bi,ad} + H_2O_g$. By using available literature values for the heats of formation of various gas-phase and adsorbed molecules and the experimentally measured heat at 240 K, we can extract the bond enthalpy of bidentate formate to Cu(111)

($HCOO_{bi,ad}$=Cu(111)) and the enthalpy of formation of bidentate formate on the Cu(111) surface ($\Delta H_f(HCOO_{bi,ad})$). To do so, we construct the thermodynamic cycles shown in Figure 6-3 & Figure 6-4. Note that all positive heats of adsorption in Figure 6-2 represent exothermic processes, while here they have been converted to negative enthalpies of reaction for use in the thermodynamic cycles.

The cycle in Figure 6-3 begins on the left-hand side, starting with gas-phase formate and a surface-bound oxygen atom (but with only ½ mole of O_{ad}, for ½ of the stoichiometry of Reaction 6-1, which then corresponds to a single formate adsorbate). The bottom pathway represents our measurement at 240 K, and is quantified by the integral heat of adsorption at 0.20 ML. This must be energetically equivalent to the parallel pathway; therefore, the sum of the steps in the top pathway must equal -90. kJ/mol. The first step in the top pathway is to dissociate gas-phase formic acid into a gas-phase hydrogen atom and a gas-phase formate radical. The enthalpy of reaction for this step (+468 kJ/mol) is calculated using literature values for the enthalpies of formation for each of the three gas-phase species from elements in their standard states at 298 K[134].

In the second step of the top pathway the oxygen adatom is desorbed to form gaseous oxygen. In the absence of a reported value for the enthalpy of formation of adsorbed O on Cu(111), or the reverse of this step, the enthalpy of reaction (+116 kJ/mol) is estimated from reported literature values for the enthalpy of dissociative adsorption of O_2 on polycrystalline Cu of 465 kJ per mole O_2 [184,185]. Reported DFT calculations (summarized in Table 6-3 below) for the adsorption energy of O_{ad} on different Cu faces showed that O_{ad} is 21 to 36 kJ/mol less stable on Cu(111) than on the (110) and (100) faces[186]. This suggests that this calorimetric heat for ½ O_{ad} of 116 kJ/mol in Figure 6-3 may be too large for Cu(111) by 10 to 18 kJ/mol. In this second

step, the gas-phase hydrogen and formate radical species were left unchanged. The third step in the top pathway is to combine the gaseous oxygen and hydrogen species to form gaseous water. The enthalpy of reaction for this step (-339 kJ/ml) was calculated using literature values for the enthalpies of formation for each of the three gas-phase species from elements in their standard states at 298 K[134].

Finally, this leaves the top right step as the only unsolved value. This step represents the enthalpy to form bidentate formate from the gas-phase formate radical, which provides an estimate of the total bond enthalpy of bidentate formate to Cu(111), from both its O-Cu bonds. The extracted $HCOO_{bi,ad}$=Cu(111) bond enthalpy is 335 kJ/mol. Given that this value is very close to that of the bond enthalpy of bidentate formate to Ni(111) (320 kJ/mol[35]), we assume the same difference in bond enthalpies between mono- and bidentate formate on Cu(111) as previously measured on Ni(111) (28 kJ/mol[35,36]) in order to estimate the bond enthalpy of monodentate formate to Cu(111). This estimated bond enthalpy of monodentate formate to Cu(111), or $HCOO_{mono,ad}$-Cu(111), is thus 335 - 28 = 307 kJ/mol. This assumed difference between mono- and bidentate formate is also close to that measured on Pt(111) (33 kJ/mol[30,36]).

Figure 6-4 shows how this extracted $HCOO_{bi,ad}$=Cu(111) bond enthalpy can be used in another thermodynamic cycle to extract the enthalpy of formation of bidentate formate on Cu(111). In this case the cycle starts on the left-hand side with the elements in their standard states. The top pathway uses first the literature value for the enthalpy of formation of gas-phase formate[187], followed by the extracted bond enthalpy of bidentate formate from Figure 6-3. This results in the formation of surface-bound bidentate formate. The bottom pathway then represents the enthalpy of formation for bidentate formate on Cu(111), and again must be energetically equivalent to the parallel pathway. The resulting extracted value for the enthalpy of formation of

bidentate formate, or $\Delta H_f(HCOO_{bi,ad})$, on Cu(111) is -465 kJ/mol. Using the same method as discussed above, the estimated corresponding enthalpy of formation for monodentate formate, or $\Delta H_f(HCOO_{mono,ad})$, on Cu(111) is -465 + 28 = -437 kJ/mol.

6.4.2 Comparison to DFT

The bond energies of bidentate and monodentate formate to Cu(111) measured in this work are compared to theoretical values obtained by DFT in Table 6-1. DFT calculations report integral bond energies of adsorbates at specific coverages. Bond enthalpies were converted to bond energies by subtracting *RT* (2 kJ/mol at 240 K). The bond enthalpies at 0.20 ML were calculated from the thermodynamic cycle in Figure 6-3. In order to match the reported coverage of most of the DFT values, equivalent values at 0.11 ML were calculated in an identical manner to that at 0.20 ML, but using the integral heat value at 240 K and 0.11 ML of 94 kJ/mol.

As can be seen, all of the reported DFT calculations significantly underestimate the measured bond energies of bidentate and monodentate formate to the Cu(111) surface. On average, the DFT values are ~80 kJ/mol lower than the experimentally determined bond energy of bidentate formate, and ~95 kJ/mol lower than that for monodentate formate. While larger in magnitude for Cu(111), this underestimation of the formate bond energy by DFT is also seen when comparing the experimental and theoretical values for Ni(111). For example, prior DFT calculations had underestimated the bond energy of bidentate formate to Ni(111) by 26 to 58 kJ/mol compared to calorimetry[35]. Both of these margins of error are supported by the fact that it is well known that DFT has substantial errors in energy accuracy[21]. Since prior to this present work, there had not been experimentally determined bond energies reported for *any* molecular fragment on *any* Cu surface, this work provides an important benchmark for comparison to computational studies of small molecular fragments on Cu(111). However future experimental

results beyond the formate/Cu(111) system will be important for extending these benchmarks to Cu systems more widely.

6.4.3 Comparisons to Pt(111) & Ni(111)

Previous calorimetric measurements by this group studied the adsorption of formic acid on Pt(111) & Ni(111), allowing for a direct comparison between the three metal surfaces[30,35]. The values of the bond enthalpies and enthalpies of formation for both mono- and bidentate formate to Pt(111), Ni(111), & Cu(111) are summarized in Table 6-2. When possible, coverages as close to the saturation coverage of 0.20 ML in this work have been reported, but that is not available for all values.

As can be seen, the experimentally determined values for Cu(111) are ~85 kJ/mol stronger than the equivalent values for Pt(111), and ~15 kJ/mol stronger than those for Ni(111). The reported bidentate formate bond enthalpies are 254, 320, and 335 kJ/mol on Pt(111), Ni(111), and Cu(111), respectively. The reported enthalpies of formation of bidentate formate are -381, -449, and -465 kJ/mol on Pt(111), Ni(111), and Cu(111), respectively.

It is interesting to compare this resulting trend of Pt < Ni < Cu to DFT results on all three systems. The experimental results reported here reverse the order of Ni & Cu predicted by DFT, where bidentate formate bond energies are predicted to be ~20 kJ/mol stronger on Ni(111)[35,102], when these results show them to be ~15 kJ/mol stronger on Cu(111). DFT does accurately predict that the bond energy to Pt(111) is much less than that of both Ni(111) & Cu(111)[102]. Also, DFT systematically underestimates the bond energy of formate to all three systems, by a margin of ~30, ~40, & ~85 kJ/mol on Pt(111), Ni(111), & Cu(111), respectively. It is well known that DFT has substantial errors in energy accuracy, and all of these margins of error in comparison to experimental results are comparable to margins of error reported previously[21].

Again, this work on Cu(111) provides an important benchmark to improve computational accuracy as the first bond energy reported for *any* molecular fragment on *any* Cu surface.

These calorimetric bond energies for monodentate formate to Pt(111) and Ni(111) are well fitted based on a model previously developed by Carey and Campbell that is based on Pauling's equation and uses only known parameters (gas-phase ligand-hydrogen bond enthalpies, bond enthalpies of adsorbed H atoms to the surface, electronegativities of the elements, and group electronegativities)[36]. That model was also used to predict equivalent values on surfaces for which experimental measurements had not yet been reported, including Cu(111). The predicted bond enthalpy of monodentate formate to Cu(111) was 228 kJ/mol[36], versus the estimated value of 307 kJ/mol reported here. In comparison to the equivalent experimental value of 292 kJ/mol on Ni(111), this trend also predicted the opposite order of bond enthalpies on Ni versus Cu than is seen in this work.

Further experimental measurements of molecular fragments on Cu(111) will be important to validate this observed difference between the experimental values measured here and those predicted by DFT or the electronegativity-based model of Carey & Campbell. At this point the basis for this difference is unclear, and the study of additional systems on Cu can further elucidate underlying mechanisms and energetics driving this difference.

6.4.4 Adhesion Energy of Liquid Formic acid on Cu(111)

Solvent/metal adhesion energies are crucial to understanding solvent effects on adsorption energies, which is increasingly critical as catalytic and electrocatalytic reactions occurring at solid surfaces in liquid solvents become more important. The determination of the adhesion energy for liquid formic acid on Cu(111) can provide valuable insight into the energetics of this liquid-solid interface. However, there is currently no way to directly measure

the adhesion energy of a liquid solvent to a clean metal surface. To estimate this adhesion energy, we will employ a recently developed method from this group that allows for an estimate of the adhesion energy from experimentally determined differential heat of adsorption data like that in Figure 6-2[44,143]. See refs. [44,122,143] for an in-depth derivation and discussion of this model.

This model results in the following equation for the determination of adhesion energy from calorimetric data:

$$E_{adh,S(liq)/M(s)} = \frac{\left[Q_{adsorption} - n \cdot \Delta H_{vap,S}\right]}{A} + 2\gamma_{S(liq)} \quad (6\text{-}5)$$

where $E_{adh,S(liq)/M(s)}$ is the adhesion energy of the liquid solvent (formic acid) to the solid metal surface (Cu(111)), $\gamma_{S(liq)}$ is the surface energy per unit area of bulk, liquid formic acid, and the term $[Q_{adsorption} - n \cdot \Delta H_{vap,S}]/A$ is equal to the numerically integrated area from zero coverage up to a (bulklike) multilayer coverage (with n moles adsorbed per area A) of the heat versus coverage curve ($Q_{adsorption}$) minus n/A times the molar heat of vaporization of the liquid solvent ($\Delta H_{vap,S}$). Ideally, these values would all be measured at room temperature to provide the adhesion energy at room temperature. Since $Q_{adsorption}$ can only be measured on a clean metal surface in ultrahigh vacuum, which is only possible for formic acid at temperatures where the solvent grows as solid films rather than liquid films, the assumption was made that the term $[Q_{adsorption} - n \cdot \Delta H_{vap,S}]/A$ at room temperature is approximately equal to the analogous quantity at experimental temperatures where the solvent is a solid, or $[Q_{adsorption} - n \cdot \Delta H_{sub,S}]/A$, where $\Delta H_{sub,S}$ is the heat of sublimation of bulk formic acid.

Using this method and the reported surface energy of bulk, liquid formic acid of $\gamma_{S(liq)}$ = 0.0377 J/m^2 [44,142], we calculate the adhesion energy of liquid formic acid to the Cu(111) surface at 120 K to be E_{adh} = 0.271 J/m^2. Comparatively, this value is slightly less than the adhesion energy of formic acid to Ni(111) (0.279 J/m^2), but greater than that to Pt(111) (0.162 J/m^2)[44].

Understanding this adhesion energy, and particularly how it compares to other common solvents, could enable the intelligent selection among these solvents to tune reaction environments to have more desirable energetics for surface adsorption or desorption for catalytic reactants and intermediates. Unfortunately, there is currently no other reported solvent adhesion energies to the Cu(111) surface for comparison. However, these values are reported for multiple solvents on Pt(111) & Ni(111) and follow the trend of methanol < formic acid < water < benzene ≈ phenol[44]. This indicates that solvents with higher heats of adsorption per unit area in the first adsorbed layer have higher adhesion energies to a given metal surface. We note that these adhesion energies were all estimated using the same assumption of a negligible difference in heat capacities (including the heat of fusion) between the first and subsequent layers, and the errors associated with this assumption are possibly large (~25%). However, all of these errors are likely qualitatively similar, so these trends in E_{adh} values will remain. The close alignment of the adhesion energy of liquid formic acid to Cu(111) with the equivalent values to Pt(111) & Ni(111) suggests that these energetic trends will extend to the Cu(111) surface as well. However further experimentally determined solvent/metal adhesion energy values on Cu(111), along with computational approaches, will provide valuable comparison to support or refute the extension of these trends to Cu(111).

6.4.5 Formic Acid Multilayer Structure on Cu(111)

The multilayer heat of adsorption obtained in this work on Cu(111) (64.3 ± 2.9 kJ/mol) is in close agreement with the estimated range for the heat of sublimation of bulk formic acid of 61.3-61.9 kJ/mol at 120 K, estimated from literature values as noted above. However, this is different than those heats previously reported by this group for multilayer adsorption of formic acid on Pt(111) and Ni(111) (49.9 and 52.8 kJ/mol, respectively)[30,35]. Previous literature results

show that below 143 K, adsorption of formic acid on Pt(111) results in the formation of an amorphous multilayer rather than the more stable crystalline (also referred to as polymeric) phase[188,189]. Therefore, Silbaugh *et al.* attribute the observed multilayer heat of 49.9 kJ/mol measured at 100 K to amorphous multilayer adsorption on Pt(111)[30]. However, STM studies on Cu(111) have shown the presence of the more stable polymeric multilayer phase down to 85 K[94,170]. This polymeric phase on Cu(111) is composed of hydrogen-bonded chains that align in a β configuration on the surface (roughly a zig-zag structure) that minimizes repulsive forces, and is consequently more energetically favorable than amorphous adsorption at lower temperatures. Therefore, the present results measured at 120 K correspond to polymeric multilayer adsorption on Cu(111).

6.4.6 Stability of OH_{ad} & energetics of H_2O desorption on Cu(111), Cu(100), & Cu(110)

In analyzing the heat measurements above when making bidentate formate, we used the fact that the desorption temperature for H_2O_g from $2\ OH_{ad} \rightarrow H_2O_g + O_{ad}$ was reported in a methanol study on Cu(111)[177] to be 160 K, so that this process was fast at the measurement temperature of 240 K. However, this temperature of 160 K is much lower than that known for this same reaction on Cu(110) (290 K[179,180]). To our knowledge, such a large percentage change in desorption temperatures between low-index faces of the same metal has not been reported for any reaction. As this value of 160 K for Cu(111) was only reported by one group, we wanted to verify that it is reasonable. To do this, we next compare this experimental difference to predicted results extracted from adsorption energies for O_{ad}, OH_{ad}, & H_2O_{ad} on Cu(111), Cu(100), & Cu(110) calculated by DFT[186]. The adsorption energies used for these calculations, along with

resulting enthalpies of reaction and predicted desorption temperatures are summarized in Table 6-3.

The listed adsorption energies were first used to calculate the enthalpy of reaction for Reaction 6-3 (the desorption of gaseous water from two adsorbed hydroxyls). This resulting reaction enthalpy was converted to a desorption energy, E_{des}, by subtracting 1/2 *RT*. We made the assumption that the reaction enthalpy was equal to the activation energy for desorption (after converting from enthalpy to energy) based on computational results in literature that predict that the energetic barrier for desorption of molecularly adsorbed water is far larger than the energetic barrier for the reaction of two surface-bound hydroxyls to form adsorbed water plus O_{ad} on Cu(111)[89]. A prefactor for desorption of $\nu_{des} = 5 \times 10^{14}$ s^{-1} was estimated using the method of Campbell & Sellers[183]. Together, these E_{des} and ν_{des} values can be used to estimate a temperature for the desorption of H_2O via the reaction $2\ OH_{ad} \rightarrow H_2O_g + O_{ad}$ from each of the three surfaces, using the first-order Readhead equation[190]:

$$E_{des} = RT_m \left[\ln\left(\frac{\nu_{des} T_m}{\beta}\right) - \ln\left(\frac{-E_{des}}{RT_m}\right) \right] \quad (6\text{-}6)$$

where *R* is the gas constant, T_m is temperature corresponding to the maximum of the desorption peak in TPD, and β is the heating rate. Using an assumed β = 5 K/s, the resulting estimated T_m values for Cu(111), Cu(100), & Cu(110) are 244, 286, and 407 K, respectively. In comparison, the values obtained in the TPD study of methanol by Pöllmann *et al.* are 160, 220, & 290 K, respectively[177]. As seen, the extremely wide range of the temperatures of desorption is reflected in the predicted temperatures, but the accuracy of the values are not well aligned with the experimental results. However, if we scale the DFT-derived reaction enthalpies by 0.70, equivalent to assuming an over-estimation of the reaction enthalpy of ~50% by DFT, we obtain

desorption temperatures of 173, 202, and 287 K for Cu(111), Cu(100), & Cu(110). These values are now in very close agreement to the results of Pöllmann *et al.*, and provide a verification of both the experimentally determined desorption temperatures and the extreme dependence of this temperature on the crystal face of Cu.

6.5 Conclusions

The energetics of the molecular and dissociative adsorption of formic acid on Cu(111) were measured by SCAC. The enthalpy of formation and bond enthalpy of bidentate formate to Cu(111) are -465 kJ/mol and 335 kJ/mol, respectively, at 240 K and 0.20 ML. Corresponding enthalpies are estimated for monodentate formate on Cu(111), which give an enthalpy of formation of -437 kJ/mol and a bond enthalpy of 307 kJ/mol. A comparison to DFT calculations in the literature shows that DFT systematically underestimates the bond enthalpies and enthalpies of formation of mono- and bidentate formate to Cu(111). In comparison to experimental measurements on Pt(111) and Ni(111), these enthalpy values indicate that formate binds ~15 kJ/mol more strongly to Cu(111) than to Ni(111), and ~85 kJ/mol more strongly than to Pt(111).

At 240 K, the integral heat of the dissociative adsorption of formic acid on oxygen-precovered Cu(111) is well fit by (99.1 – 46.8θ) kJ/mol, which gives an integral (average) heat of 89.7 kJ/mol at 0.20 ML. The initial differential heat of adsorption is 99.1, which decreases linearly to 80.4 kJ/mol by 0.20 ML. At 120 K, the molecular adsorption of formic acid on clean Cu(111) has an initial differential heat of adsorption of 80.9 kJ/mol, which decreases to ~70 kJ/mol by 0.50 ML. Past that coverage, the heat remains at ~70 kJ/mol through 1.5 ML, after which it drops to a multilayer energy of 64.3 kJ/mol by 1.75 ML. Using the 120 K heat of

adsorption curve measured out to multilayer coverages, we estimate the adhesion energy for liquid formic acid to Cu(111) to be 0.271 J/m^2.

These results constitute important benchmarks for DFT calculations and efforts to improve the energy accuracy of computational models, as they are (to our knowledge) the first experimental measurements of the energy of *any* molecular fragment on *any* Cu surface. As formate is the simplest example of a carboxylate adsorbate, these results are applicable not only for systems with formate, but as well as other carboxylates and, more broadly, other oxygenates on Cu surfaces. These results further our understanding of fundamental energetic differences on catalyst surfaces, and can help explain differences in catalytic activity between late transition metal catalysts and guide the development of new catalysts and catalytic pathways.

6.6 Figures

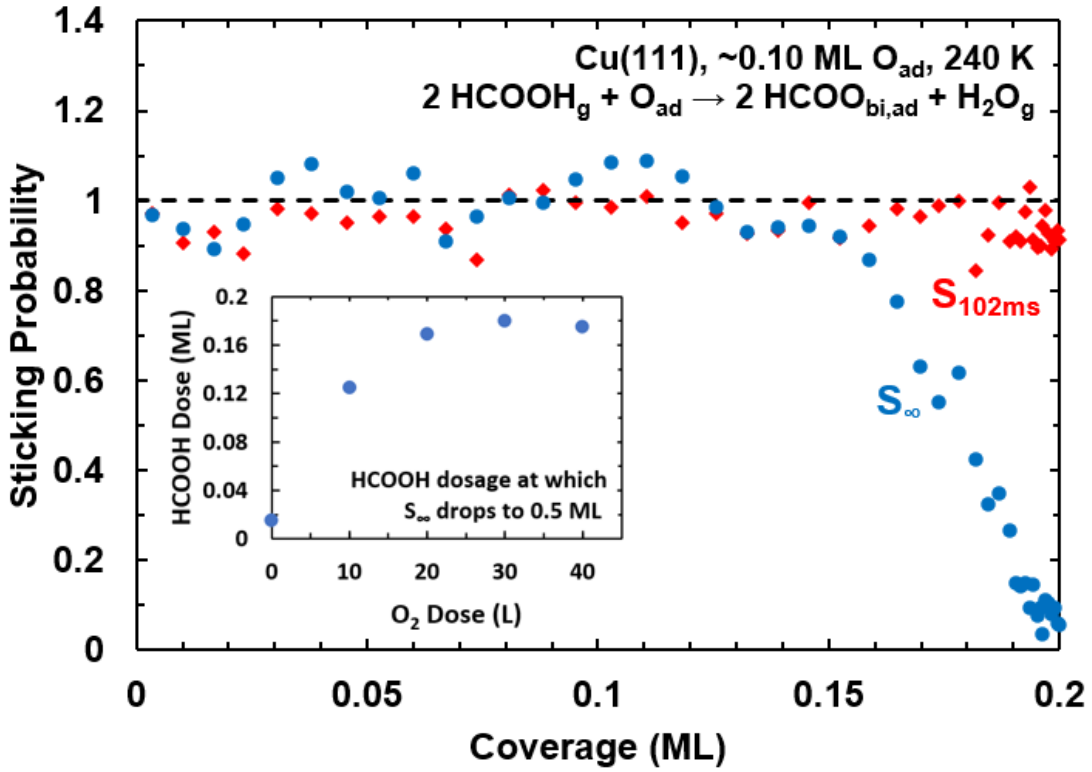

Figure 6-1. Average short-term (red diamonds, S_{102ms}) and long-term (blue circles, S_∞) sticking probabilities of formic acid dissociatively adsorbing on O-precovered Cu(111) at 240 K as a function of the HCOOH-derived adsorbate coverage. A coverage of 1 ML is defined as one adsorbate per Cu(111) surface atom or 1.77×10^{19} $HCOO_{bi,ad}$ adsorbates per m^2. Inset: The HCOOH dosage at which S_∞ at 240 K drops to 0.50 versus the pre-exposure of O_2 gas to the clean Cu(111) surface at 240 K. (1 Langmuir = 10^{-6} torr sec.)

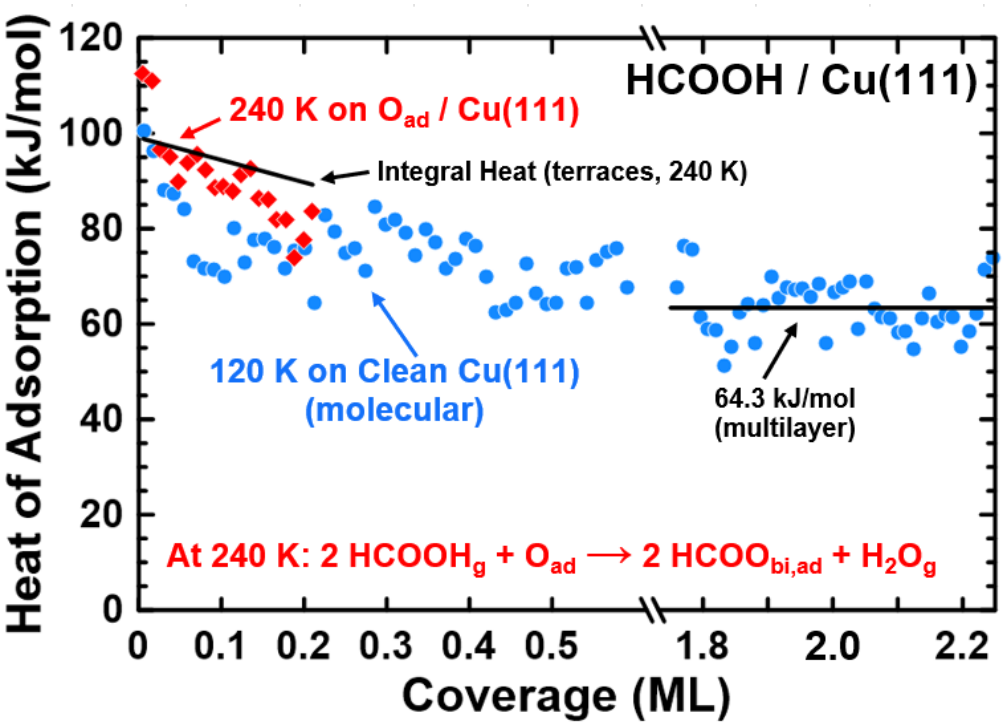

Figure 6-2. Differential heats of adsorption of formic acid on clean Cu(111) at 120 K (blue circles) and O-precovered Cu(111) at 240 K (red diamonds) as a function of the HCOOH-derived adsorbate coverage. The average heat of molecular adsorption reached at the multilayer limit is shown by the black line through the 120 K data, giving 64.3 ± 2.9 kJ/mol. The integral heat of adsorption for 240 K is shown in black from the low coverage limit, fit by (99.1−46.8θ) kJ/mol and giving 89.7 kJ/mol at saturation (θ = 0.20 ML). 1 ML = 1.77×10^{19} adsorbates per m^2.

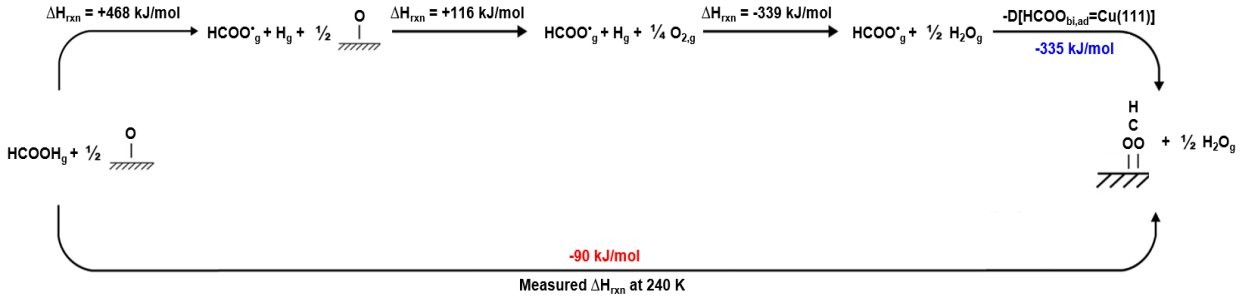

Figure 6-3. Thermodynamic cycle used to determine the total bond enthalpy of bidentate formate to Cu(111) (formate gas to surface-bound bidentate formate) from the integral heat of dissociative formic acid adsorption at 240 K and 0.20 ML of formate (90 kJ/mol, shown in red). The top right-hand step shows the enthalpy to form bidentate formate from gas-phase formate radical, which provides an estimate of the total bond enthalpy of bidentate formate to Cu(111), from both its O-Cu bonds. Values in red are experimental values from this study, black are taken from literature as described in the text, and blue values are values that were extracted using this cycle.

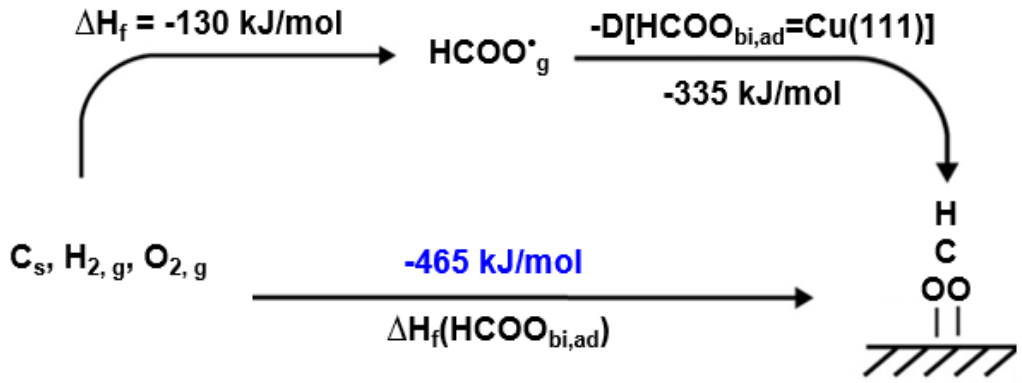

Figure 6-4. Thermodynamic cycle used to determine the total enthalpy of formation of bidentate formate on Cu(111) using the total bond enthalpy extracted from the thermodynamic cycle above (Figure 6-3). The bottom pathway shows the total enthalpy to form surface-bound bidentate formate from elements in their standard states. Values in black are previously extracted values or tabulated enthalpies of formation as referenced in the text, and blue values are values that were extracted using this cycle.

6.7 Tables

Table 6-1. Comparison of the present calorimetric bond energies of bidentate and monodentate formate to the Cu(111) surface with calculated values using DFT.

Coverage	Functional or method	$HCOO_{bi,ad}$ bond energy (kJ/mol)	$HCOO_{mono,ad}$ bond energy (kJ/mol)	Ref.
0.20 ML (1/5 ML)	Calorimetry	333	305	This paper
0.11 ML (1/9 ML)[a]	Calorimetry	337	309	This paper
DFT:	--	--	--	--
0.11 ML (1/9 ML)	RPBE	242	200	[101]
0.11 ML (1/9 ML)	PBE-DFT-D2	253	218	[100]
0.11 ML (1/9 ML)	PW91 / (PW91 with ZPE)	268 / (253)	217 / (206)	[91]
0.25 (1/4 ML)	GGA-PW91 / (GGA-PW91 with ZPE)	267 / (253)	224 / (210)	[89]

[a] As many DFT values reported here are calculated at 0.11 ML coverage, the experimentally determined bond enthalpy values of bidentate and monodentate formate to Cu(111) were also calculated at 0.11 ML in an identical manner to that at 0.20 ML but using the integral heat value at 240 K and 0.11 ML of 94 kJ/mol.

Table 6-2. Comparison of calorimetrically measured bond enthalpies and enthalpies of formation of monodentate and bidentate formate on Pt(111), Cu(111), & Ni(111).

	Bond enthalpy $HCOO_{mono,ad}$ (kJ/mol)	**Bond enthalpy $HCOO_{bi,ad}$ (kJ/mol)**	**ΔH_f $HCOO_{mono,ad}$ (kJ/mol)**	**ΔH_f $HCOO_{bi,ad}$ (kJ/mol)**	**Coverage (ML)**
Pt(111)	221 (ref.[36])	254[a] (ref.[30])	-345 (ref.[155])	-381 (ref.[155])	0.25
Ni(111)	292[b] (ref.[36])	320 (ref.[35])	-422[c] (ref.[35])	-449 (ref.[35])	0.143
Cu(111)	307	335	-437	-465	0.20

[a] The bond enthalpy of bidentate formate on Pt(111) is only reported at 0.375 ML coverage, while the rest of the values are available for a coverage of 0.25 ML. [b] The bond enthalpy of monodentate formate on Ni(111) is reported at 0.20 ML, while the rest of the values are only available at 0.143 ML. [c] The enthalpy of formation of monodentate formate on Ni(111) was calculated using the calorimetry data measured previously[35] in a thermodynamic cycle identical to that used to calculate the enthalpy of formation of bidentate formate in that same paper[35], but instead using the monodentate formate bond enthalpy published later by our group (292 kJ/mol)[36], which corresponds to dissociation of HCOOH gas to make monodentate formate and a hydrogen adatom.

Table 6-3. Summary of adsorption energies taken from DFT[186], and the resulting calculated reaction enthalpies and predicted TPD desorption peak temperatures for H_2O desorption from Cu(111), Cu(100), & Cu(110), compared to published TPD results[177].

Crystal surface:	**Cu(111)**	**Cu(100)**	**Cu(110)**
$\Delta E_{ads,DFT}$ of OH_{ad} (kJ/mol) (ref.[186])	-315	-389	-349
$\Delta E_{ads,DFT}$ of O_{ad} (kJ/mol) (ref.[186])	-488	-524	-509
$\Delta E_{ads,DFT}$ of H_2O_{ad} (kJ/mol) (ref.[186])	-21	-24	-37
$\Delta H_{rxn,DFT}$ for: $2\ OH_{ad} \rightarrow H_2O_g + O_{ad}$ (kJ/mol)	70	83	119
$\Delta H_{rxn,DFT}$ for: $2\ OH_{ad} \rightarrow H_2O_{ad} + O_{ad}$ (kJ/mol)	49	59	82
Predicted T_{max} for H_2O desorption (K)	244	286	407
Predicted T_{max} if $\Delta H_{rxn} = (0.70*\Delta H_{rxn,DFT})$ (K)	173	202	287
T_{max} from TPD (K) (ref.[177])	160	220	290

Chapter 7 Aqueous phase catalytic and electrocatalytic hydrogenation of phenol and benzaldehyde over platinum group metals

This chapter has reprinted with permission from reference[112]:

Singh, N., Sanyal, U., Ruehl, G., Stoerzinger, K. A., Gutiérrez, O. Y., Camaioni, D. M., Fulton, J. L., Lercher, J. A., & Campbell, C. T. Aqueous phase catalytic and electrocatalytic hydrogenation of phenol and benzaldehyde over platinum group metals. *Journal of Catalysis* **382**, 372–384 (2020).

Chapter Abstract

The mechanisms of aqueous-phase thermal catalytic hydrogenation (TCH) and electrocatalytic hydrogenation (ECH) of organic molecules over Pt group metals are not as well-understood as gas-phase thermal catalytic hydrogenation. In gas-phase, the reactions generally occur via a Langmuir-Hinshelwood mechanism with adsorbed hydrogen adding to adsorbed organics. Here, we show that the rates, reaction orders and activation energies for TCH and ECH of phenol and benzaldehyde on Pd, Pt, and Rh can be explained with a simple kinetic model based on similar Langmuir-Hinshelwood mechanisms. For Pt/C, the adsorption equilibrium constants for the organics needed to fit the rate data are consistent with independently-measured values, provided we assume that the rates are dominated by (111)-like sites, in agreement with reported particle size effects. The reaction rate of Pd in the ECH of benzaldehyde increases with the surface hydrogen coverage. The state of Pd during ECH of phenol and benzaldehyde are very different, with a high concentration of adsorbed H in the presence of phenol, but not in the

presence of benzaldehyde, consistent with benzaldehyde's stronger binding to the surface. In consequence, Pd is converted to β-PdH_x during the hydrogenation of phenol but not benzaldehyde. This is proposed to explain the much lower activity of Pd for hydrogenation of phenol compared to benzaldehyde. The measured low coverage of H on Pd in the presence of benzaldehyde is in agreement with the high selectivity/Faradaic efficiency of protons to benzaldehyde hydrogenation to benzyl alcohol. The decrease in apparent activation energy for ECH versus TCH can also be understood within this same kinetic model. The combination of ECH and TCH kinetics and spectroscopy has, thus, allowed to deduce a microkinetic model for these hydrogenation reactions.

It should be noted that I was not the primary author on the paper summarizing the research of this chapter. I did not contribute to the collection and analysis of the X-ray scattering studies, but those portions have been included for completeness of narrative and the full context of the conclusions of that research.

7.1 Introduction

Catalytic and electrocatalytic reactions on Pt group metals in the aqueous phase are important for carbon neutral pathways to fuels and chemicals[107,191–193]. Understanding the reaction mechanisms involved in these transformations is important to improving catalytic reaction rates, either by controlling reaction conditions to maximize rates on a given catalyst, or selecting new catalysts that have better properties, leading to higher activity.

Thermal catalytic hydrogenation (TCH) of organics on metal surfaces in gas phase tend to proceed through a hydrogen atom addition, in which an adsorbed surface hydrogen (H*) reacts with an adsorbed organic molecule[194]. The same mechanism has been proposed to occur in aqueous phase TCH[191] and for electrocatalytic hydrogenation (ECH) on metals with low hydrogen overvoltage (e.g., Pt, Rh, Pd)[195–197]. Electrocatalytic hydrogenation of phenol to cyclohexanone and cyclohexanol on platinum group metals appears to follow this mechanism, because catalysts share similar activation energies and product distributions to TCH[119,198,199]. If TCH and ECH follow the same mechanism, the main difference in conversion rates between ECH and TCH must be caused either by different coverages of H* (and its effect on organic coverage) or by a change in electronic properties of the metal catalyst by the applied potential. Since XANES of Pt has shown only subtle changes in the electronic properties[200], this second explanation seems unlikely. The H* coverage is determined by the H_2 pressure for TCH and by the activity of hydronium ions near the electrode surface and the external electric potential for ECH.

Benzaldehyde hydrogenation to benzyl alcohol on platinum group metals behaves differently than phenol, in that the activation energy in ECH is 7 kJ/mol lower than in TCH for Pt, Pd and Rh[120]. ECH of benzaldehyde is also interesting in that it has higher current selectivity

than phenol towards ECH versus H_2 evolution, particularly for Pd (~99% towards ECH). In contrast, Pd has extremely low activity for phenol hydrogenation (both TCH and ECH) compared to Pt or Rh[201].

The reason for the low activity for phenol ECH/TCH on Pd compared to Pt or Rh is unclear, since benzaldehyde ECH or TCH on Pd is comparably fast or faster than on Pt or Rh. One possible reason for the low TCH or ECH phenol activity on Pd may be a different reaction pathway for phenol hydrogenation on Pd compared to Pt as supported by calculations, which showed that hydrogenation on Pd(111) proceeds through a phenoxy intermediate rather than the direct hydrogenation route as predicted for Pt(111)[202]. Here we propose instead that the different Pd structure observed during benzaldehyde hydrogenation (metallic Pd) than phenol hydrogenation (β palladium hydride) causes this difference in reactivity.

The present study clarifies the reaction kinetics and mechanism of phenol and benzaldehyde ECH and TCH over the platinum group metals, Pt, Pd and Rh. This is done by measuring and comparing TCH and ECH rates, selectivities, activation energies, and reaction orders with respect to the organic species and hydrogen on Pt/C, Pd/C and Rh/C catalysts, and by measuring the surface species and catalyst structure under reaction conditions for Pd/C catalysts using EXAFS and XANES. Two main research questions are addressed here: (i) Can a mechanism involving adsorbed H addition to an adsorbed organic species as the rate-limiting step capture the observed kinetic behavior, including the positive reaction orders (~1) in benzaldehyde reported for benzaldehyde ECH on Pt and Rh, and the reaction order near zero reported for Pd?[120] (ii) Why does Pd behave differently than Pt and Rh with respect to benzaldehyde and phenol hydrogenation kinetics?

To this goal, we measure the reaction orders in organic species for Pt/C and Pd/C ECH and TCH, to determine how organic concentrations (and thus coverages) affect the rates. We compare these results to previous results in the literature, varying concentrations here over a wider range to detect changes in reaction rate that are not measurable with minor concentration changes. We also perform in situ X-ray absorption spectroscopy including X-ray absorption near edge (XANES), and extended fine structure (EXAFS), cyclic voltammetry, and electrochemical impedance measurements to estimate the coverages of the adsorbed organic species and hydrogen on Pd/C to help determine how these coverages affect the rates in both ECH and TCH. For Pt/C, we favorably compare the adsorption equilibrium constants of phenol and benzaldehyde used in our kinetic model for the concentration-dependent rates to our previous direct measurements of these equilibrium constants on Pt surfaces[116]. This also helps to test a recently proposed[203] Eley-Rideal mechanism for ECH of benzaldehyde on Pd based on absence of a negative reaction order with respect to benzaldehyde concentrations at the concentrations studied.

7.2 Experimental Methodology

7.2.1 TCH of Phenol with Pd/C and Pt/C and Fitting to Reaction Model

Thermal catalytic hydrogenation of phenol was carried out by reducing the catalyst (Pt/C or Pd/C) in water, while sparging H_2 under stirring at 500 rpm, then introducing phenol into the sealed glass reactor cell under flow of hydrogen at 1 bar. Aliquots of 1 mL of solution were sampled periodically. To test the aliquots, the dissolved organic products and reactants in the aqueous solution were extracted into dichloromethane with a dimethoxybenzene internal standard and then measured by gas chromatography to calculate conversion as a function of time.

The flow rate of H_2 was varied and did not show change in the measured turnover frequencies. Turnover frequencies (TOFs) were calculated by normalizing to the number of surface metal sites measured by H_2 chemisorption. The rate constant ($k_{LH,c}$), K_A, and K_H-C_H in the Langmuir-Hinshelwood model were fitted to the measured TOFs as a function of phenol concentration by the method of least squares.

7.2.2 ECH of Benzaldehyde with Pd/C

Benzaldehyde was reacted in an electrocatalytic cell. The cell has been described in detail elsewhere[204]. The compartment containing the working electrode/reference electrode and the compartment with the counter electrode (Pt wire) were separated by a Nafion membrane. The double junction silver/silver chloride reference electrode was calibrated vs. reversible hydrogen electrode (RHE) using a Pt wire with 1 bar H_2 bubbled into solution. A SP-150 Biologic potentiostat was used to control the potential and the resistance (measured using impedance spectroscopy). Resistance was compensated during runs by 85%, with the remaining 15% corrected afterwards. Aliquots of 1 mL were extracted from the cell, and tested in the same manner as for TCH. Acetate buffer (pH 5) was used as supporting electrolyte.

7.2.3 Pd Foil Cyclic Voltammetry

A Pd foil was used for cyclic voltammetry (CV) experiments because a CV of the 5 wt% Pd/C catalyst at potentials above the potential for hydrogen evolution (HER) did not show evidence of hydrogen underpotential deposition (H_{upd}) or current that could be attributed to bulk hydride formation due to the high background capacitance of carbon at the low metal loadings. The 0.025 mm-thick Pd foil (Sigma Aldrich) of dimensions 0.5 cm x 1 cm (immersed in acetate buffer electrolyte, pH 5 electrolyte) was cleaned by flame annealing followed by rinsing in Millipore water, then electrochemically cleaned by multiple sweeps from -1 V to 1.3 V versus

Ag/AgCl in acetate buffer. The cleaned Pd foil was then cycled in the range of -0.4 V to 0 V versus Ag/AgCl in solutions with no organics, in a cell that had been cleaned to ensure no trace organics were present. A separate glass cell was used for cyclic voltammetry to prevent contamination by benzaldehyde or phenol residue from ECH runs. The potential range was selected to be above 0 V vs. RHE (~-0.5 V versus Ag/AgCl is 0 V versus RHE at pH 5) to avoid H_2 evolution and hydrogenation of the organic. Organics were introduced at varying concentrations into the cell and the cyclic voltammograms were repeated. The potentiostat and calibrated reference electrode used for ECH were also used for CV experiments.

7.2.4 Electrochemical Impedance Spectroscopy (EIS) of Pt and Pd

Details of Electrochemical Impedance Spectroscopy (EIS) on a polycrystalline Pd and Pt disk in the presence of phenol and benzaldehyde to determine the effect of organics on capacitance and charge transfer resistance are discussed in the Supporting Information.

7.2.5 X-ray Adsorption Spectroscopy of Pd/C

An electrochemical flow cell designed for X-ray absorption spectroscopy was used with a Ag/AgCl reference electrode. Details of the cell are reported elsewhere[200]. Electrolyte was flowed at 0.5 mL/min past a carbon felt loaded with Pd/C catalyst separated from the carbon counter electrode by a Nafion membrane. The working electrode was prepared by loading the catalyst onto a carbon felt. Degassed electrolyte was flowed through the cell to remove air pockets and during measurement to remove generated hydrogen or small traces of oxygen. The Pd/C catalyst was oxidized then reduced for 20 min to clean the surface after being loaded and exposed to electrolyte to remove adventitious carbon and surface oxide layer, respectively. Experiments were conducted at the Advanced Photon Source at Argonne beamline, Sector 20 BM.

7.2.6 X-ray Adsorption Near Edge Spectroscopy Peak Fitting

X-ray Absorption Near Edge Spectroscopy (XANES) that covered a broad energy range were background subtracted, normalized, and calibrated using ATHENA software[205]. The narrower-range (faster scan) XANES spectra (negative log of I_T/I_0, giving the X-ray absorption coefficient for the sample, $\mu(E)$) were unnormalized and fit using an iterative solver minimizing the sum of least squared differences of two Gaussian peaks overlayed with a linear baseline compared to the spectra. The shift in Gaussian peak location (the higher energy value of these two peaks) was used to identify the transition of the Pd catalyst to a β-PdH_x.

7.2.7 Extended X-ray Adsorption Fine Structure Fitting

Extended X-ray Absorption Fine Structure (EXAFS) fitting was done using ARTEMIS[205,206], with FEFF9[207] theoretical standards as input. EXAFS spectra fitting was done with the first four Pd-Pd single shells and two multiscattering Pd-Pd shells, as well as two Pd-C pathways at different Pd-C distances. Due to noise in the data, Pd-C CN and Debye-Waller factor had very high uncertainty for some samples, and so a constant Debye-Waller of 0.005 $Å^2$ was used based on instances where data quality was higher. The Pd-C coordination numbers of both paths were fit using a single variable. S_0^2 (Amplitude reduction factor) = 0.7975, ΔE_0 = -2.118 eV were used for fits based on the reference Pd foil spectra taken concurrently with the Pd/C samples. The approach of fitting using Pd-C was drawn from previous work with Pt/C with phenol[200] and benzaldehyde[114].

7.3 Results

7.3.1 ECH and TCH of Phenol and Benzaldehyde on Pt, Rh, and Pd Supported on Carbon

We summarize first our new and previously reported aqueous-phase hydrogenation rate and selectivity measurements. The TOFs of TCH and ECH of phenol and benzaldehyde on carbon-supported Pt, Rh and Pd measured and those from the literature[115,120,204] are summarized in Table 7-1. The hydrogenation products from phenol were cyclohexanone and cyclohexanol formed in series, with >95% combined selectivity. Under the reaction conditions studied, the conversion of cyclohexanone to cyclohexanol had a slightly slower rate than the conversion of phenol to cyclohexanone, so that cyclohexanone was the dominant product at the low conversions used in the rate measurements below (i.e., Tables 7-1 and 7-2 and Figures 7-1 and 7-2). The sole product observed from benzaldehyde was benzyl alcohol with >95% selectivity. The Faradaic efficiency to ECH (the current utilized towards hydrogenation of phenol and benzaldehyde rather than H_2 production) is shown in Table 7-1. Both phenol and benzaldehyde are converted rapidly on Pt and Rh in TCH and ECH. Phenol, in contrast, is converted slowly on Pd. (Phenol's ECH activity on Pd was too low to be measured accurately, including our attempts in this work, which were measured for shorter times than TCH and set the TOF for ECH at $<0.002\ s^{-1}$.) Despite low phenol ECH activity compared to Pt and Rh, Pd is more active for ECH of benzaldehyde than Pt or Rh. No evidence for products involving C-C bond cleavage was observed in our results or those reported in Refs. [115,120,204,208]. Also, if C-C cleavage happened and it produced large coverages of strongly-adsorbed products like CO and phenyl, then the equilibrium constants for phenol and benzaldehyde adsorption obtained from the kinetic modelling below would not agree with those measured independently, as we find below.

On Pd, the Faradaic efficiency of ECH was very high for benzaldehyde (99%, Table 7-1), but low for phenol. The Faradaic efficiency of ECH of benzaldehyde and phenol were similar on Pt, and both lower than ECH of benzaldehyde on Pd. The total reduction current during benzaldehyde ECH (sum of the currents towards H_2 and ECH) was similar for Pt and Pd[120], indicating that ~50x less H_2 is evolved during ECH of benzaldehyde on Pd than on Pt. (Approximately 1% of the current is used to reduce hydronium ions to H_2 on Pd while ~50% goes to H_2 on Pt.) Despite the low activity of Pd for phenol ECH, the total reduction current was similar to that of benzaldehyde ECH on Pd, suggesting that adsorbed H (H*) are produced and react at similar rates, but a much larger fraction of these react with benzaldehyde than with phenol.

7.3.2 ECH and TCH Rates as a Function of Temperature and Concentration with Comparison to Reaction Model

We now summarize the effects of organic concentrations, H_2 pressure, and temperature on the rates, and fit some of these data to a Langmuir-Hinshelwood microkinetic model, which assumes that the rate-determining step is the addition of an adsorbed hydrogen to the adsorbed organic. This type of model was already used successfully to explain the effect of pH on the TCH rate for phenol over Pt/C, which results from the known change in adsorbed hydrogen stability with pH[114]. Further comparison of this model to the data is presented later in this chapter.

The effect of organic concentration at different H_2 pressures (for TCH) or applied potentials (for ECH) is shown in Figure 7-1. The reaction orders at 20 mM and apparent activation energies for phenol and benzaldehyde TCH and ECH measured in this work and from literature are compiled in Table 7-2. Under TCH conditions at 1 bar, the order in H_2 was

approximately 1 for all cases[115,120,201]. For Pd and Pt TCH of phenol, the TOFs over a wider range of phenol concentrations are shown in Figure 7-2. Benzaldehyde solubility in water (<50 mM at 298 K) limits the range of concentrations that can be tested for benzaldehyde TCH and ECH.

TCH of phenol on Pd/C initially increased in rate with increasing concentration of phenol (20–200 mM), but then has an increasingly negative order in phenol at higher concentrations (>200 mM) (Figure 7-2a). This negative order indicates that adsorbed phenol blocks Pd sites at sufficiently high coverages. The data for all three metals and both organics are interpreted using a Langmuir-Hinshelwood mechanism, in which the surface hydrogenation (addition of an adsorbed H atom to the adsorbed organic) is rate-limiting. A fit of the data to the quantitative reaction rate equation described below (and derived in the SI) is shown in Figure 7-2a for phenol hydrogenation over Pd. K_A refers to the adsorption coefficient of phenol on the Pd surface, C_A is the phenol_{aq} concentration (relative to the standard concentration of 1 M), and K_H similarly refers to H adsorption and C_H is the aqueous hydrogen concentration (the standard state for C_H is explained below). We use C_H rather than hydrogen pressure, P_{H_2}, here to express the effective aqueous hydrogen concentration (or activity) for both ECH and TCH, thereby allowing both H^+_{aq} and $H_{2,aq}$ to be treated with the same rate equations in the SI. As discussed in the SI, during TCH, C_H is really an "effective first-order concentration" actually given by $C_H = (P_{H_2}/(1\text{ bar}))^{1/2}$ in TCH, whereas in ECH, C_H is just the concentration of H^+_{aq} (divided by 1 M). In both TCH and ECH, K_H is defined as the equilibrium H* coverage divided by this C_H thus defined. Note that K_H in ECH should increase exponentially with decreasing applied potential (i.e., approximately following the Nernst equation, as described in the Supporting Information), and is thus much larger in value under the ECH conditions studied here than under the TCH conditions at 1 bar H_2.

Based on the value for K_A of 38 from the fit, 50% coverage in phenol may be expected around 0.09 M phenol (including competition with hydrogen within this model).

The rate of TCH of phenol on Pt is shown in Figure 7-2b for a range of initial concentrations from 6 mM to 1.62 M. Over this wide concentration range, the reaction order changed as was observed for Pd. The rate increased with phenol concentration until it reached a maximum, after which the rate decreased. The order was ~0.6 at 20 mM phenol in Figure 7-2b (based on the reaction model fit to the experimental data), whereas prior reports stated that the order in phenol concentration was ~0.3 at the same conditions[117]. We attribute this difference to the very narrow phenol concentration range explored in the previous report. Our own more recent measurements for TCH of phenol on Pt/C[8] covered such a small concentration drop with time (only 39%) that the data are equally well fit by orders of 0 and 0.5 (relative standard deviations of 2.7% and 3.1%, respectively). For similar reasons, we omit from Table 7-2 the previously reported order for phenol ECH over Pt[117]. The measurements in Figure 7-2b cover a much wider concentration range and are far more accurate. Although previously at high phenol concentrations (~160 mM)[115], a negative order in phenol was not observed for TCH on Pt/C, as is observed in Figure 7-2b, those measurements were at higher H_2 pressure (20 bar), where H_2 would compete for sites more effectively than at 1 bar (Figure 7-2b). We show below that a simple Langmuir-Hinshelwood mechanism with competitive adsorption of the two reactants can be used to approximately describe the behavior in Figure 7-2, and those previous results. We also show that the adsorption equilibrium constants for phenol and benzaldehyde needed in these models for Pt/C are consistent with our independent measurements of these on Pt surfaces[116], if we assume that the hydrogenation reactions occur mainly on (111)-like facets and not at steps or

(110)/(100)-like sites. This assumption was suggested by the observation that larger Pt particles are more active per unit Pt area[117].

Under ECH conditions, benzaldehyde ECH is first order in benzaldehyde concentration on Pt and Rh and zero order on Pd[120]. Another difference between Pd and Rh or Pt for ECH of benzaldehyde is that as the overpotential is increased for benzaldehyde ECH (from -0.6 V to -0.9 V versus Ag/AgCl in Figure 7-1d), Pd goes from being comparable in rate to Pt and Rh to being ~4x more active (at 20 mM benzaldehyde). The implications of these differences will be discussed further below. The activation energy for ECH and TCH are similar for phenol for Pt and Rh, but ECH of benzaldehyde has a 7 kJ/mol lower activation energy than TCH for Pt, Rh and Pd.

7.3.3 Cyclic Voltammetry of Pd and Pt in Presence of Phenol or Benzaldehyde

We have previously used cyclic voltammetry on a well-annealed Pt wire to determine how the coverage of adsorbed phenol and benzaldehyde on Pt increases with their aqueous-phase concentrations[116]. This was done by measuring the corresponding decrease in the so-called H_{upd} current associated with adsorbing (and removing) adsorbed H. In the Supporting Information, we present a similar type study using a Pd foil. This is more complex, since the adsorption of H^+ to make H* does not stop at ~1 monolayer as it does for Pt, but also produces H dissolved in the bulk of Pd and even Pd hydride. The results nevertheless reveal the concentration ranges where phenol and benzaldehyde adsorb onto Pd (Figure 7-S4). From that, it is easy to conclude that the Pd surface binds benzaldehyde considerably more strongly than phenol.

7.3.4 In situ X-ray Adsorption Spectroscopy and EIS Measurements in the Presence of Benzaldehyde or Phenol

We summarize here our in situ spectroscopic and EIS measurements of adsorbed species on Pd and Pt, and the effects of organic concentrations on the transition of Pd to Pd hydrides. Our previous work with both X-ray absorption near edge (XANES) and extended X-ray absorption fine structure (EXAFS) on Pt/C in the presence of phenol[116,200] and benzaldehyde[116] were used to probe the coverages of H and organics on the surface under reaction conditions. These results confirmed earlier reports that on Pt, the rate of phenol hydrogenation is controlled by the surface hydrogenation of adsorbed phenol[200]. Detection of adsorbed organic and hydrogen also showed that the organic and hydrogen appear to compete for sites on the Pt surface[116,200].

XANES and EXAFS can be used to identify the relevant Pd phases including Pd oxide, the β Pd hydride phase (which we will refer to as β-PdH_x, where x is >0.58 for bulk Pd[209], and has been reported to be as low as 0.4 for Pd/C nanoparticles[210]), and α-PdH_x (the H-lean solid phase where $x < 0.03$ for bulk Pd at 298 K, but $x < 0.15$ for nanoparticles[210] and x up to > 0.5 for bulk Pd above 570 K). Although Pd nanoparticles show separate hydride phases at > 2 nm sizes, the relationship between x and the phase transition onset varies compared to that of bulk Pd, as discussed in the SI[209,210]. XANES in particular has been used to discriminate between the formation of a palladium carbide versus the Pd hydride even though EXAFS and X-Ray Diffraction (XRD) cannot[211]. (Both XRD and EXAFS only detect resultant Pd structural changes such as the Pd-Pd distance, while XANES detects electronic effects due to Pd-C.) The two prominent Pd K-edge XANES peaks have been used to rapidly discriminate between the α-PdH_x or β-PdH_x phases on a ~4 nm Pd/C electrocatalyst in the presence of CO_2 [212]. A scan of the Pd K-

edge (Figure 7-3a) shows the major change in XANES between a partially oxidized Pd/C sample compared to one that has been reduced at -0.55 V.

As mentioned, Figure 7-3b shows the shifts in the two XANES peak energies that are used to distinguish the β-PdH_x from that of the Pd metal (such as Pd foil) or α-PdH_x. By acquiring short energy scans in the region of these two XANES peaks while varying the cell potential, a rapid determination of the Pd state is obtained[211–213]. As shown in Figure 7-3b, the Pd metal converts to a β-PdH_x at more negative potentials as the first peak at ~24369 eV shifts 1 eV negative and becomes more narrow, while the second peak at 24390 eV shifts slightly negative. If this were formation of a carbide, the peak at ~24369 eV would shift positive by 1 eV and become broader[211]. Thus, this shift is primarily attributed to the formation of the β-PdH_x. In lieu of a full EXAFS scan, this method allows rapid probing of the catalyst phase during a sweep of the potential. The decrease in μ(E) (absorption coefficient) for peaks taken at more negative potential is caused by the increase in X-ray transmission that varies with increasing H_2 concentration in the solution (see Supporting Information).

The location of the XANES peak at ~24390 eV is plotted in Figure 7-4 as the applied potential is swept cathodically (scan rate 0.6 mV/s), and shows the change in the catalyst from a Pd metal or α-PdH_x to the β-PdH_x. From this, it is evident that there is a transition from α-PdH_x to β-PdH_x at -0.55 to -0.60 V versus Ag/AgCl in acetate buffer, which can be reversed by returning to more positive potentials (Figure 7-S3a). If phenol is present, this transition occurs at approximately the same potential (Figure 7-4). In the presence of benzaldehyde, the formation of β-PdH_x is inhibited (Figure 7-4), even though the amount of charge (integrated current) passed during the negative potential sweep is more than sufficient to completely convert to β-PdH_x (Figure 7-S3b). Based on the lack of change in transmission (indicating the absence of an

increase in H_2 in the solution) in the presence of benzaldehyde, a negligible fraction of the reduction current for benzaldehyde ECH was directed towards H_2 evolution (Figure 7-S3b), consistent with the high Faradaic efficiency of Pd for ECH of benzaldehyde (Table 7-1). The absence of the β-PdH_x in XANES in the presence of benzaldehyde is qualitatively similar to the cyclic voltammetry study of Pd foil described in the SI, where the amount of Pd hydride formed (based on charge) during a negative sweep is inhibited more by benzaldehyde than by phenol at the same solution-phase concentrations (Figure 7-S4). Under these conditions, the reduction current induces the reversible formation of α-PdH_x, indicating negligible current related to reaction with benzaldehyde or phenol. As discussed in more detail in the SI and below, these data show that benzaldehyde binds more strongly to Pd than does phenol (and has a higher coverage under reaction conditions), and so the corresponding coverage of H* on Pd during hydrogenation catalysis is lower for benzaldehyde than phenol.

The β-PdH_x forms after the surface is populated with a higher concentration of adsorbed H[214], and, for α -PdH_x, the concentration of H in the bulk scales with steady state coverage of adsorbed hydrogen[215,216]. The absence of β-PdH_x in the presence of benzaldehyde implies less available surface hydrogen (lower hydrogen coverage). This lower hydrogen coverage may be due to strong adsorption of benzaldehyde on the surface (blocking sites for hydrogen adsorption) and/or high reactivity of benzaldehyde (which would consume surface hydrogen rapidly, forcing a low steady-state coverage of hydrogen).

EXAFS spectra of Pd/C were acquired under constant potentials where the β-PdH_x forms (-0.6 V versus Ag/AgCl) and where α-PdH_x forms (-0.55 V versus Ag/AgCl). These spectra provided a basis for comparison to the same conditions in the presence of phenol or

benzaldehyde. Typical Pd K-edge Im[χ] EXAFS spectra are shown in Figure 7-S5 for several conditions.

Fitting of the experimental spectra to the theoretical standards (from FEFF9) yields the structural parameters reported in Table 7-3. The Pd-Pd coordination number indicates the particle sizes are ~3nm[217], small enough that Pd behaves differently than bulk in terms of chemical reactivity and hydride formation[117,214,218,219], but large enough that there are still distinct hydride phases, although with different [H]/[Pd] ratios (x) than in the bulk[210,220]. As recently reported[210], this is suggested to be due to the competing interactions of the core Pd that behaves similar to bulk Pd and the outer shell of Pd that becomes more significant at smaller particle sizes. The average 1st shell Pd-Pd distances in Table 7-3 confirm that at -0.6 V versus Ag/AgCl, the Pd-Pd distances are substantially larger than that of the bulk foil and, therefore, correspond to the presence of H dissolved in the Pd phase, consistent with β-PdH_x [210,214,221]. At -0.55 V versus Ag/AgCl, the Pd-Pd distances are shorter, but still larger than for the bulk foil, indicating that less H is dissolved under these conditions. The Pd-Pd distances in the presence of 20 mM phenol are similar to those measured in absence of phenol. The distances initially contract (possibly to those of the α-PdH_x) in the presence of benzaldehyde at both -0.55 V and -0.6 V. However, the lattice expands with increasingly negative potentials, even in the presence of benzaldehyde, although not to the extent observed under mild reducing conditions in the absence of benzaldehyde until -1.2 V (at which the current is sufficiently high to completely convert the benzaldehyde being flowed past the catalyst, see SI).

The average Pd-Pd distance change (fractional lattice expansion $\delta l/l_0$) can be used to estimate the H/Pd atomic ratio for the H dissolved in the Pd bulk via[221]:

$$\frac{\delta l}{l_0} = 0.0666\frac{[H]}{[Pd]} - 0.0164\left(\frac{[H]}{[Pd]}\right)^2 \quad (7\text{-}1)$$

Although Equation 7-1 was derived for bulk Pd above the critical point temperature, it can be used semi-quantitatively for Pd/C nanoparticles and for both α and β phases[214]. (The relationship between the Pd-Pd distance and [H]/[Pd] is discussed in greater detail in Ref.[210] and in the SI, Figure 7-S6.) Figure 7-5 shows the [H]/[Pd] ratio of the Pd/C under different electrochemical conditions based on the 1st shell Pd-Pd distance expansion using Equation 7-1. Here we assume that the Pd/C obeys the same equation as bulk Pd, and that the values of the foil constitutes the starting Pd-Pd distance (strictly, should be the Pd-Pd distance of a bare nanoparticle). Since the amount of hydrogen in the bulk is determined by the steady state hydrogen coverage on the surface[215], and scales linearly with it[216], [H]/[Pd] can act as an estimate of the relative hydrogen coverage. Figure 7-5 shows this hydrogen coverage is much lower in the presence of benzaldehyde than in the presence of phenol. However, changing the potential from -0.6 to -1.2 V causes an increase in the bulk H concentration (and thus the surface concentration, proportionally), from 2.5% to ~20%. The increase [H]/[Pd] from -0.6 V (0.027) to -0.9 V (0.10) mirrors the increase in rate for ECH of benzaldehyde on Pd over these same potentials (0.37 s^{-1} at -0.6 V to 1.08 s^{-1} at -0.9 V)[120] as shown in Figure 7-1, and replotted in Figure 7-5. A comparison of the reduction current during the EXAFS measurement to the [H]/[Pd] ratio also shows a similar correlation when benzaldehyde is present (Figure 7-S7).

The inhibition of the β-PdH_x in the presence of benzaldehyde detected by EXAFS corroborates the XANES data from Figure 7-4 that the Pd/C catalyst has a low hydrogen coverage in the presence of benzaldehyde. This result has been observed both at steady state conditions (EXAFS), as well as under slowly decreasing potentials (XANES). This indicates that the high reactivity of Pd for benzaldehyde ECH is not due to the formation of a β-PdH_x phase, differentiating it from reports of the β-PdH_x being more active for CO_2 reduction than Pd

metal[212]. It is speculated, in contrast, that the high benzaldehyde activity is caused by metallic states of Pd in the presence of benzaldehyde, and the increase in ECH rate with more negative potential is caused by a higher hydrogen coverage.

The EIS measurements summarized in the SI show that adsorbed phenol covers a large fraction of the Pt disk's surface, and that benzaldehyde covers an even larger fraction, under their ECH reaction conditions studied there. The EIS results also confirm that the rate of ECH over the Pd disk is faster for benzaldehyde than phenol (consistent with our direct rate measurements over Pd/C above).

7.4 Discussion

7.4.1 Faradaic Efficiency Towards ECH and Relation to Hydrogen Coverages

We show next that the high Faradaic efficiency of Pd for ECH of benzaldehyde implies the adsorbed H (H*) coverage (θ_H) is low in the presence of benzaldehyde. The hydrogen evolution reaction (HER) current in the presence of benzaldehyde is ~1% of that without benzaldehyde (99% Faradaic efficiency towards ECH of benzaldehyde at comparable total currents to without benzaldehyde). Assuming HER current is proportional to θ_H^2 or θ_H, based on a Tafel or Heyrovsky mechanism[222], this implies θ_H on Pd must only be 1–10% of that in the absence of benzaldehyde (assuming in the absence of benzaldehyde that θ_H ~1). At pH 5, the exchange current density of Pd for HER is ~2–5 times lower than Rh or Pt (respectively), in the absence of organics[223], and yet the HER current at similar potentials in the presence of benzaldehyde is much lower for Pd than Pt or Rh (1% of that in HER for Pd, ~50% for Rh or Pt). Again, using the assumption that the HER current is proportional to θ_H^2 or θ_H under the same overvoltages, this indicates that Pd has a lower hydrogen coverage under benzaldehyde ECH

conditions than either Pt or Rh. The XANES and EXAFS results also indicate the θ_H is much lower on Pd in the presence of benzaldehyde than in its absence or in the presence of phenol. This lower θ_H on Pd than Pt or Rh in the presence of benzaldehyde is either due to benzaldehyde consuming H* much faster on Pd than Pt or Rh, or benzaldehyde (or its products) blocking sites more efficiently on Pd (i.e., higher coverage) than on Pt or Rh, or both. The first explanation can be ruled out, since it is inconsistent with the similar TOF for these three metals (Table 7-1), which is only 50% higher for Pd than Pt or Rh. The second explanation is more viable, since it is also consistent with the fact that the reaction order in benzaldehyde is zero for Pd but one on Pt and Rh (see below). Based on the cyclic voltammetry with a Pd foil (Figure 7-S4), benzaldehyde greatly reduces the amount of α-hydride formed, even though the current due to benzaldehyde hydrogenation is very low (evidenced by the observed similarity in areas of the α-hydride formation and removal peaks), at potentials above 0 V versus RHE, also supporting the hypothesis of site-blocking.

From the cyclic voltammograms, phenol binds more weakly to Pd than benzaldehyde does, based on the lower inhibition of the bulk Pd hydride formation by 20 mM phenol (~50% inhibited) than by 20 mM benzaldehyde (~75% inhibited) (Figure 7-S4). Although the cyclic voltammogram can give a qualitative assessment of the relative binding strengths, it does not allow us to estimate coverages under reaction conditions at voltages more negative than 0 V versus RHE. However, the double layer capacitance in the presence of organic molecules remains reduced at -0.1 V versus RHE as observed by impedance spectroscopy (Figure 7-S8, Table 7-S1). This suggests organic (benzaldehyde or phenol) adsorption remains competitive with that of H* on Pt under cathodic bias, based on the inversely proportional relationship between double layer capacitance and organic coverage on metals in aqueous solution[224]. For Pd,

however, interpretation of adsorbate capacitance from impedance spectra is complicated by differences in bulk hydride formation.

7.4.2 Proposed Langmuir-Hinshelwood Reaction Model Involving Adsorbed Surface Hydrogen (H) Addition*

As noted above, we will use the same reaction model involving the addition of an adsorbed H to the adsorbed organic in the rate-determining step to explain all the data for all three metals and both organics. The fact that the Pd has the α-hydride present during benzaldehyde hydrogenation does not change its surface from being essentially pure metallic Pd, but this is not true during phenol hydrogenation, where the Pd converts to the β-hydride. So we expect qualitatively similar behavior for all three Pt group metals (except during phenol hydrogenation over Pd). However, there will be quantitative differences between the metals in the adsorption equilibrium constants for both the organic and hydrogen as well as in the rate constant for the rate-determining H-addition step. This explains the general similarities but also differences between systems in Figure 7-1[115,204].

For a kinetic model based on this simple mechanism to capture the observed kinetic and spectroscopic data, it must explain the observed behavior near room temperature, as summarized here for the conditions of Figures 7-1 and 7-2 and Tables 7-1 and 7-2:

1. The TOFs of phenol in both TCH and ECH are much slower on Pd than Pt or Rh, and much slower than the TCH and ECH TOFs of benzaldehyde on all three metals. Otherwise, the TOFs for all three metals in both TCH and ECH of both phenol and benzaldehyde are all within a factor of about 4. This is tentatively attributed to the fact that Pd has converted to the β-hydride in phenol hydrogenation conditions, so it is really a quite different material than all the other cases.

2. The rates of TCH and ECH of both phenol and benzaldehyde increase with increasing chemical or electrochemical driving force to make H* (i.e., H_2 pressure or applied voltage, respectively), on all three metals.

3. *In situ* X-ray absorption spectroscopies show that the H coverage on Pd is very low during benzaldehyde ECH but much higher during phenol ECH (indeed so high that the Pd converts to the β-hydride).

4. The Faradaic efficiencies for ECH of both phenol and benzaldehyde are in the range of 40–70% for both Pt and Rh, but it drops to < 1% for phenol on Pd and rises to ~99% for benzaldehyde on Pd.

5. The apparent activation energies are lower in ECH than for TCH, especially with benzaldehyde.

6. The rates of TCH and ECH of both phenol and benzaldehyde show reaction orders in organic concentration near 20 mM that vary from system to system (Table 7-2).

7. When the phenol concentration was varied over a much broader range, the TCH rates over both Pd and Pt were found to approach first-order in phenol concentration at low concentrations (<20 mM), be approximately zero order in phenol at 100 mM phenol, then approach an order of -1 at high phenol concentrations (>250 mM).

We explain these results based on a simplified 3-step microkinetic model for phenol and benzaldehyde hydrogenation (both ECH and TCH) which assumes a Langmuir-Hinshelwood mechanism wherein the two reactants adsorb competitively and then react:

$$A + * \leftrightharpoons A^* \ (K_A) \tag{7-2}$$

$$H + * \leftrightharpoons H^* \ (K_H) \tag{7-3}$$

$$A^* + H^* \rightarrow Product \ (K_{LH,c}) \tag{7-4}$$

Here, *A* represents the reacting aqueous-phase organic (phenol or benzaldehyde), H represents hydrogen (either H^+_{aq}/e^- (in ECH) or $½H_{2,aq}$ (in TCH)), * represents an open site, *A** represents the adsorbed organic (in whatever form is required for the rate-determining step) and *H** represents an adsorbed H atom. The rate-determining step is assumed to be H* addition to the adsorbed organic from the adsorbed hydrogen atom. We have assumed that the hydrogenation steps after this are fast. (Benzaldehyde has two H additions total, and phenol has four to form cyclohexanone, and two additional steps to form cyclohexanol).

From this mechanism (see Supporting Information and ref.[225] for derivations of rate equations), the rate ($r_{LH,c}$ for this Langmuir-Hinshelwood model with competitive adsorption) is of the form proposed for Figure 7-2[225]:

$$r_{LH,c} = k_{LH,c} \frac{K_A C_A K_H C_H}{(1 + K_A C_A + K_H C_H)^2} \quad (7\text{-}5)$$

where K_A is the adsorption coefficient (equilibrium constant) of A on the surface, C_A is the aqueous concentration of A (relative to the standard concentration of 1 M), and $k_{LH,c}$ is the rate constant for the surface hydrogenation (rate-determining) step. In ECH, C_H is the concentration of H^+_{aq} (divided by 1 M). In TCH, C_H is equal to the "effective first-order concentration" of aqueous H_2, $(P_{H_2}/(1\ \text{bar}))^{1/2}$. In both TCH and ECH, K_H is defined as the H* coverage divided by this C_H thus defined. The equilibrium constants and rate constant will depend on temperature and, for ECH, K_H should increase exponentially with decreasing applied potential (i.e., approximately following the Nernst equation as described in the SI). We assume they are constant under the conditions where we quantitatively fit data to this rate equation (only TCH at 25 °C). This model assumes that there is no difference between different binding sites (*), although the adsorption constants may depend on the exposed surface facet. As noted above, the

rate on Pt/C is dominated by the (111) facets. The effect of $K_H C_H$ on the rate and the coverage of the organic (θ_A) and hydrogen (θ_H) is shown for several conditions in Figure 7-S9.

The reaction model that best fits the data summarized above for both TCH and ECH of both phenol and benzaldehyde on Pd, Pt and Rh is the competitive adsorption model, where the organic is moderately strongly bound on the surface (K_A is moderate, Figure 7-6). This reaction model is consistent with the one used in Figure 7-2 where fitting shows $K_H C_H$ is approximately 2.5 and $K_A C_A$ ranges from 0.175 to 22. The competitive adsorption Langmuir-Hinshelwood reaction model (Figure 7-6, Figure 7-S9b) shows that for low $K_H C_H$ and moderate K_A, the reaction rate will increase with increasing $K_H C_H$ (increasing overvoltage or increasing hydrogen pressure), but C_A will not affect the rate (order in A is ~zero). Under these conditions, the coverage of A (θ_A) is relatively high (but does not completely saturate the surface), and the hydrogen coverage (θ_H) is low (but increases with increasing $K_H C_H$). At sufficiently high $K_H C_H$, the rate becomes positive order in C_A (and θ_A is low). In this regime, the rate begins to reach a maximum in $K_H C_H$, and the θ_H is high. (Figure 7-S9 shows that the concentration at which the rate reaches its maximum depends on the value of K_A). Figure 7-6b shows that the C_A also influences the coverages, changing the reaction order in A (discussed below as related to our experimental phenol TCH data in Figure 7-2).

The equilibrium constants K_A for phenol adsorption determined by the fit to the rate data in Figure 7-2 are very similar on Pd and Pt, i.e., 38 and 33, respectively. This value for Pt/C is very similar to the K_A for phenol adsorption we determined by direct aqueous-phase adsorption measurements on Pt(111)-like sites (exp[-(-9 kJ/mol)/RT] = 38 [116], but far below the value we determined for Pt steps sites or (110)/(100)-like sites (exp[-(-29 kJ/mol)/ RT] = 121000) [116]. This strongly supports the model presented and suggests that the hydrogenation occurs mainly on

(111)-like sites. Also, the equilibrium constant K_A for benzaldehyde adsorption we determined by direct aqueous-phase adsorption measurements on Pt(111)-like sites (exp[-(-27 kJ/mol)/ RT] = 54,100) [116] is much stronger than the K_A for phenol on those same sites, consistent with the much lower reaction order for benzaldehyde on Pt/C in Table 7-2 (~0) than for phenol on Pt/C (~0.6). This again supports the kinetic model presented, and highlights the high importance of the Pt(111)-like sites compared to Pt steps and (110)/(100)-like facets for both phenol and benzaldehyde hydrogenation rates. It is also consistent with the observation that the rate of both phenol and benzaldehyde hydrogenation is slower on smaller Pt nanoparticles[117], which have a smaller fraction of (111)-like sites.

The value of $K_H C_H$ = 2.32 for Pt/C from the fit of Equation 7-5 to Figure 7-2b at C_H = (1 bar)$^{1/2}$ gives K_H = 2.32 at 298 K, and a standard-state free energy of adsorption of H_2 of approximately -2 kJ per mol H*. This value is close to the values estimated by Yang et al.[226] from modeling kinetic measurements of H_2/D_2 exchange in aqueous phase over Pt on silicalite of + 1.6 kJ per mol H* at 303 K (based on their reported value of K_H = 0.28), and + 0.9 kJ per mol H* at 298 K (extrapolated using the standard enthalpy and entropy of adsorption they estimated based on K_H values in the range from 303 to 343 K).

Note that our fit value really reflects the H adsorption strength when phenol is also adsorbed (which may weaken H* binding), whereas the study by Yang et al. was in the absence of phenol. The hydrogen adsorption free energy (relative to 1 bar H_2 gas) was shown from H underpotential deposition on a Pt(111) surface in aqueous solution by Gómez et al.[227] to change strongly with H* coverage, from -4.8 kJ/mol H* near full coverage at 0.05 V versus RHE to -33 kJ/mol H* near zero coverage at 0.35 V versus RHE, with values of -22, -17, and -11 kJ/mol H* at fractional H* coverages of 0.2, 0.4, and 0.6, respectively[227]. This trend would require that the

value reported by Yang et al.[226] mentioned above correspond to H* coverages above 0.6 at the 30 bar H_2 pressure used there, compared to a value of ~0.5 reported by Yang et al. The differences between the measured (and calculated) thermodynamics of H* adsorption on Pt with and without water have been discussed previously[226,227]. The value we measure here is similar to the calculated standard free energy of adsorption on Pt(111) of H_2 gas at 300 K from DFT (-9 kJ per mol H* at 0.25 monolayers and -3 kJ per mol H* at 1 monolayer coverage in the absence of water, i.e., in vacuum)[228], although other DFT-based calculations showed that the standard free energy of H* relative to H2 gas at 343 K increases by 44 kJ per mol H* with the addition of water to the Pt(111) surface[226].

The similar phenol concentration dependences in the rate of TCH for Pd and Pt in Figure 7-2 implies that the phenol coverage is similar on Pd and Pt. Thus, phenol's much slower TCH and ECH rates on Pd than Pt is *not* due to differences in its coverage or the strength of phenol adsorption. The strength and rate of H* adsorption is also not expected to be much different between Pd and Pt (and Rh), since they are very similar in vacuum, with Pd binding H slightly more strongly[155,229], and their HER rates are within an order of magnitude[223]. The low phenol hydrogenation rate on Pd thus seems to be due to the much lower value of $k_{LH,c}$ for phenol on Pd compared to Pt (or Rh). Calculations indicate that on Pd(111), phenol hydrogenation proceeds through hydrogenation of an adsorbed phenoxy intermediate, rather than a direct hydrogenation of adsorbed phenol as predicted for Pt(111)[202]. This, however, does not explain why the species that hydrogenates in the slowest step on Pt is so much slower to hydrogenate on Pd. The $k_{LH,c}$ for that same phenol-derived species must still be much slower on Pd than Pt. We tentatively attribute this to the fact that, under reaction conditions for phenol hydrogenation, Pd is actually a

β-PdH_x, as shown in Figure 7-4, which could have a lower intrinsic activity for hydrogenation than metallic Pd.

Interestingly, benzaldehyde hydrogenation follows the opposite trend: its ECH and TCH rates are slightly higher on Pd compared to Pt and Rh. With benzaldehyde, however, there is a difference in reaction order in the organic in ECH, now 1st order on Pt and Rh but still zero order on Pd. This implies lower benzaldehyde coverage on Pt and Rh compared to Pd in ECH, which may lead to lower rates than on Pd. In spite of this low benzaldehyde coverage on Pt and Rh, the benzaldehyde ECH rate is still ~3-fold faster than phenol's ECH rate (where we know the phenol coverage is higher on Rh from its zero order, Table 7-2). Thus, the intrinsic rate constant ($k_{LH,c}$) for benzaldehyde is markedly higher than for phenol on Rh (and possibly Pt). Palladium also appears to have a higher intrinsic rate constant ($k_{LH,c}$) for benzaldehyde than phenol, since TCH and ECH rates on Pd are much higher for benzaldehyde than phenol. This is consistent with the reduced charge transfer resistance at -0.5 V versus Ag/AgCl observed from impedance spectroscopy for a Pd disk with benzaldehyde present compared to phenol (Figure 7-S8, Table 7-S1). This is also consistent with the observation for ECH of acetophenone and benzophenone on Pd nanoparticles that the ketone group is more readily hydrogenated than the aromatic alcohol[230]. It must be easier for H* to insert into the aldehyde group on the adsorbed benzaldehyde than into the aromatic ring of the adsorbed phenol.

Within the mechanism presented, higher hydrogenation rate constants for benzaldehyde than for phenol can lead to lower coverage of the former, possibly explaining both the lower coverage and the higher order for benzaldehyde than for phenol on Pt and Rh. However, the simple kinetic model (Equation 7-5) assumes that the organic reactant coverages are determined only by their competitive adsorption/desorption equilibria, and not significantly affected by their

removal rates by the reaction. Within Equation 7-5, the lower benzaldehyde coverage and consequently its higher order compared to phenol can only result from a lower adsorption constant K_A of benzaldehyde than of phenol.

The reaction model with moderate K_A matches the behavior of Pd ECH and TCH of benzaldehyde (Table 7-2). The hydrogen coverage (θ_H) is low, and there is no dependence of the rate on the concentration of benzaldehyde. However, as the $K_H C_H$ increases (either by increasing hydrogen pressure for TCH or increasing electrochemical potential for ECH), the rate increases and θ_H also increases. The ECH and TCH of phenol over Rh, as well as TCH of benzaldehyde on all three metals also are in this same regime, where the reaction is zero-order in the organic reactant. For all of the systems in Table 7-2 for which the orders in [organic] was measured both for TCH and ECH, the orders were either the same, or more positive for ECH than TCH. This occurs because $K_H C_H$ is higher in ECH than in TCH, due to the more negative applied potential in ECH (< 0 V versus RHE) than effectively present in TCH conditions (0 V versus RHE open-circuit potential at 1 bar H_2), leading to higher coverage of H on the surface. According to the rate law in our model (Equation 7-5), the higher $K_H C_H$ is, the higher C_A (or $K_A C_A$) must be to achieve rollover in rate versus C_A. This could be amplified by the fact that K_A generally decreases with H* coverage for many organics on platinum group metals, which is not explicitly incorporated in our model in Equation 7-5[231–234].

By our reaction model (Figure 7-6a), under conditions where the reaction is positive order in A, the rate would increase less with an increase in $K_H C_H$ (compared to conditions that are zero-order in A). This difference is observed for ECH of benzaldehyde between Pt/Rh (first order in benzaldehyde) and Pd (zero order in benzaldehyde), where the rate of benzaldehyde ECH over Pd is comparable to Pt at low overvoltages (-0.6 V versus Ag/AgCl), but double that

of Pt at higher overvoltages, or higher $K_H C_H$ (-0.9 V versus Ag/AgCl), as shown in Figure 7-1d. This shows that Pd's rate has a stronger dependence on $K_H C_H$ than Pt or Rh under benzaldehyde ECH conditions.

Although Pd under benzaldehyde ECH conditions operates at the same C_H (pH and applied potential) as Pt and Rh, θ_H is lower on Pd, either due to the fact that H* is removed faster by the faster reaction with benzaldehyde or due to a weaker K_H, or larger K_A, for Pd than Pt and Rh. As we discuss above, according to Equation 7-5 only different K_A values could cause these changes in coverage, as the K_H values should be quite similar for these metals. Because of the lower θ_H (and corresponding higher θ_A) on Pd compared to Pt and Rh, there is a zero-order dependence on [A] (benzaldehyde) for Pd, but first-order for Pt and Rh. Solution calorimetry also supports stronger benzaldehyde adsorption (larger K_A) on Pd than on Pt or Rh[120].

The positive order in phenol for TCH at low phenol concentrations and negative order in phenol at high concentrations (Figure 7-2) can also be matched by the same reaction model of Figure 7-6b. At moderate K_A, as C_A is increased (in this case A refers to phenol), the rate goes through a maximum, where the order in A transitions from first order to negative order (Figure 7-6b). During the transition, the hydrogen coverage will begin to decrease, but will not approach zero until very high concentrations of C_A. As we discuss above, the presence of 20 mM phenol does not decrease the HER current on Pd (compared to Pd without any organic), consistent with the observation that at 20 mM phenol, the phenol concentration is too low to significantly reduce the hydrogen coverage on Pd (HER activity being related to the hydrogen coverage).

7.4.3 Activation Energy Differences

The 7 kJ/mol lower apparent activation energy for benzaldehyde in ECH compared to TCH on all catalysts (Table 7-2) may be understood within this same kinetic model and Equation

7-5. We show next that this can be expected due to the increase in H coverage brought on by the higher H chemical potential (i.e. driving force to make H*) in ECH than in TCH. Under conditions where $K_A C_A >> 1 + K_H C_H$ (corresponding to very high organic coverage and low hydrogen coverage), Equation 7-5 simplifies to:

$$r_{LH,c} \approx k_{LH,c} \frac{K_H C_H}{K_A C_A} \tag{7-6}$$

The observed apparent activation barrier for these conditions would then be

$E_{app} = E_{a,LH,c} + \Delta H_H - \Delta H_A$, where $k_{LH,c} = A_{LH,c} \cdot exp[E_{a,LH,c}/RT]$, and ΔH_i is the standard enthalpy of adsorption of species *i*, always a negative value. If ΔH_A is larger in magnitude than ΔH_H, this could result in an apparent activation energy higher than the true activation barrier for the LH step. In contrast, if $K_H C_H$ was much higher, such that $K_H C_H >> 1 + K_A C_A$ (corresponding to very high hydrogen coverage and low organic coverage), Equation 7-5 simplifies to:

$$r_{LH,c} \approx k_{LH,c} \frac{K_A C_A}{K_H C_H} \tag{7-7}$$

In this case, the apparent activation barrier would be artificially lower than the true activation barrier instead of higher. Even though the data in Tables 7-1 and 7-2 were measured at conditions where the coverages do not approach the limiting values required to get Equations 7-6 and 7-7, the qualitative difference between Equations 7-6 versus 7-7 is still to be expected. Thus, the lower apparent activation energy observed for ECH of benzaldehyde than TCH in Table 7-2 is expected due to the higher $K_H C_H$ at the negative applied potentials used in ECH. (We note again here that we use $K_H C_H$ to generalize to both TCH and ECH, and ignore the role of applied potential beyond its influence on K_H discussed in the SI, which is mainly associated with the

Nernst equation.) Additional effects related to the observations that higher H coverages weaken organic adsorption may also play a role here[232–234].

Under limited conditions, the rate law in Equation 7-5 may be approximated with a power-law type expression which explicitly includes the reaction orders in reactant concentrations, α and β:

$$r_{LH,c} = k_{LH,c}\frac{K_A C_A K_H C_H}{(1 + K_A C_A + K_H C_H)^2} \approx k_{LH,c}(K_A C_A)^{\alpha}(K_H C_H)^{\beta} \quad (7\text{-}8)$$

The far right-hand side of this equation is an approximation that will only have constant values of α and β under small ranges of concentrations. For example, this form matches Equation 7-6 when α = -1 and β = 1, and matches Equation 7-7 when α = 1 and β = -1. If we consider the observed reaction orders for benzaldehyde TCH and ECH on Pt and Rh (Table 7-2), we see that for TCH (where the reaction order in benzaldehyde, α, is zero):

$$r_{LH,c} \approx k_{LH,c}(K_A C_A)^0(K_H C_H)^{\beta_{TCH}} \quad (7\text{-}9)$$

where $E_{app,TCH} = E_{a,LH,c} + \beta_{TCH}\Delta H_H$, and $\beta_{TCH} > 0$, $\Delta H_H < 0$.

For ECH, where there is a reaction order in benzaldehyde of one for Pt and Rh:

$$r_{LH,c} \approx k_{LH,c}(K_A C_A)^{\alpha_{ECH}}(K_H C_H)^{\beta_{ECH}} \quad (7\text{-}10)$$

where now $E_{app,ECH} = E_{a,LH,c} + \beta_{ECH}\Delta H_H + \alpha_{ECH}\Delta H_A$, $\beta_{ECH} > 0$, $\Delta H_H < 0$, $\alpha_{ECH} \approx 1$, and $\Delta H_A < 0$. Subtracting the above equations for E_{app} gives:

$$E_{app,TCH} - E_{app,ECH} = (\beta_{TCH} - \beta_{ECH})\Delta H_H - \alpha_{ECH}\Delta H_A \quad (7\text{-}11)$$

For the molecules and metals studied here, it appears that β is close to unity for both TCH and ECH at the conditions of Tables 7-1 and 7-2, so that the first term on the right approaches zero. In this case, $E_{app,TCH} - E_{app,ECH} > 0$ (remembering that ΔH_A is negative), or equivalently, $E_{app,TCH} > E_{app,ECH}$, thus, explaining the lower apparent barrier for ECH than TCH seen for any given molecule on any given metal seen in Table 7-2.

The earlier proposal[203] of an Eley-Rideal mechanism for ECH of benzaldehyde on Pd was based on absence of a negative reaction order with respect to benzaldehyde concentrations at the concentrations studied. However, the range of benzaldehyde concentrations studied was small (15–25 mM) and as Figures 7-2 and 7-6 show, the rate can remain relatively constant over such a small range of concentrations. Future work to definitively prove the mechanism for aqueous-phase benzaldehyde ECH on Pd is still needed, but the Langmuir-Hinshelwood mechanism we propose in this work can describe the kinetic data under the concentrations tested.

Our results show that Pt(111)-like sites are more active than Pt step and (110)/(100)-like sites in both phenol and benzaldehyde hydrogenation. This conclusion is based both on the earlier observation that the rates per unit area are slower on smaller Pt nanoparticles[117], and our kinetic modelling of concentration effects on rates here, which require adsorption equilibrium constants appropriate for (111) sites of Pt to fit the measured rates. This is the opposite from the observation for electrochemical hydrogenation of acetone in aqueous solution, where the Pt (110) step sites are most active, and the (111) and (100) facets are inactive due to too weak adsorption of acetone[235,236]. We attribute this marked difference between hydrogenation of acetone versus aromatics (phenol and benzaldehyde) to the much stronger binding of the aromatic molecules to Pt(111) than acetone. Acetone has a desorption temperature of ~190 K from Pt(111) in UHV, which corresponds to an adsorption energy of only ~50 kJ/mol[237]. Aromatic molecules (phenol and benzene) have much higher heats of adsorption (200 to 140 kJ/mol, depending on the coverage)[34,161]. Using these values in our recent bond-additivity model for the effect of solvents on adsorption energies[44,123] indicates that it would be *endothermic* to adsorb aqueous acetone on Pt(111) in aqueous phase (due to the failure of acetone to compete effectively with liquid water for Pt sites), whereas aqueous phenol adsorption is downhill by 21

kJ/mol (see above). Thus, while the weaker binding (111) facets may be more active for hydrogenation of these very strongly binding aromatics because they do not get covered too completely by adsorbed organics (leaving sites needed for H* adsorption), these facets may bind acetone so weakly that the coverage of adsorbed acetone is far too low to give significant rates. This explanation is consistent with the type of Langmuir-Hinshelwood model we proposed above also being applicable to acetone hydrogenation. Indeed, that model offers an excellent explanation for the reversed facet dependence observed for acetone versus aromatic hydrogenation rates.

7.5 Conclusions

The dependences of the reaction rates on reactant concentrations and temperature for all cases of both ECH and TCH for benzaldehyde and phenol on Pt/C, Pd/C, and Rh/C in aqueous-phase can be described successfully by a Langmuir-Hinshelwood model where the rate-determining step is the addition of an adsorbed H from the surface to the molecularly-adsorbed organic molecule, which competes for sites with H. The rate changes from being nearly first-order in organic concentration to strongly negative order as the organic concentration increases, for phenol, due to this competitive adsorption with H*. Because of the much lower solubility of benzaldehyde in water, this same range in concentration cannot be spanned. For Pt/C, the adsorption equilibrium constants for the organic required to fit the rates with this model are consistent with independent measurements of those equilibrium constants on Pt(111)-like sites (but not other facets), suggesting these are the most active sites. The increase in ECH activity with more negative (cathodic) potential is attributed to the corresponding increase in surface hydrogen coverage. The apparent activation energy decreases in going from TCH to ECH

conditions, attributed to the higher H* coverage which results from the applied potential in ECH. The high benzaldehyde adsorption constant on Pd (perhaps aided by its high intrinsic rate constant for benzaldehyde hydrogenation) causes the steady-state hydrogen coverage to be low, resulting in a high Faradaic efficiency towards benzaldehyde ECH over H_2 evolution. Pt and Rh have lower Faradaic efficiencies, and also higher orders in benzaldehyde for ECH, than Pd due to the lower benzaldehyde coverages on Pt and Rh. The high reaction rate of Pd towards benzaldehyde is not due to formation of β-PdH_x, which does not form under these conditions (unlike what has been found for CO_2 reduction). Adsorbed benzaldehyde is more reactive with H* (i.e., has a higher intrinsic rate constant for H addition) than is adsorbed phenol on all three metals.

7.6 Supporting Information

7.6.1 Calculating iR-corrected Overpotential and 'Equivalent' Hydrogen Pressure

The reference electrode is calibrated by comparing to a platinum wire in solution with 1 bar H_2 (defining 0 V vs. RHE at the given pH at open circuit voltage). The uncompensated resistance (due to solution resistance, contact resistances and other effects) is calculated using impedance spectroscopy, then compensated at 85% during the run (not 100% due to issues in stability above 85%). The final 15% of the resistance is compensated afterwards by the following equation to achieve the corrected voltage (V_{corr}).

$$V_{corr} = V_{85\%\,comp} - i_{meas} \times 0.15 \times R_u \qquad \text{(7-S1)}$$

where i_{meas} is the current measured during the experiment, and R_u is the measured uncompensated resistance. When both of these compensations are done, it gives a iR compensated voltage (V_{corr} vs. RHE), which minimize the contribution from iR drop and associated issues due to reference electrode distance, etc.

This compensated voltage vs. RHE can be compared to an 'equivalent' H_2 pressure. This pressure is the hydrogen pressure that would thermodynamically be achieved at equilibrium at the same applied potential, assuming no change in pH, calculated with the Nernst equation. Since there is a current flowing during the run, by definition this is not the true hydrogen pressure in the system (since the Nernst equation refers to an equilibrium system).

Some of the previously reported rates of ECH of benzaldehyde and phenol on Pd, Pt and Rh may have used approximations for this voltage,[115,201,204] but it is unclear if they calibrated the reference electrode properly, or corrected for the uncompensated resistance. For our measurements here, we have corrected for this, and so the true voltage is reported.

Sample calculations converting applied compensated potential to 'equivalent H_2 pressure':

Using the method above to determine an iR-compensated potential against a calibrated reference electrode (at electrolyte pH and 1 bar H_2), two sample runs yielded applied potentials of -0.10 V vs. RHE and -0.11 V vs. RHE.

The Nernst equation can be used to calculate the equilibrium pressure of H_2 that would thermodynamically be achieved at a given compensated potential vs. SHE (*V*):

$$V = -\frac{2.303RT}{F}pH - \frac{RT}{2F}\ln\frac{p_{H_2}}{p^0} \tag{7-S2}$$

R is the ideal gas constant, *T* is the temperature, *F* is Faraday's constant, p_{H_2} is the hydrogen pressure and p^0 is the standard pressure (1 bar). We use here compensated potentials vs. RHE (*E*) instead, which removes the effect of pH from this equation:

$$E = -\frac{RT}{2F}\ln\frac{p_{H_2}}{p^0}\,. \tag{7-S3}$$

At *E* = -100 mV:

$$-0.1V = \frac{-8.314\,\frac{J}{molK} * 300K}{2 * 96485\ C/mol}\ln\frac{p_{H_2}}{p^0} \tag{7-S4}$$

$$\frac{-0.1V}{-0.012925\ V} = \ln\frac{p_{H_2}}{p^0} \tag{7-S5}$$

$$p^0 e^{\frac{-0.1V}{-0.012925\ V}} = p_{H_2} \tag{7-S6}$$

$$p_{H_2} = 2291\ bar\ at - 100\ mV.$$

Similarly at *E* = -110 mV:

$$p_{H_2} = 4966\ bar\ at - 110\ mV \quad \text{(7-S7)}$$

These pressures calculated from Equation 7-S3 are not actually achieved, due to the system not reaching equilibrium during ECH. However, they can be considered as 'equivalent H_2 pressures' in that they quantitatively capture the thermodynamic effect of applying a more negative potential on the stability of H^+_{aq} (plus an electron on the metal) that results in the rapidly increasing equilibrium constant (K_H) for H adsorption via $H^+_{aq} + e^- \rightarrow H^*$ discussed in the text. That is, for any given applied potential (E) during ECH at constant temperature and pH, the product $K_H C_H$ discussed in the text equals, to a first approximation, $K_H C_H$ at 0 V versus RHE multiplied by this 'equivalent pressure' (divided by p^0). This simple Nernstian correction for the stability H^+_{aq} (plus an electron on the metal) captures the dominant change in K_H with applied potential. There is a smaller effect due to the change in stability of H* with applied potential. We have shown that H* gets more stable by ~0.8 kJ/mol (or 8.3 mV) per increase in pH by 1 at fixed voltage vs. RHE, which we attributed to the corresponding 59 mV decrease in potential vs. SHE at fixed chemical potential of H^+_{aq}.[114] This 8.3 mV stabilization is only 14% of the direct Nernstian correction of Equation 7-S3 above for this 59 mV decrease in potential. It should thus add another ~14% to the pure Nernstian increase in K_H that results from the effect of more negative applied potential on the stability of H^+_{aq} (plus an electron on the metal) relative to H*.

7.6.2 Benzaldehyde ECH on Pd/C

The conversion (based on benzyl alcohol product formed) versus time for ECH of benzaldehyde on Pd/C is shown in Figure 7-S2. The slope of this line was used to determine the turnover frequencies plotted in Figure 7-2. Although the solution is purged by nitrogen during the measurements, a pre-conditioning step of the Pd/C electrode consists of reduction (in the

absence of benzaldehyde) which also generates H_2 gas and would form absorbed H in the Pd lattice. After addition of benzaldehyde, the solution is purged with nitrogen, however, small amounts of thermocatalytic conversion (due to residual H_2) occur before the potential is applied for ECH, as seen at time zero in Figure 7-S2.

7.6.3 XANES Results for Pd/C

The electrochemical formation of the β-PdH_x is determined from the XANES peak position for the Pd K-edge. It is formed by going to more cathodic potentials, and is reversible (with some hysteresis) by reversing the potential (Figure 7-S3a). In addition to this change in Pd XANES peak position with applied potential, the unnormalized X-ray transmission of the electrolyte changes with applied potential (Figure 7-S3b). (The X-ray absorption coefficient for the sample, μ(E), varies as the negative log of the transmission (I_T/I_0).) The increase in transmission with more cathodic potential is attributed to the amount of dissolved H_2 in solution and H_2 gas bubbles in the beam path (due to generation of H_2 electrochemically). For water saturated with H_2 gas, the decrease in density is 0.002%, corresponding to an increase in transmission of 0.003%,[238,239] significantly lower than the observed increase here, indicating gas-phase H_2 may also be responsible for the increased transmission. As H_2 molecules are formed electrochemically at more negative potentials, the H_2 amount in the flowing electrolyte increases, thus increasing transmission (decreasing μ(E)), as seen in Figure 7-3b. This increase in transmission can be used to estimate the amount of H_2 formed electrochemically (Figure 7-S3b), and as expected the presence of benzaldehyde significantly reduces the transmission change at a given potential, due to the high current efficiency towards benzaldehyde hydrogenation over H_2 evolution. The charge during the scan is also shown in Figure 7-S3b, and compared to the

amount of charge require to convert the catalyst completely to a 1:1 ratio of Pd:H (based on catalyst mass).

7.6.4 Cyclic Voltammetry of Pd Foil with Phenol and Benzaldehyde

Cyclic voltammetry of Pd in aqueous electrolytes in the absence of organic molecules has previously been done on C-supported nanoparticles,[223,240,241] thin films,[242] and bulk foils.[240,243] Unlike Pt and Rh, which show peaks corresponding to hydrogen underpotential deposition (H_{upd}) for both nanoparticles/thin films and bulk materials such as wires or foils, for Pd the H_{upd} peaks are only distinguishable on C-supported nanoparticles (at 0.2-0.3 V vs. RHE depending on pH),[223,240,241] or thin films[242], but not on bulk (i.e. foil) Pd metal.[240,243] This is due to the bulk of nanoparticles quickly becoming saturated with H (formation of bulk hydride), as opposed to bulk foils, where H_{upd} and bulk hydride formation is indistinguishable.[240] Because Pt and Rh do not form bulk hydrides, H_{upd} can be detected even on bulk foils of Pt and Rh (but not Pd). For the 5 wt% Pd/C used in this study, the loading of Pd metal was too low to distinguish H_{upd} or hydride formation from the carbon support capacitance. For this reason, we instead used a Pd foil to look at the effects of benzaldehyde and phenol on hydride formation (including bulk and surface hydrogen). Although this does not allow direct probing of the surface hydrogen (H_{ad} or H*), the effect of benzaldehyde and phenol on the electrochemical formation of the hydride during cyclic voltammetry can give qualitative information about hydrogen coverage on Pd in the presence of these organic molecules by assuming the bulk hydride formation rate is proportional to hydrogen surface coverage, as expected.[215,216]

The cyclic voltammograms shown in Figure 7-S4a and 7-S4b for a Pd foil in acetate buffer with no organic present shows the formation of a Pd “hydride” (by integration of charge, at -0.4 V versus Ag/AgCl the foil has converted to $Pd_1H_{0.0015}$, which is ~100 times more H than a

monolayer of H on the Pd surface, but still of a stoichiometry corresponding to α-PdH_x). The equal charge in the cathodic and anodic scan indicate this current is a reversible reaction, and as the potential is positive to 0 V versus RHE, this cathodic and anodic current is completely attributed to the formation and reversal, respectively, of the Pd metal to the Pd hydride (although the distinction between surface and bulk hydride cannot be made). The addition of 20 mM phenol (Figure 7-S4a), inhibits the hydride current in both the cathodic and anodic scans. There is a slight increase in hydride formation current at low concentrations of phenol for unknown reasons, but site blocking by phenol is clearly seen above 1 mM (Figure 7-S4a). A similar increase at low concentrations was reported for addition of benzene to Pt(111).[244,245] At ≥5 mM benzene, however, the H_{upd} charge did decrease, due to benzene blocking sites.[245]

In Figure 7-S4b, benzaldehyde decreases the hydride current (and charge) at all concentrations, and significantly more than phenol at 20 mM (relevant to initial reaction conditions for ECH). Although the inhibition of the Pd hydride formation might either be because the organic blocks sites from forming a surface hydrogen (necessary as an intermediate for bulk hydride formation), or the organic reacts so fast with H* it consumes it before it can form the bulk hydride, because the magnitudes of the cathodic charge and anodic charge are equal for each scan, the reduction current must correspond to a reversible formation of hydride, not irreversible reaction of that hydrogen with the organic. Thus, the inhibition of the hydride by addition of phenol or benzaldehyde is mainly due to blocking of sites, rather than fast reaction with surface hydrogen, consistent with our kinetic model. Since benzaldehyde has a larger decrease in the hydride current than phenol, benzaldehyde must bind more strongly and thus pack more tightly at high coverage than phenol on Pd. These results corroborate the XANES (Figure 7-4) and EXAFS (Figure 7-5) results that indicate benzaldehyde binds stronger to Pd

than phenol and maintains a low hydrogen coverage on the surface of Pd. From the measurement in Figure 7-S4a, at 20 mM phenol there is roughly 50% of the charge from H stripping (from bulk and surface) than with no phenol present, perhaps implying 50% coverage. This is a slightly lower concentration than the predicted ~90 mM for 50% coverage of phenol based on the fit from Figure 7-2a, but in a similar order of magnitude.

7.6.5 EXAFS Spectra for Pd/C during ECH

The difference in the peak and trough at 2.4 and 2.6 Å (uncorrected) between the Pd foil and the Pd/C catalyst under applied potential in Figure 7-S5 is related to the expansion in lattice parameter (Pd-Pd distance) as H enters the Pd lattice.[246–248] The Pd-Pd expansion is related to the [H]/[Pd] ratio both for bulk Pd[221] and for Pd nanoparticles.[210,214] The expansion is minor if benzaldehyde is present, and is more significant at -0.60 V than -0.55 V in acetate buffer only. There is also a change in the peak at 1.8 Å with the addition of benzaldehyde, which may be due to Pd-C interactions.

Figure 7-S6 shows the comparison of the average Pd-Pd distance from EXAFS of a 2.6 nm Pd/C catalyst as a function of the H to Pd ratio from ref. [210], compared to the prediction from Equation 7-1. Differences in the data may be from the influence of the shell of Pd, as discussed in ref. [210,220]. Because of the difference in particle sizes and conditions during the EXAFS measurements, the data from ref. [210] is not directly used to calculate the [H]/[Pd] ratio for this work, and instead Equation 7-1 is used to estimate [H]/[Pd].

The data in Figure 7-5 for the [H]/[Pd] ratio from EXAFS for the Pd/C in different electrolytes is plotted against the steady-state current (during the EXAFS measurement) in Figure 7-S7. The correlation between current (i.e., TOF) and [H]/[Pd] in the presence of benzaldehyde is evident from both Figure 7-5 and Figure 7-S7. There was negligible decrease in

the steady-state current with time for these potentials (±5% variation over the 15 minutes measurements). The only exception was at -1.2 V versus Ag/AgCl, where the reduction current did decrease ~20% over 15 minutes. However, as mentioned in the main text, the current required to completely convert the molar flow rate of benzaldehyde to the Pd/C was approximately 7 mA, and at -1.2 V, as seen in Figure 7-S7, the average reduction current of 7 mA corresponds to a complete conversion of the benzaldehyde fed into the electrochemical cell. Therefore, we attribute the decrease in current with time for -1.2 V to insufficient feed of benzaldehyde to keep up the initially high conversion rates (which are enabled until the benzaldehyde concentration in the cell reaches steady state). The lower reaction rates/current at the less negative potentials are insufficient to completely convert the benzaldehyde, and thus there is no decrease in activity with time.

7.6.6 Electrochemical Impedance Spectroscopy (EIS)

Electrochemical Impedance Spectroscopy (EIS) was performed in a rotating disk electrode (RDE) setup. Polycrystalline Pt and Pd disks 5 mm in diameter (Pine) were cleaned before use by sonication in iso-propanol and Millipore water. The glass RDE cell was initially cleaned in acid and base baths and boiled in Millipore water, and subsequently sonicated in iso-propanol to remove any organics followed by drying then several series of further sonication with Millipore water between measurements. The Ag/AgCl reference electrode was calibrated to the reversible hydrogen electrode (RHE) in the same electrolyte, and used a double junction to minimize potential contamination. The Pt counter electrode was contained in a glass fritted compartment for isolation from the working electrode. The electrolyte was 100 mM acetic acid (Sigma Aldrich, 99.995%) and 100 mM sodium acetate (99.999%) (pH 5), purged with N_2 gas.

The organics were phenol (Sigma Aldrich, unstabilized >99%) and benzaldehyde (Sigma Aldrich >99%).

Disks were rotated constantly at 1600 rpm and polarized with a Bio-Logic SP200 potentiostat. Disks were cleaned by cycling between -0.3 and 0.9 V versus Ag/AgCl. Prior to impedance measurements, the electrodes were cycled from -0.4 to 0.6 V versus Ag/AgCl. Potentiostatic EIS was carried out with an AC amplitude of 10 mV, after holding for 30 seconds at the specified DC potential. Spectra (Figure 7-S8a and 7-S8b) were fit with Z-fit software (Bio-Logic) using the equivalent circuit in Figure 7-S8c (Armstrong circuit).

The capacitance C1 is lower for Pt with 20 mM organics present than with only acetate buffer (Table 7-S1). Based on the reported relation between double layer capacitance and organic coverage due to the adsorbed organic acting as a 'blanket',[224] the lower capacitance seen for benzaldehyde and phenol implies organics are still adsorbed on the Pt surface, even at -0.1 V versus RHE. Because of the formation of PdH_x at these potentials for the Pd disk, it is more challenging to interpret the results for capacitance in the presence of organics. However, the charge transfer resistance R3 for Pd is lower for Pd in the presence of benzaldehyde than in the presence of phenol (Table 7-S1), corroborating the higher intrinsic rate constant for benzaldehyde inferred from the rate measurements.

7.6.7 Rate Equations for Langmuir-Hinshelwood Mechanism

The general derivations of reaction models for surface reactions with multiple elementary steps can be found in many textbooks on catalysis, for example in Davis and Davis.[225] Here we reproduce derivations of some of these for the specific rate-determining step here, for completeness.

Elementary steps and rate equations

As in the main text, *A* is the organic molecule and *H* refers to hydrogen, either H^+_{aq} (in ECH) or $H_{2,aq}$ (in TCH). Let us assume reversible adsorption of *A* (organic) and *H* (hydrogen) onto sites on the catalyst surface, designated here as being of two possibly different types (* and ^), with these adsorption reactions all coming to rapid equilibrium:

$$A + * \rightleftharpoons A* \tag{7-S8}$$

$$H + * \rightleftharpoons H* \tag{7-S9}$$

and/or

$$H + \text{^} \leftrightarrow H\text{^} \tag{7-S10}$$

A adsorbs onto a certain site either competitively with *H* (competing for * sites) or non-competitively with *H* (if *H* adsorbs onto a separate type of site, ^). The equilibrium of *A* adsorbing on the surface is given by equilibrium constant K_A, and the equilibrium constant for *H* is K_H. For simplicity, we neglect here the second-order nature of $H_{2,aq}$ adsorption/desorption (so that the rate equations involving H^+_{aq} and $H_{2,aq}$ look the same below), but explain below a simple way to mathematically correct for this.

Let us also assume that the rate-determining step is a surface reaction between the two adsorbed species:

$$A* + H* \xrightarrow{k_{LH,c}} Product + 2* \tag{7-S11}$$

and/or

$$A* + H\text{^} \xrightarrow{k_{LH,nc}} Product + * + \text{^} \tag{7-S12}$$

where $k_{LH,c}$ is the rate constant for the case where there is competitive adsorption of *A* and *H*, and $k_{LH,nc}$ is the rate constant for the case where there is non-competitive adsorption. The rate equation is:

$$r_{LH} = k_{LH}\theta_A\theta_H \tag{7-S13}$$

where θ_A is the coverage of *A* and θ_H is the coverage of *H**. Here we are assuming it does not matter which site *H* is adsorbed onto.

Coverage equations for competitive and non-competitive adsorption

For competitive adsorption:

$$K_A = \frac{\theta_A}{C_A\theta_*} \tag{7-S14}$$

$$K_H = \frac{\theta_H}{C_H\theta_*} \tag{7-S15}$$

We neglected here the second-order nature of $H_{2,aq}$ adsorption, but it is well known that an identical equation results if we treated it as second-order, provided we consider C_H here as an "effective first-order concentration" actually given by $C_H = (C_{H2})^{1/2}$ in TCH, and $K_H = (K_{H2})^{1/2}$. C_{H2} is assumed to equal P_{H2} in equilibrium with the solution.

Site balance requires that:

$$\theta_A + \theta_H + \theta_* = 1 \tag{7-S16}$$

Using the last equation to solve for θ_* and substituting for it in the first gives:

$$K_A = \frac{\theta_A}{C_A(1 - \theta_A - \theta_H)} \tag{7-S17}$$

which can be rearranged to give:

$$\theta_A = \frac{K_A C_A (1 - \theta_H)}{(1 + C_A K_A)} \tag{7-S18}$$

Similarly:

$$K_H = \frac{\theta_H}{C_H (1 - \theta_A - \theta_H)} \tag{7-S19}$$

which can be combined with the above to give:

$$\theta_H = \frac{K_H C_H}{(1 + K_A C_A + K_H C_H)} \tag{7-S20}$$

These can be combined to give:

$$\theta_A = \frac{K_A C_A}{1 + K_A C_A + K_H C_H} \tag{7-S21}$$

Rate equations using solutions for coverages

For Langmuir-Hinshelwood with competitive adsorption, these coverage expressions can be substituted into the rate equation above to give:

$$r_{LH,c} = k_{LH,c} \frac{K_A C_A}{(1 + K_A C_A + K_H C_H)} \frac{K_H C_H}{(1 + K_A C_A + K_H C_H)} \tag{7-S22}$$

$$r_{LH,c} = k_{LH,c} \frac{K_A C_A K_H C_H}{(1 + K_A C_A + K_H C_H)^2} \tag{7-S23}$$

Similarly, for non-competitive adsorption, we have:

$$K_A = \frac{\theta_A}{C_A \theta_*} \tag{7-S24}$$

$$K_H = \frac{\theta_H}{C_H \theta_\wedge} \tag{7-S25}$$

$$1 = \theta_A + \theta_* \tag{7-S26}$$

$$1 = \theta_H + \theta_\wedge \tag{7-S27}$$

and:

$$K_A = \frac{\theta_A}{C_A(1-\theta_A)} \tag{7-S28}$$

$$\theta_A = \frac{K_A C_A}{(1+K_A C_A)} \tag{7-S29}$$

$$\theta_H = \frac{K_H C_H}{(1+K_H C_H)} \tag{7-S30}$$

The Langmuir-Hinshelwood rate with non-competitive adsorption is then:

$$r_{LH,nc} = k_{LH,nc}\theta_A\theta_H \tag{7-S31}$$

$$r_{LH,nc} = k_{LH,nc}\frac{K_A C_A K_H C_H}{(1+K_A C_A)(1+K_H C_H)} \tag{7-S32}$$

For values of C_A = 0.02, $k_{LH,c}$ = 4 s^{-1}, the reaction rate is plotted in Figure 7-S9 for different values of K_A for competitive (a-c) and non-competitive (d-f) adsorption. The 'order' can be determined by calculating:

$$\frac{d\ln Rate}{d\ln C_A} = Order\ in\ A \tag{7-S33}$$

The order in *A* is plotted on the second (right) vertical axis in Figure 7-S9.

In Figure 7-2, the negative order in phenol (*A*) observed for phenol TCH is only possible considering a competitive adsorption Langmuir-Hinshelwood model. Because this simple model is able to explain the observed kinetic data for TCH and ECH of phenol and benzaldehyde on the platinum group metals, without invoking additional reaction pathways (such as Eley-Rideal-like mechanisms), we assume that it is the dominant mechanism.

7.7 Figures

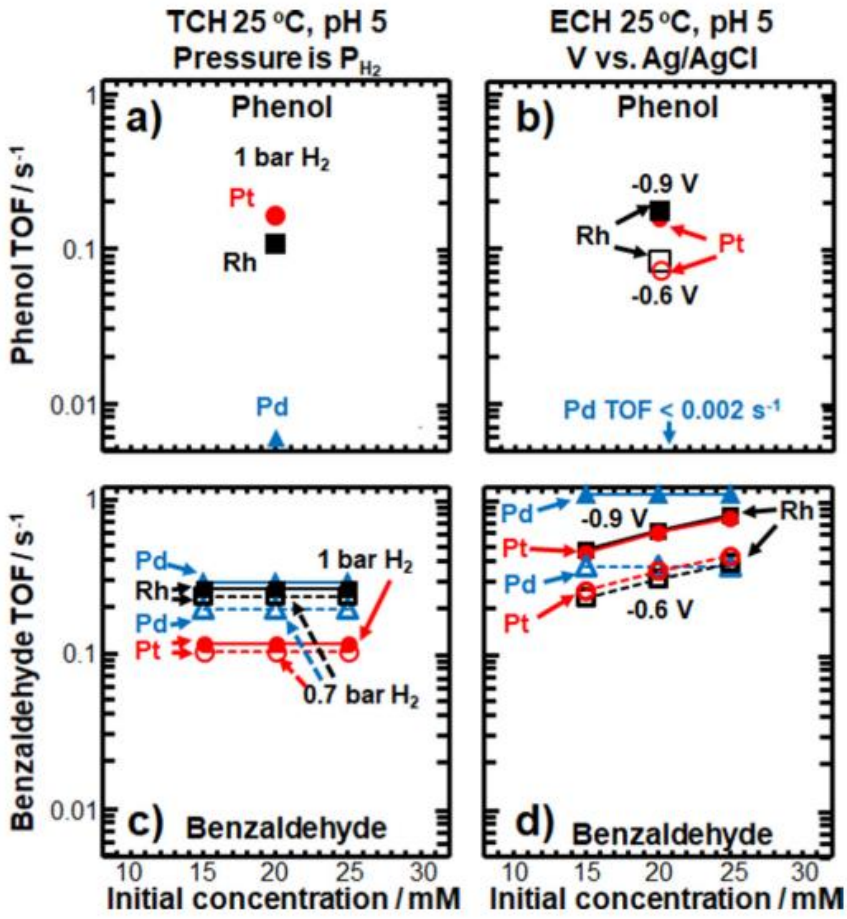

Figure 7-1. (a) Phenol thermal catalytic hydrogenation (TCH) rates for Pd and Pt (this work) and Rh at 1 bar H_2 at 25 °C as a function of phenol concentration. Full set of concentrations and TOFs for Pt and Pd TCH at 1 bar H_2 is shown in Figure 7-2. (b) Phenol electrocatalytic hydrogenation (ECH) rates for Pt and Rh at -0.9 V and -0.6 V versus Ag/AgCl at 25 °C and pH 5. (c) Benzaldehyde TCH rates for Pd, Pt and Rh at 1 bar and 0.7 bar H_2 [120]. (d) Benzaldehyde ECH rates for Pd, Pt and Rh at -0.9 V and -0.6 V versus Ag/AgCl[120]. The literature ECH rates were at voltages that were not compensated for solution resistance (see Supporting Information).

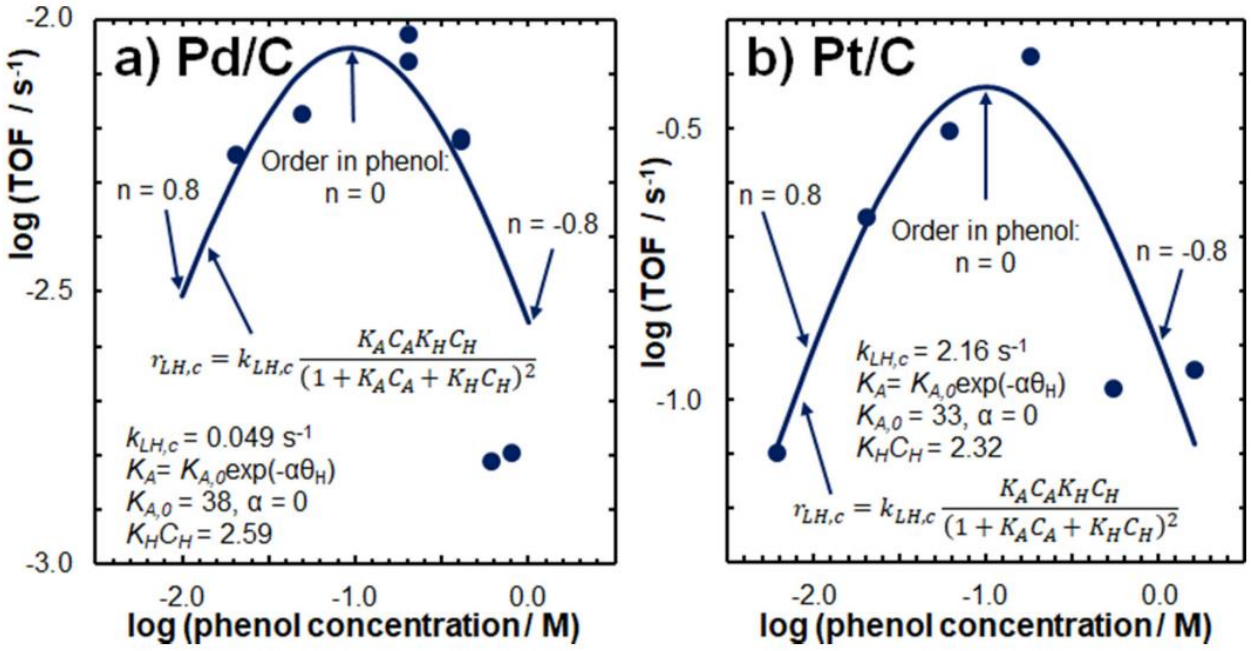

Figure 7-2. Effect of phenol concentration on the TOFs at 25 °C for phenol TCH on (a) Pd/C and (b) Pt/C. Fits based on a Langmuir-Hinshelwood mechanism with competitive adsorption (Equation 7-5) are shown by the solid lines. The points on the fit where the order, n, in phenol is 0.8, 0, and -0.8 are indicated. Concentrations of phenol where the order in phenol equaled to 0.8, 0, and -0.8 are indicated. TCH was conducted at 1 bar H_2 in water. We express both concentrations and equilibrium constants as unitless here, which is equivalent to treating concentrations as activities, i.e., normalized to the standard-state concentration. We take that standard-state concentration for the organics to be 1 M and for H_2 to be the equilibrium concentration at 1 bar H_2.

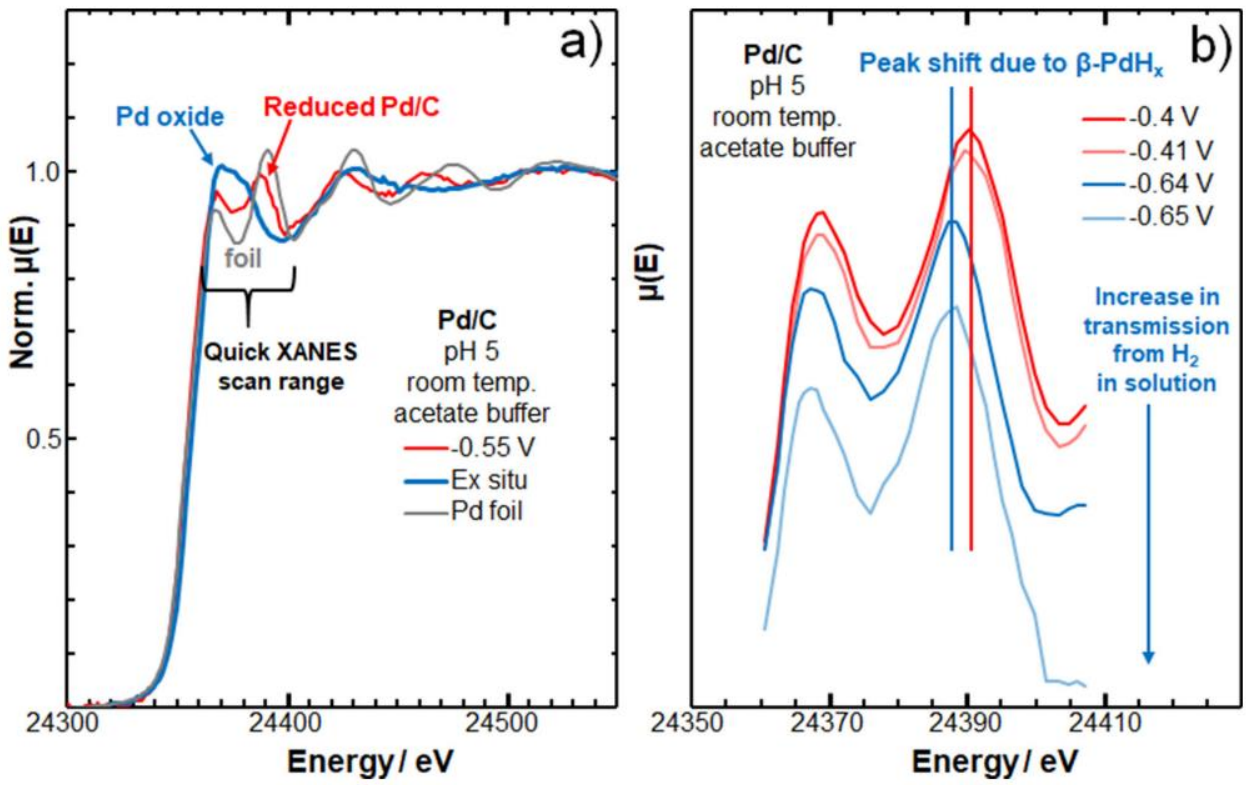

Figure 7-3. (a) X-ray absorption scan of Pd K-edge for a Pd/C sample as prepared on an electrode (partial Pd oxide), and after being reduced at -0.55 V versus Ag/AgCl in acetate buffer, compared to Pd foil. The shorter scan range in (b) is used to quickly detect formation of β-PdH_x as applied potential is varied. The shift in peak energy is due to formation of β-PdH_x. The decrease in μ(E) is due to H_2 formation increasing the X-ray transmission through the electrolyte.

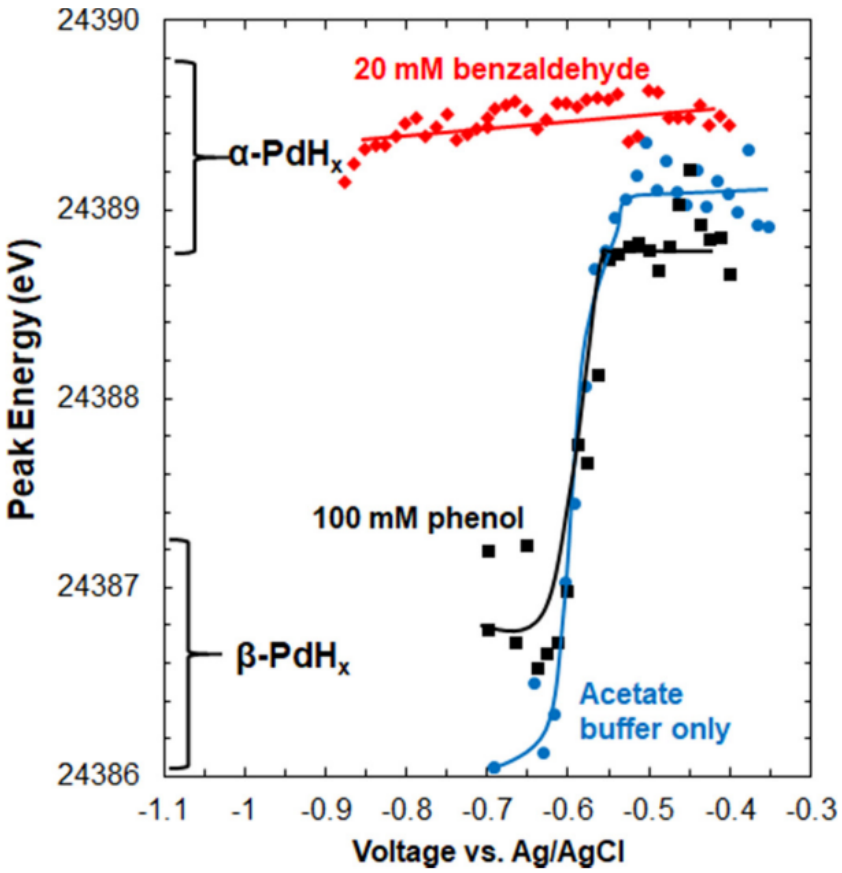

Figure 7-4. XANES Pd K-edge peak energy as a function of potential. (Examples of spectra used to determine peak energies are shown in Figure 7-3b.) Scan rate was 0.6 mV s^{-1}. Electrolytes were 100 mM acetic acid/100 mM sodium acetate (acetate buffer) with no organic, 100 mM phenol, or 20 mM benzaldehyde. Shift in the peak energy indicates a transition from either Pd metal or α-PdH_x to β-PdH_x. Catalyst is 5 wt% Pd/C. Reaction at room temperature.

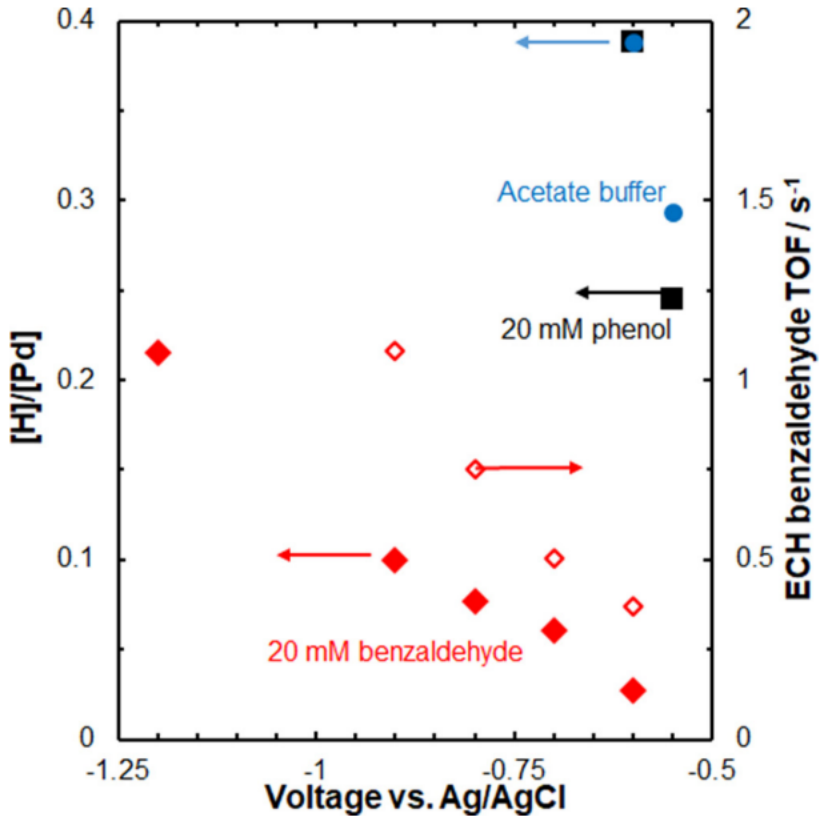

Figure 7-5. [H]/[Pd] concentration ratio in the Pd/C catalyst for different electrochemical conditions based on changes in the Pd-Pd distance from EXAFS using Equation 7-1. TOFs for ECH of benzaldehyde on Pd from ref.[120] are also included. (These are literature values, not TOFs measured during the EXAFS measurement.) The steady-state current measured during the spectroscopy measurements is plotted in Figure 7-S7.

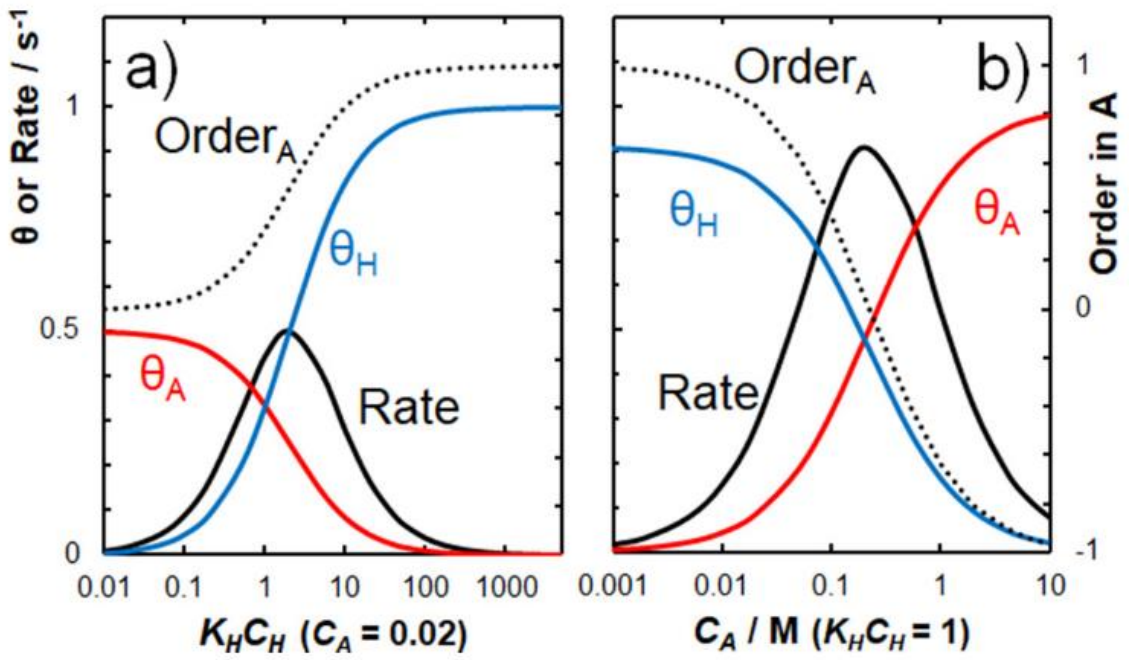

Figure 7-6. (a) Reaction rates ($r_{LH,c}$), coverages of *A* and *H* (θ_A, θ_H), and order in *A* as a function of K_HC_H for C_A = 0.02, based on the reaction model with competitive adsorption (i.e., Equation 7-5), with moderate adsorption strength (K_A = 50) and $k_{LH,c}$ =4 s^{-1}. (b) Reaction rates, coverages of *A* and *H*, and order in *A* as a function of C_A, as opposed to K_HC_H, for K_HC_H = 10 and this same competitive adsorption model and same equilibrium constants and rate constants. We express both concentrations and equilibrium constants as unitless here, which is equivalent to treating concentrations as activities, i.e., normalized to the standard-state concentration. We take that standard-state concentration for the organics to be 1 M and for H_2 to be the equilibrium concentration at 1 bar H_2 (or the square root of that for C_H, see Equation 7-S15 and related discussion in SI).

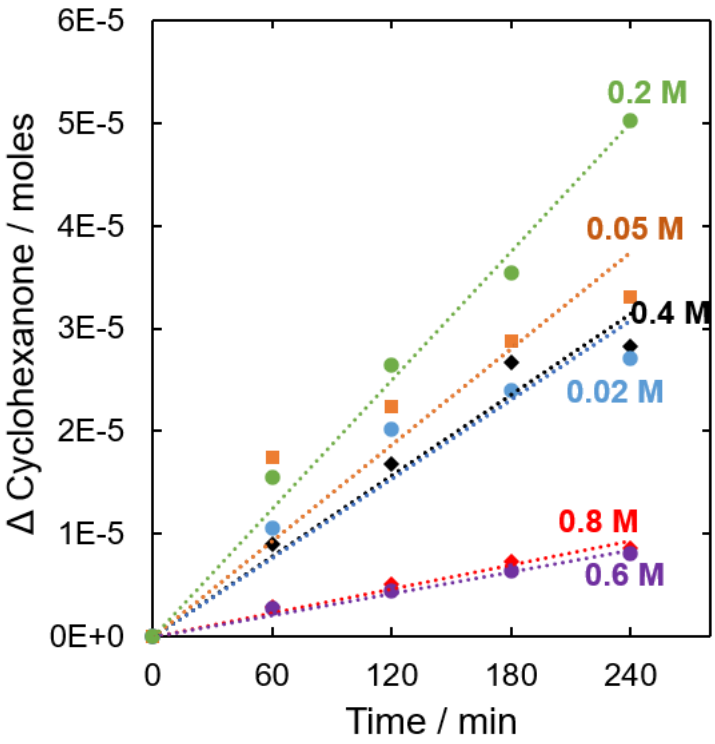

Figure 7-S1. Change in cyclohexanone amount (total volume of solution is 50 mL) with time for phenol TCH on Pd for different initial concentrations of phenol. Catalyst is 5 wt% Pd/C. Room temperature, 1 bar H_2. pH = 5.

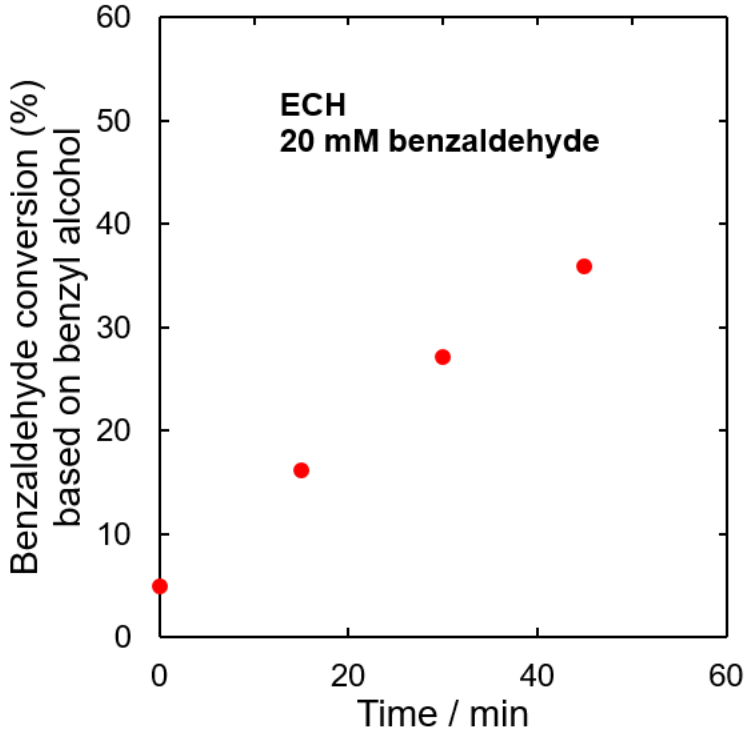

Figure 7-S2. ECH conversion rate of benzaldehyde to benzyl alcohol on 5 wt% Pd/C in electrocatalysis. These conversion values were calculated from product (benzyl alcohol) generated. iR-corrected potential range for measurements is -100 to -106 mV versus RHE. Room temperature and pH=5 in acetate buffer (100 mM of each acetic acid and sodium acetate).

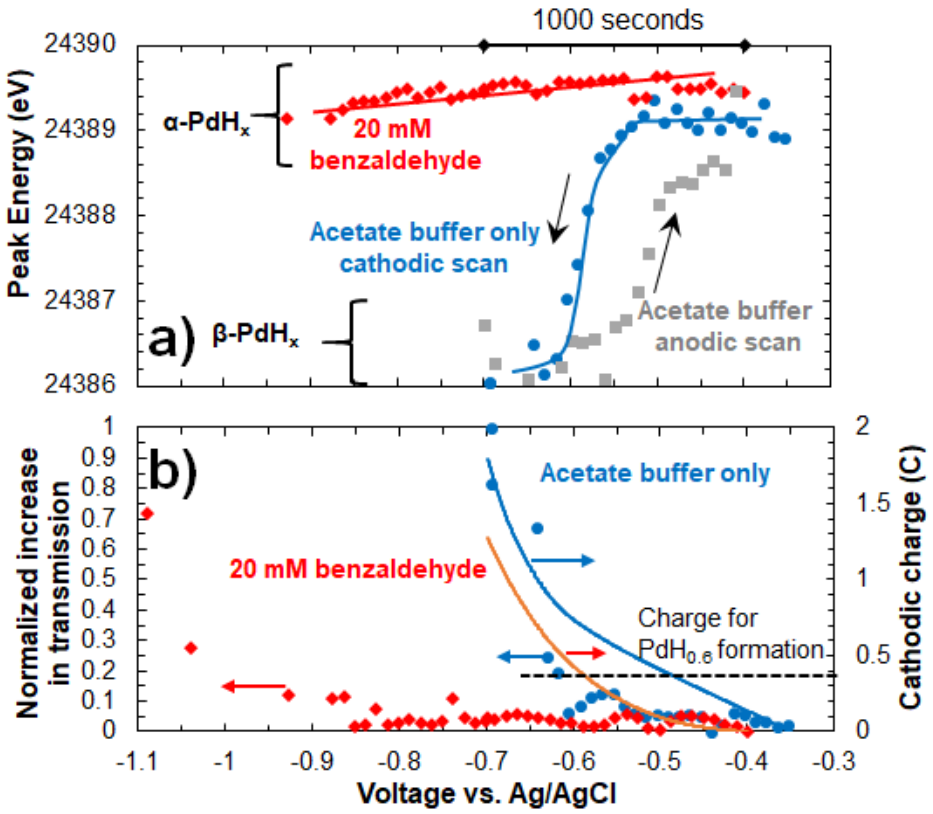

Figure 7-S3. (a) The XANES peak energy for the Pd K-edge as a function of applied potential in different electrolytes. The energies that are known to correspond to the β-PdH_x and α-PdH_x[211–213] are indicated. β-PdH_x is not formed in the presence of benzaldehyde. In acetate buffer the process is reversible (in the presence of phenol, β-PdH_x also forms reversibly). (b) The increase in X-ray transmission in XANES (points), attributed to H_2 in electrolyte as a function of applied potential. Also shown is the cumulative charge passed during cathodic sweep (solid lines) as a function of potential. The dashed line indicates the amount of charge to completely convert the Pd/C catalyst to a 1:0.6 ratio of Pd:H, based on catalyst mass (indicating that sufficient charge has passed to go to form the β-PdH_x, but instead the current is going towards benzaldehyde reduction or hydrogen evolution). Room temperature and pH 5.

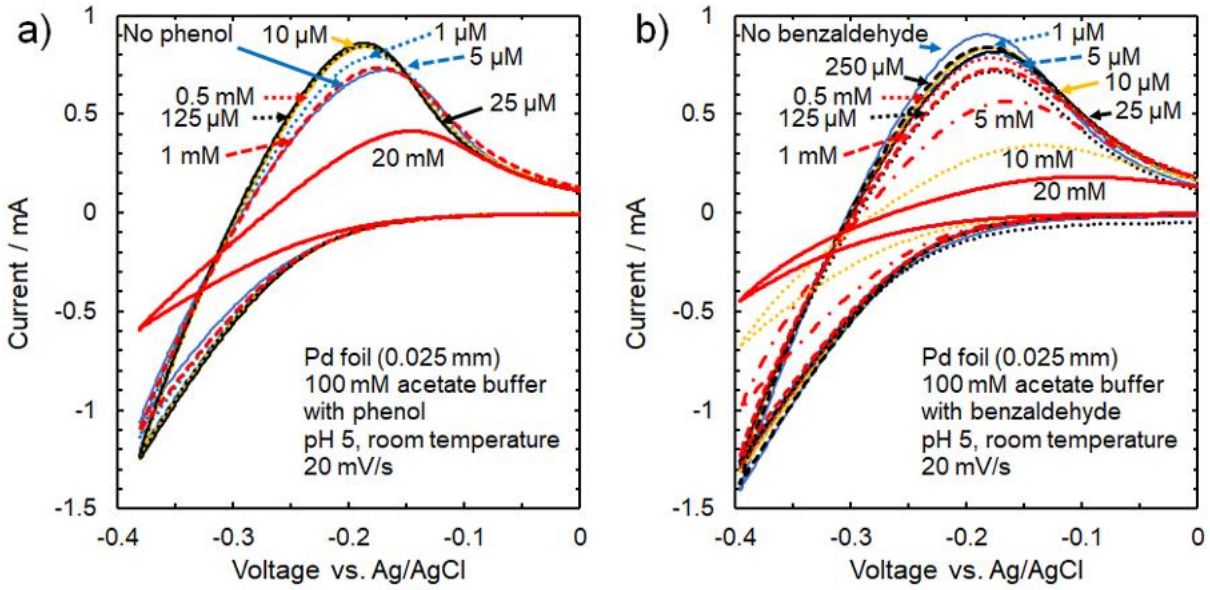

Figure 7-S4. Cyclic voltammograms of a 0.025 mm thick Pd foil in acetate buffer with different concentrations of organic. Voltage range corresponds to Pd hydride formation (but more positive than hydrogen evolution, 0 V versus RHE is -0.4 V versus Ag/AgCl here). (a) 0-20 mM phenol and (b) 0-20 mM benzaldehyde. Scan rate was 20 mV/s, pH 5 acetate buffer, room temperature.

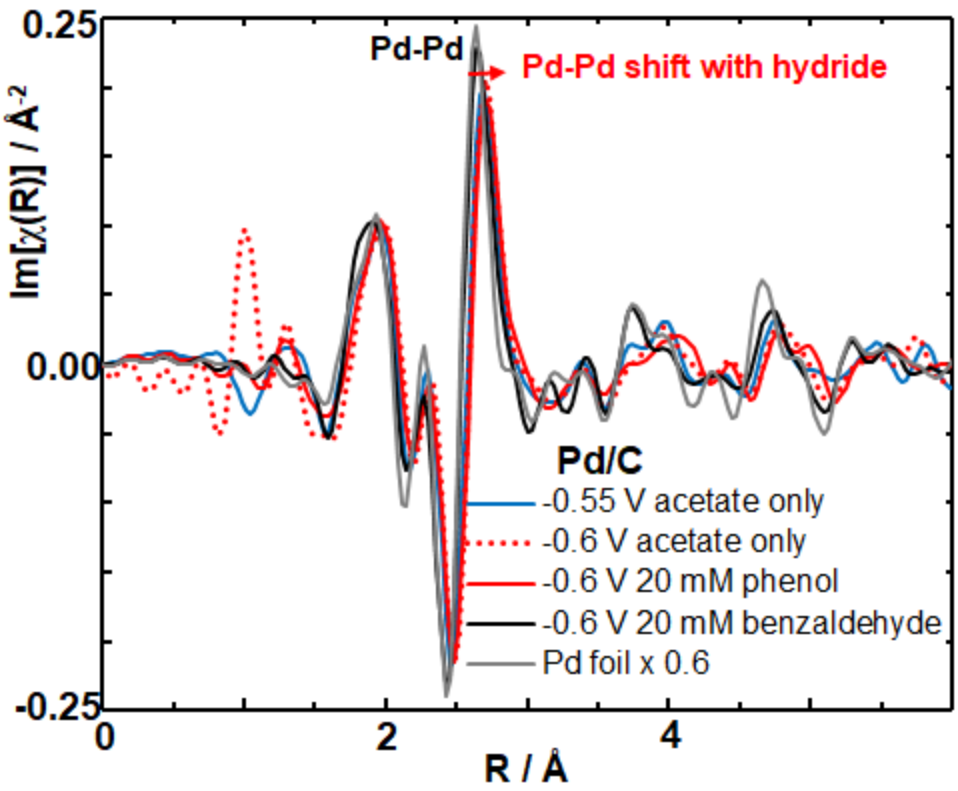

Figure 7-S5. EXAFS Pd K-edge Im[χ] plot for 5 wt% Pd/C after reduction and held at -0.55 V, -0.6 V in acetate buffer, at -0.6 V in acetate buffer with 20 mM phenol and 20 mM benzaldehyde. Clean Pd reference foil is included for comparison (scaled by 0.6).

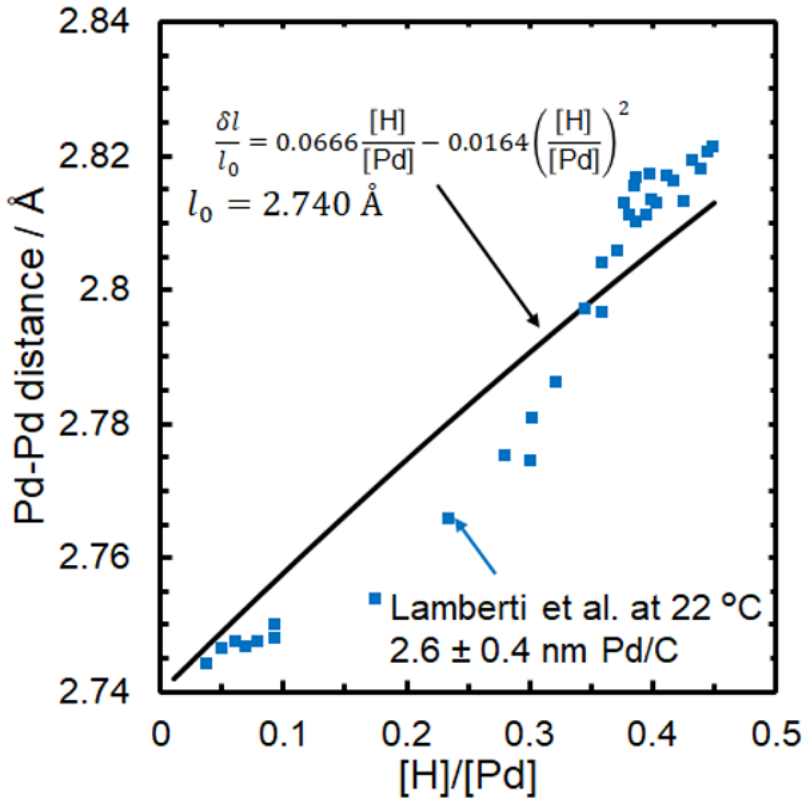

Figure 7-S6. The Pd-Pd first shell distance from EXAFS for Pd/C at 22 C from ref. [210] (blue squares) and calculated from Equation 7-1[221] (black line) plotted against the H to Pd ratio.

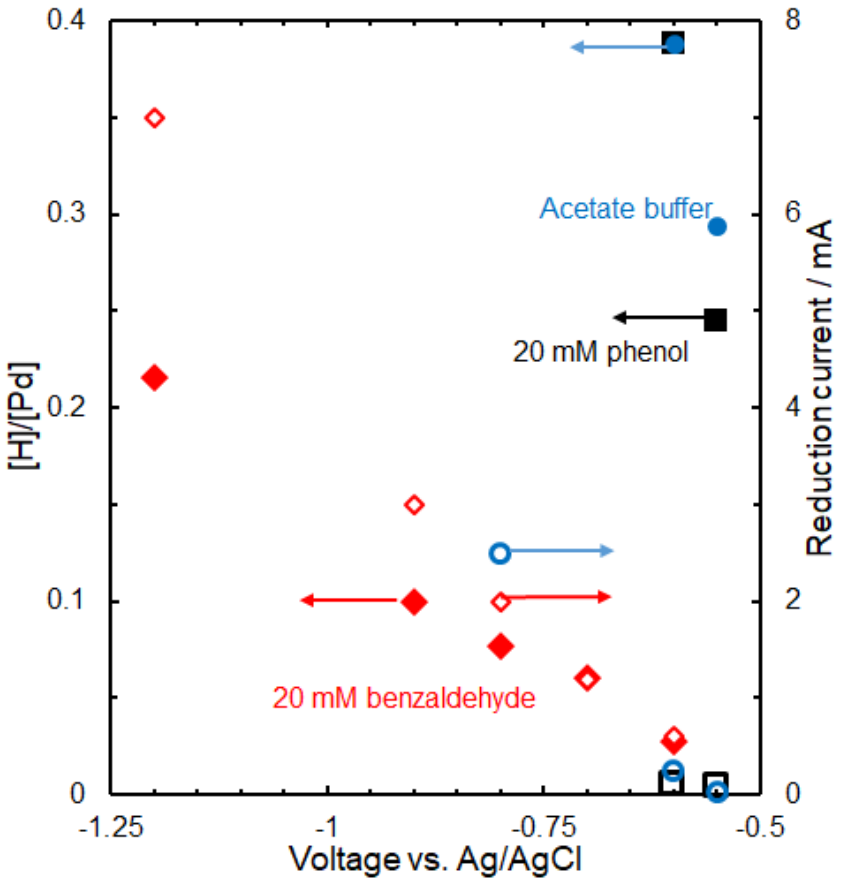

Figure 7-S7. [H]/[Pd] of the Pd/C catalyst for different electrochemical conditions based on change in Pd-Pd distance from EXAFS using Equation 7-1 (also shown in Figure 7-5). Reduction currents during the corresponding EXAFS measurement are shown on the right axis (i.e., open circles correspond to the current during the EXAFS measurement noted by closed circles, etc.). Note this is the total reduction current, which includes both ECH and hydrogen evolution reaction (HER) (for benzaldehyde it is expected >99% of the current is towards ECH, while for phenol and acetate buffer ~100% is towards HER).

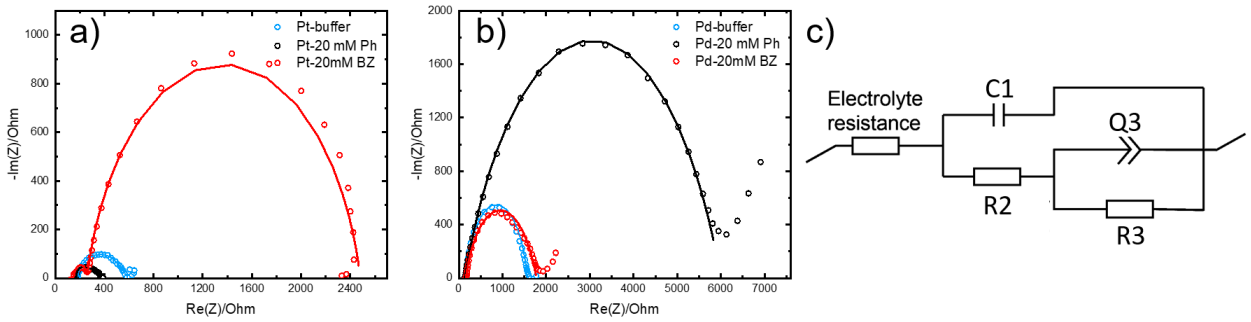

Figure 7-S8. Impedance spectra of polycrystalline disks (a) Pt and (b) Pd in 100 mM acetate buffer with 20 mM phenol (Ph) and benzaldehyde (BZ), measured at -0.5 V versus Ag/AgCl. Fits using the equivalent circuit in (c)[249–251] are presented in Table 7-S1. The reduced capacitance (C1) on Pt in the presence of organics suggests their displacement of some adsorbed H, even at potentials more cathodic than hydrogen evolution (0 V versus RHE is -0.4 V versus Ag/AgCl here).

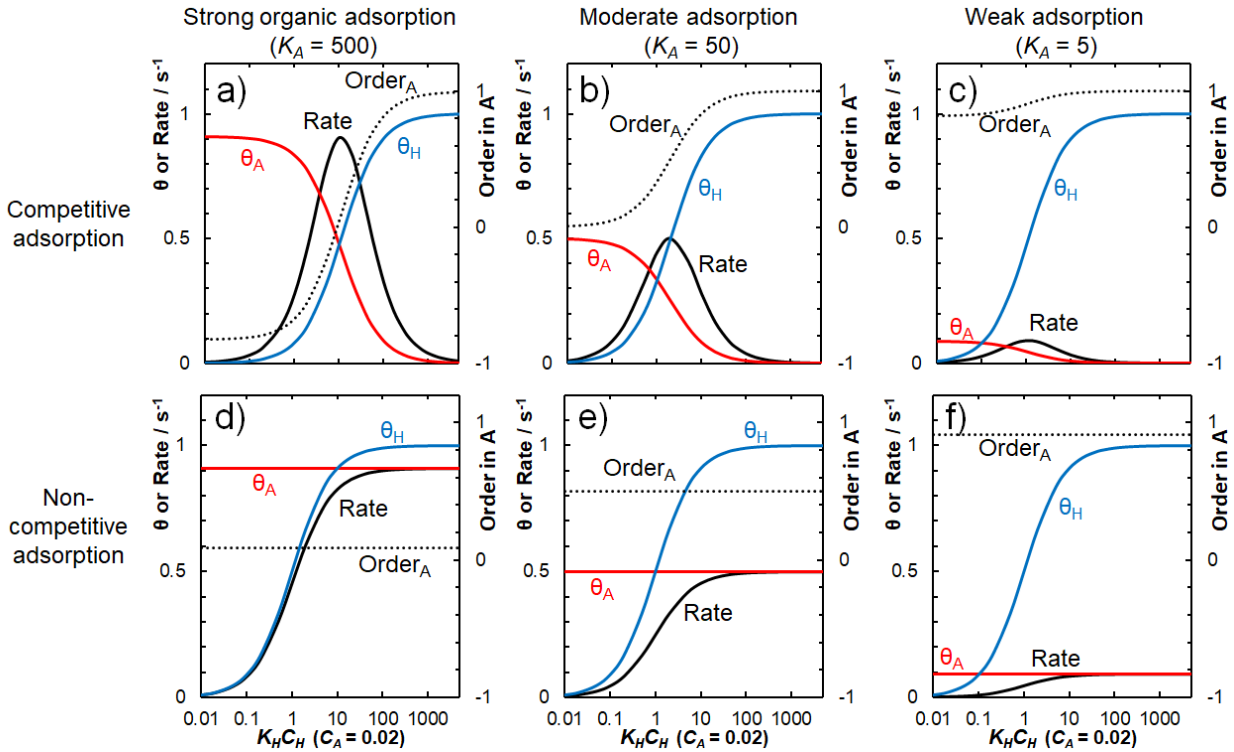

Figure 7-S9. Reaction rates, coverages of A and H (θ_A, θ_H), and order in A as a function of K_HC_H. Reaction models for competitive (a-c) and non-competitive adsorption (d-e) using Equation 7-S23 and Equation 7-S32, respectively, with strong adsorption of organic (a, d) K_A = 500, moderate adsorption (b, e) K_A = 50, and weak adsorption (c, f) K_A = 5. C_A = 0.02, $k_{LH,c}$ = 4 s^{-1}, $k_{LH,nc}$ = 1 s^{-1}.

7.8 Tables

Table 7-1. Turnover frequencies (s^{-1}) at 1 bar H_2 (TCH) or -0.7 V versus Ag/AgCl (~-0.3 V versus RHE), pH = 5 and 20 mM phenol or benzaldehyde (bnzal) at room temperature. Faradaic efficiencies at -0.7 V versus Ag/AgCl and 20 mM organic at room temperature. Values are taken from refs.[115,120,201,204] as indicated.

		Pt	Rh	Pd
Turnover frequencies (s^{-1})	**TCH phenol**	0.16 [115], 0.20	0.10 [204]	0.0057
	ECH phenol	~0.16 [115]	0.13 [204]	< 0.002 [201]
	TCH bnzal	0.12 [120]	0.27 [120]	0.30 [120]
	ECH bnzal	0.45 [120]	0.40 [120]	0.51 [120]
Faradaic Efficiency to ECH	**ECH phenol**	~40%	70% [204]	< 1% [201]
	ECH bnzal	~50% [120]	~60% [120]	~99% [120]

Table 7-2. Reaction order in phenol or benzaldehyde (bnzal) concentration at room temperature, and apparent activation energies. For values taken from literature, the reference number is given in brackets. Reaction order and apparent activation energy were measured at ~20 mM organic (see Figures 7-1 and 7-2), pH = 5, and T = 25 °C. (A temperature range from 5 to 40 °C[201] was used.) For TCH, values are measured at 1 bar H_2, and for ECH at -0.7 V versus Ag/AgCl. Uncertainties in reaction orders taken from ref.[120] were estimated assuming 10% standard deviation in TOF measurements.

		Pt	**Rh**	**Pd**
Reaction orders	**TCH phenol**	~ + 0.6	0 [201,204]	~ + 0.5
	ECH phenol	-	0 [204]	-
	TCH bnzal	(0 ± 0.2) [120]	(0 ± 0.2) [120]	(0 ± 0.2) [120]
	ECH bnzal	+ (1 ± 0.2) [120]	+ (1 ± 0.2) [120]	(0 ± 0.2) [120]
Apparent activation energies (kJ/mol)	**TCH phenol**	33 [201,204]	-	-
	ECH phenol	29 [201,204]	23 [201]	-
	TCH bnzal	32 [120]	27 [120]	21 [120]
	ECH bnzal	25 [120]	21 [120]	14 [120]

Table 7-3. Value of parameters used to fit the Pd K-edge EXAFS spectra of Pd/C under different electrochemical potentials (versus Ag/AgCl) in flowing acetate buffer with and without 20 mM phenol or benzaldehyde (bnzal) at room temperature. Only the first Pd-Pd shell is shown, but the first four Pd-Pd shells and two multiple scattering Pd-Pd shells were used for fitting, as well as two Pd-C pathways (shown here). A constant Debye-Waller factor for C pathways of 0.005 $Å^2$ was used based on fitting from multiple averaged spectra of a sample under conditions with high signal to noise, as detailed in the experimental section. S_0^2 (Amplitude reduction factor) = 0.7975 and ΔE_0 = -2.118 eV were used for fits based on the reference Pd foil spectra taken concurrently with the Pd/C sample.

	Pd-Pd interactions				**Pd-C interactions**	
	Pd-Pd 1st Shell (Å)	**Pd-Pd CN**	**Debye-Waller factor (Å)**	**3rd cumulant**	**Pd-C (Å)**	**Pd-C CN**
Pd foil	2.758	12	0.0054	0.00012	-	-
-0.55 V	2.809	8.3	0.0077	0.00032	2.11	0.6
-0.6 V	2.824	9.5	0.009	0.0002	2.08	0.6
-0.55 V phenol	2.801	7.2	0.007	0.0001	2.12, 2.88	0.39, 1.77
-0.6 V phenol	2.824	8.87	0.0089	0.0003	2.11, 3.02	0.38, 1.33
-0.6 V bnzal	2.763	8.3	0.0076	0.00003	2.14, 2.89	0.59, 1.78
-0.7 V bnzal	2.769	6.8	0.0051	0.00025	2.14, 2.8	0.8, 1.5
-0.8 V bnzal	2.772	9.2	0.0077	0.00013	2.19, 2.996	0.7, 0.7
-0.9 V bnzal	2.776	7.6	0.0062	0.0002	2.16, 2.8	0.61, 1.67
-1.2 V bnzal	2.796	7.97	0.0069	0.00028	2.17, 2.59	1.64, 1.34

Table 7-S1. Fitted components to the equivalent circuit presented in Figure 7-S8c for rotating disk electrodes in 100 mM acetate buffer with noted phenol and benzaldehyde concentration. C1 represents the double layer capacitance of the metal-electrolyte interface and is proportional to the area of metal surface in contact with electrolyte.[224] R2 is a charge transfer resistance (often specific to the H^+/H_{ads} charge transfer resistance[252]). Q3 is a constant phase element with parameter a3, where a3 = 1 corresponds to Q3 behaving as an ideal capacitor. Q3 is often related to the pseudo-capacitance of adsorbed species (e.g. hydrogen).[251] R3 is related to the charge transfer resistance of those adsorbed species, possibly a combination of hydrogen evolution and organic reduction.

	C1 [µF]	**R2 [Ω]**	**Q3 [µF s^{a3-1}]**	**a3**	**R3 [Ω]**
Pt-buffer	3.02	54.03	198	0.5265	348
Pt-20 mM Ph	1.66	80.4	388	0.5824	125
Pt-20 mM BZ	0.104	106.9	45.9	0.8511	2223
Pd-buffer	0.0933	22.04	6.97	0.8429	1407
Pd-20 mM Ph	0.127	14.53	14.2	0.6875	5850
Pd-20 mM BZ	0.352	16.21	12.4	0.6696	1597

Chapter 8 Conclusions

To summarize, this dissertation provides further systematic understandings of the energetics of adsorption of small molecules and molecular fragments on transition metal catalysts, which also act as important benchmarks for computational modeling methods like DFT. These insights are crucial for a wide range of applications, including both well-established industrial catalytic processes and emergent clean-energy technologies aimed at transitioning society off of our reliance of fossil fuels.

Chapter 2 provides a summary of the single crystal adsorption calorimetry instrument and standard experimental procedures. This system has been used to study the adsorption energetics of adsorbates of interest in chapters 3-6.

Chapter 3 describes the study of acetonitrile adsorption on Pt(111), studied by SCAC at 100 and 180 K. At 180 K, the integral heat of adsorption is 74.3 kJ/mol at a saturation coverage of 0.25 ML and well fit at lower coverages by (82.9−34.4θ) kJ/mol. At 180 K, the initial differential heat of adsorption is 82.9 kJ/mol, which decreases to 63.2 kJ/mol by 0.25 ML. At 100 K, the initial heat of adsorption is 84.5 kJ/ mol, which decreases to ~45 kJ/mol at the completion of the first layer (0.35 ML), and finally drops to a multilayer heat of 43.4 kJ/mol above coverages of 0.7 ML. This difference in saturation coverage of the first layer at 100 versus 180 K is a result of the formation of two different surface adsorbate configurations, μ and N-top, with the former being more energetically favorable but the latter arising in the presence of stearic constraints, which are present at 100 K due to lower adsorbate mobility across the surface. These present results agree well with recent TPD and RAIRS studies, and collectively these results provide a clear understanding of the nature of the interaction between acetonitrile, the simplest organic nitrile, and Pt(111). Using the 100 K heat of adsorption curve measured out to multilayer

coverages, we estimate the adhesion energy for liquid acetonitrile to Pt(111) to be 0.198 J/m^2. This is slightly higher than that of formic acid and methanol to Pt(111) but considerably lower than that of water, benzene, and phenol. This adhesion energy is useful for estimating the effects of acetonitrile as a solvent on the adsorption energies of catalytic reaction intermediates of interest in liquid-phase catalytic and electrocatalytic reactions.

Chapter 4 describes the SCAC study of *n*-decane adsorption on the Pt(111) surface at 150 K. The initial heat of adsorption was nearly constant at 152 kJ/mol though 0.0455 ML (except for the first two points below 0.004 ML, which were ~17 kJ/mol higher and attributed to defect sites). The heat then dropped to ~90 kJ/mol by 0.091 ML, then decreased to the multilayer heat of adsorption of 84.9 kJ/mol above 0.27 ML. The integral heat of adsorption at the saturation coverage of the first layer of adsorbed *n*-decane (0.091 ML) was 132.7 kJ/mol. This was close to that predicted based on desorption energies measured by TPD for shorter *n*-alkane on Pt(111) (C_1-C_6), which were found by Tait et al.[144] to increase nearly proportional to carbon number. Using the experimentally measured heat of adsorption versus coverage out to a bulk-like multilayer coverage, we estimate the adhesion energy of liquid *n*-decane on Pt(111) to be 0.148 J/m^2. This is very close to the adhesion energy per unit area of *n*-hexane on Pt(111) estimated based on TPD desorption energies. Thus, linear alkanes have average heats of adsorption in close-packed islands on Pt(111) which approximately equal to a constant (13.3 kJ/mol per C atom) times their total number of CH_2 plus CH_3 groups, but because each CH_2 and CH_3 group occupies nearly the same area on the surface, the adhesion energy per unit area is also nearly a constant (0.15 J/m^2).

Chapter 5 describes the study of azulene adsorption on the Pt(111) using SCAC, and compares it to previous SCAC results of naphthalene adsorption on Pt(111) and DFT studies of

both systems. The isomers azulene and naphthalene constitute a versatile molecular model system to study interfacial interactions of the topological pentagon−heptagon (5−7) defects in graphene. The experimental and theoretical analyses reveal that both molecules are chemisorbed on Pt(111) but azulene forms the stronger bond. Its differential adsorption energy, as measured by SCAC, is larger by 68 to 116 kJ/mol, depending on the coverage, and reaches 416 kJ/mol at zero coverage, compared to 300 kJ/mol for naphthalene. The stronger bond of azulene and the coverage dependencies of the adsorption energies are qualitatively correctly predicted by dispersion-corrected DFT calculations. DFT reveals rehybridization toward sp^3 and a partially localized σ-character of the molecule−metal bond. The interfacial electron transfer occurs in both directions through donation and back-donation, resulting in the partial occupation (deoccupation) of orbitals that are unoccupied (occupied) in the free molecules, as shown by pEDA. Interpretation of the UP and NEXAFS spectra with an MO projection analysis supports the occupation/deoccupation mechanism of the surface chemical bond. It also reveals that the molecular orbitals of azulene and naphthalene respond differently to adsorption. This observation connects the topology-related differences in the electronic structure (especially the HOMO−LUMO gap) with the different bonds to the surface. Our analysis shows that the π-topology of an aromatic ring system substantially influences its interaction at a metal/organic interface in the regime of strong chemisorption. Topology-related effects are therefore relevant for various applications, including metal/organic interfaces in organic (opto)electronic devices or catalytic reactions of aromatic hydrocarbons on transition-metal surfaces.

Chapter 6 describes the SCAC study of the molecular and dissociative adsorption of formic acid on clean and oxygen-precovered Cu(111) and 120 and 240 K. The enthalpy of formation and bond enthalpy of bidentate formate to Cu(111) are -465 kJ/mol and 335 kJ/mol,

respectively, at 240 K and 0.20 ML. Corresponding enthalpies are estimated for monodentate formate on Cu(111), which give an enthalpy of formation of -437 kJ/mol and a bond enthalpy of 307 kJ/mol. A comparison to DFT calculations in the literature shows that DFT systematically underestimates the bond enthalpies and enthalpies of formation of mono- and bidentate formate to Cu(111). In comparison to experimental measurements on Pt(111) and Ni(111), these enthalpy values indicate that formate binds ~15 kJ/mol more strongly to Cu(111) than to Ni(111), and ~85 kJ/mol more strongly than to Pt(111). At 240 K, the integral heat of the dissociative adsorption of formic acid on oxygen-precovered Cu(111) is well fit by (99.1 – 46.8θ) kJ/mol, which gives an integral (average) heat of 89.7 kJ/mol at 0.20 ML. The initial differential heat of adsorption is 99.1, which decreases linearly to 80.4 kJ/mol by 0.20 ML. At 120 K, the molecular adsorption of formic acid on clean Cu(111) has an initial differential heat of adsorption of 80.9 kJ/mol, which decreases to ~70 kJ/mol by 0.50 ML. Past that coverage, the heat remains at ~70 kJ/mol through 1.5 ML, after which it drops to a multilayer energy of 64.3 kJ/mol by 1.75 ML. Using the 120 K heat of adsorption curve measured out to multilayer coverages, we estimate the adhesion energy for liquid formic acid to Cu(111) to be 0.271 J/m^2. These results constitute important benchmarks for DFT calculations and efforts to improve the energy accuracy of computational models, as they are (to our knowledge) the first experimental measurements of the energy of *any* molecular fragment on *any* Cu surface. As formate is the simplest example of a carboxylate adsorbate, these results are applicable not only for systems with formate, but as well as other carboxylates and, more broadly, other oxygenates on Cu surfaces. These results further our understanding of fundamental energetic differences on catalyst surfaces, and can help explain differences in catalytic activity between late transition metal catalysts and guide the development of new catalysts and catalytic pathways.

Chapter 7 describes the study of thermal and electrocatalytic hydrogenation reactions of phenol and benzaldehyde over Pt, Pd, and Rh. The dependences of the reaction rates on reactant concentrations and temperature for all cases of both ECH and TCH for benzaldehyde and phenol on Pt/C, Pd/C, and Rh/C in aqueous-phase can be described successfully by a Langmuir-Hinshelwood model where the rate-determining step is the addition of an adsorbed H from the surface to the molecularly-adsorbed organic molecule, which competes for sites with H. The rate changes from being nearly first-order in organic concentration to strongly negative order as the organic concentration increases, for phenol, due to this competitive adsorption with H*. Because of the much lower solubility of benzaldehyde in water, this same range in concentration cannot be spanned. For Pt/C, the adsorption equilibrium constants for the organic required to fit the rates with this model are consistent with independent measurements of those equilibrium constants on Pt(111)-like sites (but not other facets), suggesting these are the most active sites. The increase in ECH activity with more negative (cathodic) potential is attributed to the corresponding increase in surface hydrogen coverage. The apparent activation energy decreases in going from TCH to ECH conditions, attributed to the higher H* coverage which results from the applied potential in ECH. The high benzaldehyde adsorption constant on Pd (perhaps aided by its high intrinsic rate constant for benzaldehyde hydrogenation) causes the steady-state hydrogen coverage to be low, resulting in a high Faradaic efficiency towards benzaldehyde ECH over H_2 evolution. Pt and Rh have lower Faradaic efficiencies, and also higher orders in benzaldehyde for ECH, than Pd due to the lower benzaldehyde coverages on Pt and Rh. The high reaction rate of Pd towards benzaldehyde is not due to formation of β-PdH_x, which does not form under these conditions (unlike what has been found for CO_2 reduction). Adsorbed benzaldehyde is more reactive with

H* (i.e., has a higher intrinsic rate constant for H addition) than is adsorbed phenol on all three metals.

Collectively, these results advance our systematic understanding of observed trends and differences in reactivity amongst transitional metal catalysts. This can both inform why historically ubiquitous catalysts are good for certain classes of reactions and reaction pathways, as well as enable the intelligent screening and design of catalysts for emergent technologies. One important tool for enabling the rapid screening of catalysts is computational modeling methods such as DFT, and these results constitute key benchmarks for improving the energy accuracy of those models. The formic acid study on Cu(111) is worth highlighting as the first of these measurements of the energetics of molecular fragments on any Cu surface, and further systems on Cu(111) will be important for continuing this effort to expand our knowledge of catalysis on Cu surfaces. This dissertation presents fundamental insights to further inform and enable the rational and intelligent design of new catalysts and catalytic processes to meet the needs of modern human society.

Chapter 9 References

1. Thomas, J. M. & Thomas, W. J. *Principles and Practice of Heterogeneous Catalysis*. (Weinheim, 2008).
2. Chorkendorff, I. & Niemantsverdriet, J. W. *Concepts of Modern Catalysis and Kinetics*. (Wiley-VCH Verlag GmbH & Co. KGaA, 2007).
3. Farrauto, R. J. & Bartholomew, C. H. *Fundamentals of Industrial Catalytic Processes*. (Blackie Academic & Professional, 1997).
4. Ertl, G. *Reactions at Solid Surfaces*. (Wiley, 2009).
5. Boehm, H.-P., Knoezinger, H., Anderson, J. R. & Boudart, M. *Catalysis Science and Technology*. (Springer, 1983).
6. Centi, G., Cornils, B., Herrmann, W. A., Schloegl, R. & Wong, C.-H. *Catalysis from A to Z*. (Wiley-VCH Verlag GmbH & Co. KGaA, 2000).
7. C., B. G. *Heterogeneous Catalysis: Principles & Applications*. (Oxford University Press, 1984).
8. Erisman, J. W., Sutton, M. A., Galloway, J., Klimont, Z. & Winiwarter, W. How a century of ammonia synthesis changed the world. *Nat. Geosci.* **1**, 636–639 (2008).
9. Suplee, C. *What You Need to Know About Energy*. (The National Academies Press, 2008).
10. Baerns, M. & Holena, M. *Combinatorial Development of Solid Catalytic Materials: Design of High-Throughput Experiments, Data Analysis, Data Mining*. (World Scientific, 2009).
11. Richarson, J. T. *Principles of Catalyst Development*. (Plenum Press, 1989).
12. Ozkan, U. S. *Design of Heterogeneous Catalysts*. (Wiley, 2009).
13. Greeley, J. & Nørskov, J. K. Large-scale, density functional theory-based screening of alloys for hydrogen evolution. *Surf. Sci.* **601**, 1590–1598 (2007).
14. Studt, F. *et al.* Identification of Non-Precious Metal Alloy Catalysts for Selective Hydrogenation of Acetylene. *Science (80-.).* **320**, 1320–1322 (2008).
15. Greeley, J., Nørskov, J. K., Kibler, L. A., El-Aziz, A. M. & Kolb, D. M. Hydrogen Evolution Over Bimetallic Systems: Understanding the Trends. *ChemPhysChem* **7**, 1032–1035 (2006).
16. Greeley, J. & Mavrikakis, M. Alloy catalysts designed from first principles. *Nat. Mater.* **3**, 810–815 (2004).
17. Greeley, J. *et al.* Alloys of platinum and early transition metals as oxygen reduction electrocatalysts. *Nat. Chem.* **1**, 552–556 (2009).
18. Nørskov, J. K., Bligaard, T., Rossmeisl, J. & Christensen, C. H. Towards the computational design of solid catalysts. *Nat. Chem.* **1**, 37–46 (2009).

19. Mavrikakis, M. Computational Methods: A search engine for catalysts. *Nat. Mater.* **5**, 847–848 (2006).

20. Nørskov, J. K., Abild-Pedersen, F., Studt, F. & Bligaard, T. Density functional theory in surface chemistry and catalysis. *Proc. Natl. Acad. Sci. U. S. A.* **108**, 937–943 (2011).

21. Wellendorff, J. *et al.* A benchmark database for adsorption bond energies to transition metal surfaces and comparison to selected DFT functionals. *Surf. Sci.* **640**, 36–44 (2015).

22. Freund, H.-J., Nilius, N., Risse, T., Schauermann, S. & Schmidt, T. Innovative Measurement Techniques in Surface Science. *Chem. Phys. Chem.* **12**, 79–87 (2011).

23. Brown, W. A., Kose, R. & King, D. A. Femtomole Adsorption Calorimetry on Single-Crystal Surfaces. *Chem. Rev.* **98**, 797–831 (1998).

24. Borroni-Bird, C. E. & King, D. A. An ultrahigh vacuum single crystal adsorption microcalorimeter. *Rev. Sci. Instrum.* **62**, 2177–2185 (1991).

25. Lew, W., Lytken, O., Farmer, J. A., Crowe, M. C. & Campbell, C. T. Improved pyroelectric detectors for single crystal adsorption calorimetry from 100 to 350 K. *Rev. Sci. Instrum.* **81**, 1–9 (2010).

26. Ajo, H. M., Ihm, H., Moilanen, D. E. & Campbell, C. T. Calorimeter for adsorption energies of larger molecules on single crystal surfaces. *Rev. Sci. Instrum.* **75**, 4471–4480 (2004).

27. Silbaugh, T. L. & Campbell, C. T. Energies of Formation Reactions Measured for Adsorbates on Late Transition Metal Surfaces. *J. Phys. Chem. C* **120**, 25161–25172 (2016).

28. Karp, E. M., Silbaugh, T. L. & Campbell, C. T. Energetics of Adsorbed CH3 and CH on Pt(111) by Calorimetry: Dissociative Adsorption of CH3I. *J. Phys. Chem. C* **117**, 6325–6336 (2013).

29. Lew, W. *et al.* The Energy of Adsorbed Hydroxyl on Pt(111) by Microcalorimetry. *J. Phys. Chem. C* **115**, 11586–11594 (2011).

30. Silbaugh, T. L., Karp, E. M. & Campbell, C. T. Energetics of Formic Acid Conversion to Adsorbed Formates on Pt(111) by Transient Calorimetry. *J. Am. Chem. Soc.* **136**, 3964–3971 (2014).

31. Lew, W., Crowe, M. C., Karp, E. & Campbell, C. T. Energy of Molecularly Adsorbed Water on Clean Pt(111) and Pt(111) with Coadsorbed Oxygen by Calorimetry. *J. Phys. Chem. C* **115**, 9164–9170 (2011).

32. Karp, E. M., Silbaugh, T. L., Crowe, M. C. & Campbell, C. T. Energetics of Adsorbed Methanol and Methoxy on Pt(111) by Microcalorimetry. *J. Am. Chem. Soc.* **134**, 20388–20395 (2012).

33. Karp, E. M., Campbell, C. T., Studt, F., Abild-Pedersen, F. & Nørskov, J. K. Energetics of Oxygen Adatoms, Hydroxyl Species and Water Dissociation on Pt(111). *J. Phys. Chem. C* **116**, 25772–25776 (2012).

34. Carey, S. J., Zhao, W., Mao, Z. & Campbell, C. T. Energetics of Adsorbed Phenol on Ni(111) and Pt(111) by Calorimetry. *J. Phys. Chem. C* **123**, 7627–7632 (2019).

35. Zhao, W., Carey, S. J., Morgan, S. E. & Campbell, C. T. Energetics of adsorbed formate and formic acid on Ni(111) by calorimetry. *J. Catal.* **352**, 300–304 (2017).

36. Carey, S. J., Zhao, W. & Campbell, C. T. Bond Energies of Adsorbed Intermediates to Metal Surfaces: Correlation with Hydrogen – Ligand and Hydrogen – Surface Bond Energies and Electronegativities. *Angew. Chemie - Int. Ed.* **57**, 16877–16881 (2018).

37. Zhao, W., Carey, S. J., Mao, Z. & Campbell, C. T. Adsorbed Hydroxyl and Water on Ni(111): Heats of Formation by Calorimetry. *ACS Catal.* **8**, 1485–1489 (2018).

38. Carey, S. J., Zhao, W., Frehner, A., Campbell, C. T. & Jackson, B. Energetics of Adsorbed Methyl and Methyl Iodide on Ni(111) by Calorimetry: Comparison to Pt(111) and Implications for Catalysis. *ACS Catal.* **7**, 1286–1294 (2017).

39. Carey, S. J. *et al.* Energetics of Adsorbed Methanol and Methoxy on Ni(111): Comparisons to Pt(111). *ACS Catal.* **8**, 10089–10095 (2018).

40. Campbell, C. T. Energies of Adsorbed Catalytic Intermediates on Transition Metal Surfaces: Calorimetric Measurements and Benchmarks for Theory. *Acc. Chem. Res.* **52**, 984–993 (2019).

41. Bligaard, T. *et al.* Toward Benchmarking in Catalysis Science: Best Practices, Challenges, and Opportunities. *ACS Catal.* **6**, 2590–2602 (2016).

42. Akinola, J., Campbell, C. T. & Singh, N. Effects of Solvents on Adsorption Energies: a General Bond-Additivity Model. *J. Phys. Chem. C* **125**, 24371–24380 (2021).

43. Singh, N. & Campbell, C. T. A Simple Bond-Additivity Model Explains Large Decreases in Heats of Adsorption in Solvents Versus Gas Phase: A Case Study with Phenol on Pt(111) in Water. *ACS Catal.* **9**, 8116–8127 (2019).

44. Rumptz, J. R. & Campbell, C. T. Adhesion Energies of Solvent Films to Pt(111) and Ni(111) Surfaces by Adsorption Calorimetry. *ACS Catal.* **9**, 11819–11825 (2019).

45. Yamada, Y. *et al.* Unusual Stability of Acetonitrile-Based Superconcentrated Electrolytes for Fast-Charging Lithium-Ion Batteries. *J. Am. Chem. Soc.* **136**, 5039–5046 (2014).

46. Lane, G. H. & Jezek, E. Electrochemical studies of acetonitrile based supercapacitor electrolytes containing alkali and alkaline earth metal cations. *Electrochim. Acta* **150**, 173–187 (2014).

47. Zhang, S. *et al.* Insights into the effects of solvent properties in graphene based electric double-layer capacitors with organic electrolytes. *J. Power Sources* **334**, 162–169 (2016).

48. Trinh, N. D. *et al.* An Artificial Lithium Protective Layer that Enables the Use of Acetonitrile-Based Electrolytes in Lithium Metal Batteries. *Angew. Chemie - Int. Ed.* **57**, 5072–5075 (2018).

49. Dou, Q. *et al.* Safe and high-rate supercapacitors based on an 'acetonitrile/water in salt' hybrid electrolyte. *Energy Environ. Sci.* **11**, 3212 (2018).

50. Zhang, Y. *et al.* Direct conversion of cellulose and raw biomass to acetonitrile by catalytic fast pyrolysis in ammonia. *Green Chem.* **21**, 812–820 (2019).

51. Mellmer, M. A. *et al.* Solvent-enabled control of reactivity for liquid-phase reactions of biomass-derived compounds. *Nat. Catal.* **1**, 199–207 (2018).

52. Walker, T. W. *et al.* Universal kinetic solvent effects in acid-catalyzed reactions of biomass-derived oxygenates. *Energy Environ. Sci.* **11**, 617–628 (2018).

53. He, J. *et al.* Production of levoglucosenone and 5-hydroxymethylfurfural from cellulose in polar aprotic solvent-water mixtures. *Green Chem.* **19**, 3642–3653 (2017).

54. Kryachko, E. S. & Nguyen, M. T. Hydrogen Bonding between Phenol and Acetonitrile. *J. Phys. Chem. A* **106**, 4267–4271 (2002).

55. Tylinski, M., Smith, R. S. & Kay, B. D. Structure and Desorption Kinetics of Acetonitrile Thin Films on Pt (111) and on Graphene on Pt (111). *J. Phys. Chem. C* **124**, 2521–2530 (2020).

56. Tait, S. L., Dohnalek, Z., Campbell, C. T. & Kay, B. D. n-alkanes on Pt(111) and on C(0001)/Pt(111): Chain length dependence of kinetic desorption parameters. *J. Chem. Phys.* **125**, 1–15 (2006).

57. Rumptz, J. R. & Campbell, C. T. Adhesion Energies of Liquid Hydrocarbon Solvents onto Pt(111), MgO(100), Graphene, and TiO2(110) from Temperature-Programmed Desorption Energies. *J. Phys. Chem. C* **125**, 27931–27937 (2021).

58. Lytken, O. *et al.* Energetics of Cyclohexene Adsorption and Reaction on Pt(111) by Low-Temperature Microcalorimetry. *J. Am. Chem. Soc.* **130**, 10247–10257 (2008).

59. Ihm, H., Ajo, H. M., Gottfried, J. M., Bera, P. & Campbell, C. T. Calorimetric measurement of the heat of adsorption of benzene on Pt(111). *J. Phys. Chem. B* **108**, 14627–14633 (2004).

60. Gottfried, J. M., Vestergaard, E. K., Bera, P. & Campbell, C. T. Heat of Adsorption of Naphthalene on Pt(111) Measured by Adsorption Calorimetry. *J. Phys. Chem. B* **110**, 17539–17545 (2006).

61. Klein, B. P. *et al.* Enhanced Bonding of Pentagon − Heptagon Defects in Graphene to Metal Surfaces: Insights from the Adsorption of Azulene and Naphthalene to Pt(111). *Chem. Mater.* **32**, 1041–1053 (2020).

62. Geim, A. K. & Novoselov, K. S. The rise of graphene. *Nat. Mater.* **6**, 183–191 (2007).

63. Kim, P. Graphene: Across the border. *Nat. Mater.* **9**, 792–793 (2010).

64. Tsen, A. W. *et al.* Tailoring Electrical Transport Across Grain Boundaries in Polycrystalline Graphene. *Science (80-.).* **336**, 1143–1146 (2012).

65. Huang, P. Y. *et al.* Grains and grain boundaries in single-layer graphene atomic patchwork quilts. *Nature* **469**, 389+ (2011).

66. Yazyev, O. V & Louie, S. G. Electronic transport in polycrystalline graphene. *Nat. Mater.*

9, 806–809 (2010).

67. Kim, K. *et al.* Grain Boundary Mapping in Polycrystalline Graphene. *ACS Nano* **5**, 2142–2146 (2011).

68. Grantab, R., Shenoy, V. B. & Ruoff, R. S. Anomalous Strength Characteristics of Tilt Grain Boundaries in Graphene. *Science (80-.).* **330**, 946–948 (2010).

69. Rasool, H. I., Ophus, C., Klug, W. S., Zettl, A. & Gimzewski, J. K. Measurement of the intrinsic strength of crystalline and polycrystalline graphene. *Nat. Commun.* **4**, (2013).

70. Ito, Y. *et al.* Correlation between Chemical Dopants and Topological Defects in Catalytically Active Nanoporous Graphene. *Adv. Mater.* **28**, 10644 (2016).

71. Malola, S., Hakkinen, H. & Koskinen, P. Structural, chemical, and dynamical trends in graphene grain boundaries. *Phys. Rev. B* **81**, (2010).

72. Wei, Y. *et al.* The nature of strength enhancement and weakening by pentagon – heptagon defects in graphene. *Nat. Mater.* **11**, 759–763 (2012).

73. Shekhawat, A. & Ritchie, R. O. Toughness and strength of nanocrystalline graphene. *Nat. Commun.* **7**, (2016).

74. Cervenka, J., Katsnelson, M. I. & Flipse, C. F. J. Room-temperature ferromagnetism in graphite driven by two-dimensional networks of point defects. *Nat. Phys.* **5**, 840–844 (2009).

75. Batzill, M. The surface science of graphene: Metal interfaces, CVD synthesis, nanoribbons, chemical modifications, and defects. *Surf. Sci. Rep.* **67**, 83–115 (2012).

76. Wang, R. *et al.* Graphene based functional devices: A short review. *Front. Phys.* **14**, (2019).

77. Dahlgren, D. & Hemminger, J. C. Chemisorption and Ordering of Naphthalene and Azulene on Pt(s)[7(111)x(100)]: The Effect of Periodic Defects on Long Range Order. **134**, 836–848 (1983).

78. Dahlgren, D., Hemminger, J. C., Dahlgren, D. & Hemminger, J. C. The nature of the phase transition observed for monolayers of azulene on Pt (111) a). **5573**, 1–3 (1981).

79. Dahlgren, D. & Hemminger, J. C. Chemisorption and Thermal Chemistry of Azulene and Naphthalene Adsorbed on Pt(111). *Surf. Sci.* **114**, 459–470 (1982).

80. Gland, J. L. & Somorjai, G. A. Low Energy Eelektron Diffraction and Work Function Studies of Benzene, Naphthalene and Pyridine Adsorbed on Pt(111) and Pt(100) Single Crystal Surfaces. *Surf. Sci.* **38**, 157–186 (1973).

81. Hallmark, V. M., Chiang, S., Meinhardt, K.-P. & Hafner, K. Observation and Calculation of Internal Structure in Scanning Tunneling Microscopy Images of Related Molecules. *Phys. Rev. Lett.* **70**, 3740–3743 (1993).

82. Hallmark, V. M. & Chiang, S. Imaging Structural Details in Closely Related Molecular Adsorbate Systems. *Surf. Sci.* **286**, 190–200 (1993).

83. Hallmark, V. M., Chiang, S., Brown, J. K. & Woll, C. Real-Space Imaging of the Molecular Orientation of Naphthalene on Pt(111). *Phys. Rev. Lett.* **66**, 48–51 (1991).

84. Morin, C., Simon, D. & Sautet, P. Trends in the Chemisorption of Aromatic Molecules on a Pt(111) Surface: Benzene, Naphthalene, and Anthracene from First Principles Calculations. *J. Phys. Chem. B* **108**, 12084–12091 (2004).

85. Santarossa, G., Iannuzzi, M., Vargas, A. & Baiker, A. Adsorption of naphthalene and quinoline on Pt, Pd and Rh: A DFT study. *Chem. Phys. Chem.* **9**, 401–413 (2008).

86. Klein, B. P. *et al.* Molecular Topology and the Surface Chemical Bond: Alternant Versus Nonalternant Aromatic Systems as Functional Structural Elements. *Phys. Rev. X* **9**, (2019).

87. Klein, B. P. *et al.* Molecule-Metal Bond of Alternant versus Nonalternant Aromatic Systems on Coinage Metal Surfaces: Naphthalene versus Azulene on Ag(111) and Cu(111). *J. Phys. Chem. C* **123**, 29219–29230 (2019).

88. Shiozawa, Y., Koitaya, T., Mukai, K., Yoshimoto, S. & Yoshinobu, J. The roles of step-site and zinc in surface chemistry of formic acid on clean and Zn-modified Cu(111) and Cu(997) surfaces studied by HR-XPS, TPD, and IRAS. *J. Chem. Phys.* **152**, 1–12 (2020).

89. Gokhale, A. A., Dumesic, J. A. & Mavrikakis, M. On the Mechanism of Low-Temperature Water Gas Shift Reaction on Copper. *J. Am. Chem. Soc.* **130**, 1402–1414 (2008).

90. Zhang, R., Ludviksson, A. & Campbell, C. T. The chemisorption of methanol on Cu films on ZnO(0001)-O. *Catal. Letters* **25**, 277–292 (1994).

91. Lin, S., Johnson, R. S., Smith, G. K., Xie, D. & Guo, H. Pathways for methanol steam reforming involving adsorbed formaldehyde and hydroxyl intermediates on Cu(111): density functional theory studies. *Phys. Chem. Chem. Phys.* **13**, 9622–9631 (2011).

92. Chen, B. W. J., Bhandari, S. & Mavrikakis, M. Role of Hydrogen-bonded Bimolecular Formic Acid−Formate Complexes for Formic Acid Decomposition on Copper: A Combined First-Principles and Microkinetic Modeling Study. *ACS Catal.* **11**, 4349–4361 (2021).

93. Li, S., Scaranto, J. & Mavrikakis, M. On the Structure Sensitivity of Formic Acid Decomposition on Cu Catalysts. *Top. Catal.* **59**, 1580–1588 (2016).

94. Baber, A. E. *et al.* Assisted deprotonation of formic acid on Cu(111) and self-assembly of 1D chains. *Phys. Chem. Chem. Phys.* **15**, 12291–12298 (2013).

95. Putra, S. E. M. *et al.* Theoretical study on adsorption and reaction of polymeric formic acid on the Cu (111) surface. *Phys. Rev. Mater.* **5**, 1–9 (2021).

96. Putra, S. E. M. *et al.* Van der Waals density functional study of formic acid adsorption and decomposition on Cu(111). *J. Chem. Phys.* **150**, 1–10 (2019).

97. Durand, W. J., Peterson, A. A., Studt, F., Abild-Pedersen, F. & Nørskov, J. K. Structure effects on the energetics of the electrochemical reduction of CO2 by copper surfaces. *Surf. Sci.* **605**, 1354–1359 (2011).

98. Qiao, J., Liu, Y., Hong, F. & Zhang, J. A review of catalysts for the electroreduction of carbon dioxide to produce low-carbon fuels. *Chem Soc Rev* **43**, 631–675 (2014).

99. Quan, J. *et al.* Vibration-driven reaction of CO2 on Cu surfaces via Eley-Rideal-type mechanism. *Nat. Chem.* **11**, 722–729 (2019).

100. Wang, Y.-F., Li, K. & Wang, G.-C. Formic acid decomposition on Pt1/Cu(111) single platinum atom catalyst: Insights from DFT calculations and energetic span model analysis. *Appl. Surf. Sci.* **436**, 631–638 (2018).

101. Yoo, J. S., Abild-Pedersen, F., Nørskov, J. K. & Studt, F. Theoretical Analysis of Transition-Metal Catalysts for Formic Acid Decomposition. *ACS Catal.* **4**, 1226–1233 (2014).

102. Herron, J. A., Scaranto, J., Ferrin, P., Li, S. & Mavrikakis, M. Trends in Formic Acid Decomposition on Model Transition Metal Surfaces: A Density Functional Theory study. *ACS Catal.* **4**, 4434–4445 (2014).

103. Appel, A. M. *et al.* Frontiers, Opportunities, and Challenges in Biochemical and Chemical Catalysis of CO2 Fixation. *Chem. Rev.* **113**, 6621–6658 (2013).

104. Hori, Y., Wakebe, H. H. I., Tsukamoto, T. & Koga, O. Electrocatalytic Process of CO Selectivity in Electrochemical Reduction of CO2 at Metal Electrodes in Aqueous Media. *Electrochim. Acta* **39**, 1833–1839 (1994).

105. Nie, X., Esopi, M. R., Janik, M. J. & Asthagiri, A. Selectivity of CO2 Reduction on Copper Electrodes: The Role of the Kinetics of Elementary Steps. *Angew. Chemie - Int. Ed.* **52**, 2459–2462 (2013).

106. Grabow, L. C., Gokhale, A. A., Evans, S. T., Dumesic, J. A. & Mavrikakis, M. Mechanism of the Water Gas Shift Reaction on Pt: First Principles, Experiments, and Microkinetic Modeling. *J. Phys. Chem. C* **112**, 4608–4617 (2008).

107. Chheda, J. N., Huber, G. W. & Dumesic, J. A. Liquid-Phase Catalytic Processing of Biomass-Derived Oxygenated Hydrocarbons to Fuels and Chemicals. *Angew. Chemie - Int. Ed.* **46**, 7164–7183 (2007).

108. Zhou, C.-H., Xia, X., Lin, C.-X., Tong, D.-S. & Beltramini, J. Catalytic conversion of lignocellulosic biomass to fine chemicals and fuels. *Chem. Soc. Rev.* **40**, 5588–5617 (2011).

109. Jiang, Y. *et al. Green Conversion of Biomass to Green Chemicals*. *Sustainable Production of Bulk Chemicals: Integration of Bio-, Chemo- Resources and Processes* (2015). doi:10.1007/978-94-017-7475-8

110. Huber, G. H., Iborra, S. & Corma, A. Synthesis of Transportation Fuels from Biomass: Chemistry, Catalysts, and Engineering. *Chem. Rev.* **106**, 4044–4098 (2006).

111. Alonso, D. M., Wettstein, S. G. & Dumesic, J. A. Bimetallic catalysts for upgrading of biomass to fuels and chemicals. *Chem. Soc. Rev.* **41**, 8075–8098 (2012).

112. Singh, N. *et al.* Aqueous phase catalytic and electrocatalytic hydrogenation of phenol and

benzaldehyde over platinum group metals. *J. Catal.* **382**, 372–384 (2020).

113. Singh, N. *et al.* Carbon-supported Pt during aqueous phenol hydrogenation with and without applied electrical potential: X-ray absorption and theoretical studies of structure and adsorbates. *J. Catal.* **368**, 8–19 (2018).

114. Singh, N. *et al.* Impact of pH on aqueous-phase phenol hydrogenation catalyzed by carbon-supported Pt and Rh. *ACS Catal.* **9**, 1120–1128 (2019).

115. Singh, N. *et al.* Electrocatalytic Hydrogenation of Phenol over Platinum and Rhodium: Unexpected Temperature Effects Resolved. *ACS Catal.* **6**, 7466–7470 (2016).

116. Singh, N. *et al.* Quantifying Adsorption of Organic Molecules on Platinum in Aqueous Phase by Hydrogen Site Blocking and in Situ X-ray Absorption Spectroscopy. *ACS Catal.* **9**, 6869–6881 (2019).

117. Sanyal, U. *et al.* Structure Sensitivity in Hydrogenation Reactions on Pt/C in Aqueous-phase. *ChemCatChem* **11**, 575–582 (2019).

118. Song, Y., Gutierrez, O. Y., Herranz, J. & Lercher, J. A. Aqueous phase electrocatalysis and thermal catalysis for the hydrogenation of phenol at mild conditions. *Appl. Catal. B Environ.* **182**, 236–246 (2016).

119. Song, Y., Chia, S. H., Sanyal, U., Gutierrez, O. Y. & Lercher, J. A. Integrated catalytic and electrocatalytic conversion of substituted phenols and diaryl ethers. *J. Catal.* **344**, 263–272 (2016).

120. Song, Y. *et al.* Hydrogenation of benzaldehyde via electrocatalysis and thermal catalysis on carbon-supported metals. *J. Catal.* **359**, 68–75 (2018).

121. King, D. A. & Wells, M. G. Molecular Beam Investigation of Adsorption Kinetics on Bulk Metal Targets: Nitrogen on Tungsten. *Surf. Sci.* **29**, 454–482 (1972).

122. Ruehl, G., Harman, S. E., Arnadottir, L. & Campbell, C. T. Acetonitrile Adsorption and Adhesion Energies onto the Pt (111) Surface by Calorimetry. *ACS Catal.* **12**, 156–163 (2022).

123. Singh, N. & Campbell, C. T. A Simple Bond-Additivity Model Explains Large Decreases in Heats of Adsorption in Solvents Versus Gas Phase: A Case Study with Phenol on Pt(111) in Water. *ACS Catal.* **9**, 8116–8127 (2019).

124. Villegas, I. & Weaver, M. J. Progressive cation solvation at Pt(111) model electrochemical interfaces in ultrahigh vacuum as probed by infrared spectroscopy and work-function measurements. *Electrochim. Acta* **41**, 661–673 (1996).

125. Baldelli, S., Mailhot, G., Ross, P., Shen, Y.-R. & Somorjai, G. A. Potential Dependent Orientation of Acetonitrile on Platinum (111) Electrode Surface Studied by Sum Frequency Generation. *J. Phys. Chem. B* **105**, 654–662 (2001).

126. Feng, G., Huang, J., Sumpter, B. G., Meunier, V. & Qiao, R. Structure and dynamics of electrical double layers in organic electrolytes. *Phys. Chem. Chem. Phys.* **12**, 5468–5479 (2010).

127. Pavlov, S. V & Kislenko, S. A. Effects of carbon surface topography on the electrode/electrolyte interface structure and relevance to Li–air batteries. *Phys. Chem. Chem. Phys.* **18**, 30830–30836 (2016).

128. Foley, J. K., Korzeniewski, C. & Pons, S. Anodic and cathodic reactions in acetonitrile / tetra-n-butylammonium tetrafluoroborate: an electrochemical and infrared spectroelectrochemical study. *Can. J. Chem.* **66**, 201–206 (1988).

129. Kiss, L. Electrooxidation of low-permittivity solvents in acetonitrile and solubility of trihexylamine in acetonitrile. *J. Iran. Chem. Soc.* **17**, 67–71 (2020).

130. Markovits, A. & Minot, C. Theoretical study of the acetonitrile flip-flop with the electric field orientation: adsorption on a Pt (111) electrode surface. *Catal. Letters* **91**, 225–234 (2003).

131. Shayeghi, A. *et al.* Adsorption of Acetonitrile, Benzene, and Benzonitrile on Pt(111): Single Crystal Adsorption Calorimetry and Density Functional Theory. *J. Phys. Chem. C* **121**, 21354–21363 (2017).

132. Pasti, I. A., Markovic, A., Gavrilov, N. & Mentus, S. V. Adsorption of Acetonitrile on Platinum and its Effects on Oxygen Reduction Reaction in Acidic Aqueous Solutions — Combined Theoretical and Experimental Study. *Electrocatalysis* **7**, 235–248 (2016).

133. Lytken, O., Lew, W. & Campbell, C. T. Catalytic reaction energetics by single crystal adsorption calorimetry: hydrocarbons on Pt(111). *Chem. Soc. Rev.* **37**, 2172–2179 (2008).

134. Acree, Jr., W. E. & Chickos, J. S. Phase Transition Enthalpy Measurements of Organic and Organometallic Compounds. in *NIST Standard Reference Database Number 69* (eds. Linstrom, P. J. & Mallard, W. G.) (National Institute of Standards and Technology, 2021).

135. Domalski, E. S. & Hearing, E. D. Heat Capacities and Entropies of Organic Compounds in the Condensed Phase. Volume III. *J. Phys. Chem. Ref. Data* **25**, 1 (1996).

136. Yaws, C. L. *Yaws' Handbook of Thermodynamic and Physical Properties of Chemical Compounds*. (Knovel, 2003).

137. Garwood Jr., G. A. & Hubbard, A. T. Superlattices formed by interaction of polar solvents with Pt(111) surfaces studied by LEED, Auger spectroscopy and thermal desorption mass spectrometry. *Surf. Sci.* **118**, 223–247 (1982).

138. Gardin, D. E., Barbieri, A., Batteas, J. D., Van Hove, M. A. & Somorjai, G. A. Tensor LEED analysis of the Ni(111)-p(2x2)-CH3CN structure. *Surf. Sci.* **304**, 316–324 (1994).

139. Ou, E. C., Young, P. A. & Norton, P. R. Interaction of acetonitrile with platinum (111): more properties of the n2(C,N) state and new species in the submonolayer. *Surf. Sci.* **277**, 123–131 (1992).

140. Sexton, B. A. & Avery, N. R. Coordination of acetonitrile (CH3CN) to Platinum (111): evidence for an n2 (C,N) species. *Surf. Sci.* **129**, 21–36 (1983).

141. Waldrup, S. B. & Williams, C. T. Acetonitrile Adsorption on Polycrystalline Platinum: An In Situ Investigation Using Sum Frequency Spectroscopy. *J. Phys. Chem. C* **112**, 219–226

(2008).

142. Haynes, W. M., Lide, D. R. & Bruno, T. J. *CRC Handbook of Chemistry and Physics*. (CRC Press, 2016).

143. Singh, N. & Campbell, C. T. A Simple Bond-Additivity Model Explains Large Decreases in Heats of Adsorption in Solvents Versus Gas Phase: A Case Study with Phenol on Pt(111) in Water. (2019). doi:10.1021/acscatal.9b01870

144. Tait, S. L., Dohnálek, Z., Campbell, C. T. & Kay, B. D. N -alkanes on Pt(111) and on C (0001) Pt (111): Chain length dependence of kinetic desorption parameters. *J. Chem. Phys.* **125**, 1–15 (2006).

145. Lew, W., Lytken, O., Farmer, J. A., Crowe, M. C. & Campbell, C. T. Improved pyroelectric detectors for single crystal adsorption calorimetry from 100 to 350 K. *Rev. Sci. Instrum.* **81**, (2010).

146. Lytken, O. *et al.* Energetics of cyclohexene adsorption and reaction on Pt(111) by low-temperature microcalorimetry. *J. Am. Chem. Soc.* **130**, 10247–10257 (2008).

147. Lytken, O., Lew, W. & Campbell, C. T. Catalytic reaction energetics by single crystal adsorption calorimetry: hydrocarbons on Pt(111). *Chem. Soc. Rev.* **37**, 2172–2179 (2008).

148. Ni, B., Zhang, T., Li, J., Li, X. & Gao, H. Topological Design of Graphene. in *Handbook of Graphene* (Wiley, 2019).

149. Cusati, T. *et al.* Electrical properties of graphenemetal contacts. *Sci. Rep.* **7**, (2017).

150. Mallion, R. B. & Rouvray, D. H. The Golden Jubilee of the Coulson-Rushbrooke Pairing Theorem. *J. Math. Chem.* **5**, 1–21 (1990).

151. Coulson, C. A. & Rushbrooke, G. S. Note on the Method of Molecular Orbitals. *Math. Proc. Cambridge Philos. Soc.* **36**, 193–200 (1940).

152. Xin, H. & Gao, X. Application of Azulene in Constructing Organic Optoelectronic Materials: New Tricks for an Old Dog. *Chempluschem* **82**, 945–956 (2017).

153. Koch, N. Organic electronic devices and their functional interfaces. *Chem. Phys. Chem.* **8**, 1438–1455 (2007).

154. Stuckless, J. T., Frei, N. A. & Campbell, C. T. A novel single-crystal adsorption calorimeter and additions for determining metal adsorption and adhesion energies. *Rev. Sci. Instrum.* **69**, 2427–2438 (1998).

155. Silbaugh, T. L. & Campbell, C. T. Energies of Formation Reactions Measured for Adsorbates on Late Transition Metal Surfaces. *J. Phys. Chem. C* **120**, 25161–25172 (2016).

156. Solomonov, B. N. *et al.* Solution calorimetry as a complementary tool for the determination of enthalpies of vaporization and sublimation of low, volatile compounds at 298.151 K. *Thermochim. Acta* **589**, 164–173 (2014).

157. Kovats, E., Gunthard, H. & Plattner, A. Thermische Eigenschaften von Azulenen. *Helv.*

Chim. Acta (1955).

158. Chickos, J., Hesse, D., Hosseini, S., Nichols, G. & Webb, P. Sublimation enthalpies at 298.15 K using correlation gas chromatography and differential scanning calorimetry measurements. *Thermochim. Acta* **313**, 101–110 (1998).

159. Maurer, R. J., Ruiz, V. G. & Tkatchenko, A. Many-body dispersion effects in the binding of adsorbates on metal surfaces. *J. Chem. Phys.* **143**, (2015).

160. Maurer, R. J. *et al.* Adsorption structures and energetics of molecules on metal surfaces: Bridging experiment and theory. *Prog. Surf. Sci.* **91**, 72–100 (2016).

161. Ihm, H., Ajo, H. M., Gottfried, J. M., Bera, P. & Campbell, C. T. Calorimetric Measurement of the Heat of Adsorption of Benzene on Pt(111). *J. Phys. Chem. B* **108**, 14627–14633 (2004).

162. Karp, E. M., Silbaugh, T. L. & Campbell, C. T. Energetics of Adsorbed CH3 and CH on Pt(111) by Calorimetry. *J. Phys. Chem. C* **135**, 5208–5211 (2013).

163. Lynch, I. *et al.* The nanoparticle–protein complex as a biological entity; a complex fluids and surface science challenge for the 21st century. *Adv. Colloid Interface Sci.* **134**–**135**, 167–174 (2007).

164. Kasemo, B. Biological surface science. *Surf. Sci.* **500**, 656–677 (2002).

165. Barth, J. V, Costantini, G. & Kern, K. Engineering atomic and molecular nanostructures at surfaces. in *Nanoscience and Technology* 67–75 doi:10.1142/9789814287005_0008

166. Sarikaya, M., Tamerler, C., Jen, A. K.-Y., Schulten, K. & Baneyx, F. Molecular biomimetics: nanotechnology through biology. *Nat. Mater.* **2**, 577–585 (2003).

167. Pradhan, S., Reddy, A. S., Devi, R. N. & Chilukuri, S. Copper-based catalysts for water gas shift reaction: Influence of support on their catalytic activity. *Catal. Today* **141**, 72–76 (2009).

168. Babar, S. & Weaver, J. H. Optical constants of Cu, Ag, and Au revisited. *Appl. Opt.* **54**, 477–481 (2015).

169. Weaver, J. H., Krafka, C., Lynch, D. W. & Koch, E. E. Optical properties of metals. *Appl. Opt.* **20**, 1124_1--1125 (1981).

170. Marcinkowski, M. D. *et al.* Microscopic View of the Active Sites for Selective Dehydrogenation of Formic Acid on Cu(111). *ACS Catal.* **5**, 7371–7378 (2015).

171. Shiozawa, Y., Koitaya, T., Mukai, K., Yoshimoto, S. & Yoshinobu, J. Quantitative analysis of desorption and decomposition kinetics of formic acid on Cu(111): The importance of hydrogen bonding between adsorbed species. *J. Chem. Phys.* **143**, 234707 (2015).

172. Sotiropoulos, A., Milligan, P. K., Cowie, B. C. C. & Kadodwala, M. A structural study of formate on Cu(111). *Surf. Sci.* **444**, 52–60 (2000).

173. Wuhn, M., Weckesser, J. & Woll, C. Bonding and Orientational Ordering of Long-Chain

Carboxylic Acids on Cu(111): Investigations Using X-ray Absorption Spectroscopy. *Langmuir* **17**, 7605–7612 (2001).

174. Nakano, H., Nakamura, I., Fujitani, T. & Nakamura, J. Structure-Dependent Kinetics for Synthesis and Decomposition of Formate Species over Cu(111) and Cu(110) Model Catalysts. *J. Phys. Chem. B* **105**, 1355–1365 (2001).

175. Stone, P., Poulston, S., Bennett, R. A., Price, N. J. & Bowker, M. An STM, TPD and XPS investigation of formic acid adsorption on the oxygen-precovered c(6×2) surface of Cu(110). *Surf. Sci.* **418**, 71–83 (1998).

176. Nishimura, H., Yatsu, T., Fujitani, T., Uchijima, T. & Nakamura, J. Synthesis and decomposition of formate on a Cu(111) surface — kinetic analysis. *J. Mol. Catal. A Chem.* **155**, 3–11 (2000).

177. Pöllmann, B. S., Bayer, A., Ammon, C. & Steinrück, H. Adsorption and Reaction of Methanol on Clean and Oxygen Precovered Cu(111). *Z. Phys. Chem.* **218**, 957–971 (2004).

178. Kolovos-Vellianitis, D., Kammler, T. & Kuppers, J. Interaction of gaseous hydrogen atoms with oxygen covered Cu(100) surfaces. *Surf. Sci.* **485**, 166–170 (2001).

179. Bange, K., Grider, D. E., Madey, T. E. & Sass, J. K. The surface chemistry of H2O on clean and oxygen-covered Cu(110). *Surf. Sci.* **136**, 38–64 (1984).

180. Clendening, W. D., Rodriguez, J. A., Campbell, J. M. & Campbell, C. T. The Chemisorption and Coadsorption of Water and Oxygen on Cs-Dosed Cu(110). *Surf. Sci.* **216**, 429–461 (1989).

181. Habraken, F. H. P. M., Kieffer, E. P. & Bootsma, G. A. A study of the kinetics of the interactions of O2 and N2O with a Cu(111) surface and of the reaction of CO with adsorbed oxygen using AES, LEED and ellipsometry. *Surf. Sci.* **83**, 45–59 (1979).

182. Stephenson, R. M. & Malanowski, S. *Handbook of the thermodynamics of organic compounds*. (Elsevier, 1987).

183. Campbell, C. T. & Sellers, J. R. V. Enthalpies and Entropies of Adsorption on Well-Defined Oxide Surfaces: Experimental Measurements. *Chem. Rev.* **113**, 4106–4135 (2013).

184. Dell, R. M., Stone, F. S. & Tiley, P. F. The Adsorption of Oxygen and other Gases on Copper. *Trans. Faraday Soc.* **49**, 195–201 (1953).

185. Giamello, E., Fubini, B., Lauro, P. & Bossi, A. A Microcalorimetric Method for the Evaluation of Copper Surface Area in Cu-ZnO Catalyst. *J. Catal.* **87**, 443–451 (1984).

186. Wang, Y., Yan, L. & Wang, G. Oxygen-assisted water partial dissociation on copper: a model study. *Phys. Chem. Chem. Phys.* **17**, 8231–8238 (2015).

187. Luo, Y.-R. *Comprehensive Handbook of Chemical Bond Energies*. (CRC Press, 2007).

188. Ohtani, T. *et al.* IRAS and TPD study of adsorbed formic acid on Pt(110)-(1x2) surface. *Surf. Sci.* **368**, 270–274 (1996).

189. Chapman, D. The infrared spectra of liquid and solid formic acid. *J. Chem. Soc.* 225–229 (1956).

190. Redhead, P. A. Thermal Desorption of Gases. *Vacuum* 203–211 (1962).

191. Singh, U. K. & Vannice, M. A. Kinetics of liquid-phase hydrogenation reactions over supported metal catalysts - a review. *Appl. Catal. A Gen.* **213**, 1–24 (2001).

192. Weber, R. S. & Holladay, J. E. Modularized Production of Value-Added Products and Fuels from Distributed Waste Carbon-Rich Feedstocks. *Engineering* **4**, 330–335 (2018).

193. Cantu, D. C. *et al.* Combined Experimental and Theoretical Study on the Activity and Selectivity of the Electrocatalytic Hydrogenation of Aldehydes. *ACS Catal.* **8**, 7645–7658 (2018).

194. Lin, S. D. & Vannice, M. A. Hydrogenation of Aromatic Hydrocarbons over Supported Pt Catalysts. *J. Catal.* **143**, 539–553 (1993).

195. Yoon, Y., Rousseau, R., Weber, R. S., Mei, D. & Lercher, J. A. First-Principles Study of Phenol Hydrogenation on Pt and Ni Catalysts in Aqueous Phase. *J. Am. Chem. Soc.* **136**, 10287–10298 (2014).

196. Lessard, J. Electrocatalytic Hydrogenation. in *Organic Electrochemistry, Fifth Edition* 1657–1672 (CRC Press, 2015). doi:doi:10.1201/b19122-53

197. Bannari, A., Proulx, P., Menard, H. & Cirtiu, C. M. Mathematical modeling of the kinetics of phenol electrocatalytic hydrogenation over supported Pd-alumina catalyst. *Appl. Catal. A Gen.* **345**, 28–42 (2008).

198. Singh, N. *et al.* Electrocatalytic Hydrogenation of Phenol over Platinum and Rhodium: Unexpected Temperature Effects Resolved. *ACS Catal.* **6**, 7466–7470 (2016).

199. Sanyal, U., Lopez-Ruiz, J., Padmaperuma, A. B., Holladay, J. & Gutierrez, O. Y. Electrocatalytic Hydrogenation of Oxygenated Compounds in Aqueous Phase. *Org. Process Res. Dev.* **22**, 1590–1598 (2018).

200. Singh, N. *et al.* Carbon-supported Pt during aqueous phenol hydrogenation with and without applied electrical potential : X-ray absorption and theoretical studies of structure and adsorbates. *J. Catal.* **368**, 8–19 (2018).

201. Song, Y., Gutiérrez, O. Y., Herranz, J. & Lercher, J. A. Aqueous phase electrocatalysis and thermal catalysis for the hydrogenation of phenol at mild conditions. *Appl. Catal. B Environ.* **182**, 236–246 (2016).

202. Li, G., Han, J., Wang, H., Zhu, X. & Ge, Q. Role of dissociation of phenol in its selective hydrogenation on Pt(111) and Pd(111). *ACS Catal.* **5**, 2009–2016 (2015).

203. Lopez-Ruiz, J. A., Sanyal, U., Egbert, J., Gutierrez, O. Y. & Holladay, J. Kinetic Investigation of the Sustainable Electrocatalytic Hydrogenation of Benzaldehyde on Pd/C: Effect of Electrolyte Composition and Half-Cell Potentials. *ACS Sustain. Chem. Eng.* **6**, 16073–16085 (2018).

204. Song, Y., Chia, S. H., Sanyal, U., Guti??rrez, O. Y. & Lercher, J. A. Integrated catalytic

and electrocatalytic conversion of substituted phenols and diaryl ethers. *J. Catal.* **344**, 263–272 (2016).

205. Ravel, B. & Newville, M. ATHENA, ARTEMIS, HEPHAESTUS: data analysis for X-ray absorption spectroscopy using IFEFFIT. *J. Synchrotron Radiat.* **12**, 537–541 (2005).

206. Newville, M. IFEFFIT: interactive XAFS analysis and FEFF fitting. *J. Synchrotron Radiat.* **8**, 322–324 (2001).

207. Rehr, J. J., Kas, J. J., Vila, F. D., Prange, M. P. & Jorissen, K. Parameter-free calculations of X-ray spectra with FEFF9. *Phys. Chem. Chem. Phys.* **12**, 5503–5513 (2010).

208. Song, Y., Gutiérrez, O. Y., Herranz, J. & Lercher, J. A. Aqueous phase electrocatalysis and thermal catalysis for the hydrogenation of phenol at mild conditions. *Appl. Catal. B Environ.* (2016). doi:10.1016/j.apcatb.2015.09.027

209. Tew, M. W., Miller, J. T. & van Bokhoven, J. A. Particle Size Effect of Hydride Formation and Surface Hydrogen Adsorption of Nanosized Palladium Catalysts: L-3 Edge vs K Edge X-ray Absorption Spectroscopy. *J. Phys. Chem. C* **113**, 15140–15147 (2009).

210. Bugaev, A. L. *et al.* Core-Shell Structure of Palladium Hydride Nanoparticles Revealed by Combined X-ray Absorption Spectroscopy and X-ray Diffraction. *J. Phys. Chem. C* **121**, 18202–18213 (2017).

211. Bugaev, A. L. *et al.* In situ formation of hydrides and carbides in palladium catalyst: When XANES is better than EXAFS and XRD. *Catal. Today* **283**, 119–126 (2017).

212. Sheng, W. *et al.* Electrochemical reduction of CO2 to synthesis gas with controlled CO/H2 ratios. *Energy Environ. Sci.* **10**, 1180–1185 (2017).

213. Bugaev, A. L. *et al.* Temperature- and pressure-dependent hydrogen concentration in supported PdHx nanoparticles by Pd K-edge X-ray absorption spectroscopy. *J. Phys. Chem. C* **118**, 10416–10423 (2014).

214. Chase, Z. A. *et al.* State of supported Pd during catalysis in water. *J. Phys. Chem. C* **117**, 17603–17612 (2013).

215. Johansson, M. *et al.* Hydrogen adsorption on palladium and palladium hydride at 1 bar. *Surf. Sci.* **604**, 718–729 (2010).

216. Wilde, M., Fukutani, K., Naschitzki, M. & Freund, H.-J. Hydrogen absorption in oxide-supported palladium nanocrystals. *Phys. Rev. B - Condens. Matter Mater. Phys.* **77**, 113412 (2008).

217. Frenkel, A. I., Hills, C. W. & Nuzzo, R. G. A view from the inside: Complexity in the atomic scale ordering of supported metal nanoparticles. *J. Phys. Chem. B* **105**, 12689–12703 (2001).

218. Campbell, C. T. Ultrathin metal films and particles on oxide surfaces: Structural, electronic and chemisorptive properties. *Surf. Sci. Rep.* **27**, 1–111 (1997).

219. Campbell, C. T. & Sellers, J. R. V. Anchored metal nanoparticles: Effects of support and size on their energy, sintering resistance and reactivity. *Faraday Discuss.* **162**, 9–30

(2013).

220. Bugaev, A. L. *et al.* Time-resolved operando studies of carbon supported Pd nanoparticles under hydrogenation reactions by X-ray diffraction and absorption. *Faraday Discuss.* **208**, 187–205 (2018).

221. Feenstra, R., Griessen, R. & de Groot, D. G. Hydrogen induced lattice expansion and effective H-H interaction in single phase PdHc. *J. Phys. F Met. Phys.* **16**, 1933–1952 (1986).

222. Shinagawa, T., Garcia-Esparza, A. T. & Takanabe, K. Insight on Tafel slopes from a microkinetic analysis of aqueous electrocatalysis for energy conversion. *Sci. Rep.* **5**, (2015).

223. Zheng, J., Sheng, W., Zhuang, Z., Xu, B. & Yan, Y. Universal dependence of hydrogen oxidation and evolution reaction activity of platinum-group metals on pH and hydrogen binding energy. *Sci. Adv.* **2**, e1501602 (2016).

224. Hansen, R. S. & Clampitt, B. H. The Apparent Adsorption of Some Aliphatic Compounds from Aqueous Solutions as Inferred from Hydrogen Overvoltage Measurements. *J. Phys. Chem.* **58**, 908–911 (1954).

225. Davis, M. E. & Davis, R. J. *Fundamentals of Chemical Reaction Engineering*. (2003).

226. Yang, G. *et al.* The Nature of Hydrogen Adsorption on Platinum in the Aqueous Phase. *Angew. Chemie - Int. Ed.* **58**, 3527–3532 (2019).

227. Gómez, R., Orts, J. M., Álvarez-Ruiz, B. & Feliu, J. M. Effect of Temperature on Hydrogen Adsorption on Pt(111), Pt(110), and Pt(100) Electrodes in 0.1 M $HClO_4$. *J. Phys. Chem. B* **108**, 228–238 (2004).

228. Norskov, J. K. *et al.* Trends in the exchange current for hydrogen evolution. *J. Electrochem. Soc.* **152**, J23–J26 (2005).

229. Christmann, K. Interaction of hydrogen with solid surfaces. *Surf. Sci. Rep.* **9**, 1–163 (1988).

230. Villalba, M., Bossi, M. L. & Calvo, E. J. Selective electrocatalytic hydrogenation using palladium nanoparticles electrochemically formed in layer-by-layer multilayer films. *Phys. Chem. Chem. Phys.* **17**, 10086–10092 (2015).

231. Gautier, S. & Sautet, P. Coadsorption of Butadiene and Hydrogen on the (111) Surfaces of Pt and Pt2Sn Surface Alloy: Understanding the Cohabitation from First-Principles Calculations. *J. Phys. Chem. C* **121**, 25152–25163 (2017).

232. Salmeron, M. & Somorjai, G. A. Adsorption and bonding of butane and pentane on the Pt(111) crystal surface: effects of oxygen treatments and deuterium preadsorption. *J. Phys. Chem.* **85**, 3835–3840 (1981).

233. Salmeron, M. & Somorjai, G. A. Desorption, decomposition, and deuterium exchange reactions of unsaturated hydrocarbons (ethylene, acetylene, propylene, and butenes) on the Pt(111) crystal face. *J. Phys. Chem.* **86**, 341–350 (1982).

234. Campbell, J. M., Seimanides, S. & Campbell, C. T. Probing ensemble effects in surface reactions 2. benzene adsorption on clean and bismuth-covered Pt(111). *J. Phys. Chem.* **93**, 815–826 (1989).

235. Bondue, C. J. & Koper, M. T. M. Electrochemical Reduction of the Carbonyl Functional Group: The Importance of Adsorption Geometry, Molecular Structure, and Electrode Surface Structure. *J. Am. Chem. Soc.* **141**, 12071–12078 (2019).

236. Bondue, C. J., Calle-Vallejo, F., Figueiredo, M. C. & Koper, M. T. M. Structural principles to steer the selectivity of the electrocatalytic reduction of aliphatic ketones on platinum. *Nat. Catal.* **2**, 243–250 (2019).

237. Vannice, M. A., Erley, W. & Ibach, H. A RAIRS and HREELS study of acetone on Pt(111). *Surf. Sci.* **254**, 1–11 (1991).

238. Moore, J. C., Battino, R., Rettich, T. R., Handa, Y. P. & Wilhelm, E. Partial Molar Volumes of "Gases" at Infinite Dilution in Water at 298.15 K. *J. Chem. Eng. Data* **27**, 22–24 (1982).

239. Henke, B. L., Gullikson, E. M. & Davis, J. C. X-ray interactions: photoabsorption, scattering, transmission, and reflection at E=50-30000 eV, Z=1-92. *At. Data Nucl. Data Tables* **54**, 181–342 (1993).

240. Zalineeva, A., Baranton, S., Coutanceau, C. & Jerkiewicz, G. Electrochemical behavior of unsupported shaped palladium nanoparticles. *Langmuir* **31**, 1605–1609 (2015).

241. Bhowmik, T., Kundu, M. K. & Barman, S. Palladium Nanoparticle-Graphitic Carbon Nitride Porous Synergistic Catalyst for Hydrogen Evolution/Oxidation Reactions over a Broad Range of pH and Correlation of Its Catalytic Activity with Measured Hydrogen Binding Energy. *ACS Catal.* **6**, 1929–1941 (2016).

242. Gabrielli, C., Grand, P. P., Lasia, A. & Perrot, H. Investigation of Hydrogen Adsorption and Absorption in Palladium Thin Films II. Cyclic Voltammetry. *J. Electrochem. Soc.* **151**, A1943 (2004).

243. Jaksic, M. M., Johansen, B. & Tunold, R. Electrochemical behaviour of palladium in acidic and alkaline solutions of heavy and regular water. *Int. J. Hydrogen Energy* **18**, 91–110 (1993).

244. Jerkiewicz, G. *et al.* Underpotential Deposition of Hydrogen on Benzene-Modified Pt(111) in Aqueous H2SO4. *Langmuir* **21**, 3511–3520 (2005).

245. Obradović, M. D., Lessard, J. & Jerkiewicz, G. Cyclic-voltammetry behavior of Pt(1 1 1) in aqueous HClO4 + C6H6: Influence of C6H6 concentration, scan rate and temperature. *J. Electroanal. Chem.* **649**, 248–256 (2010).

246. Davis, R. J., Landry, S. M., Horsley, J. A. & Boudart, M. X-ray-absorption study of the interaction of hydrogen with clusters of supported palladium. *Phys. Rev. B* **39**, 10580–10583 (1989).

247. Agostini, G. *et al.* Determination of the particle size, available surface area, and nature of exposed sites for silica-alumina-supported Pd nanoparticles: A multitechnical approach. *J.*

Phys. Chem. C **113**, 10485–10492 (2009).

248. McCaulley, J. A. In-situ x-ray absorption spectroscopy studies of hydride and carbide formation in supported palladium catalysts. *J. Phys. Chem.* **97**, 10372–10379 (1993).

249. Gabrielli, C., Grand, P. P., Lasia, A. & Perrot, H. Investigation of Hydrogen Adsorption and Absorption in Palladium Thin Films III. Impedance Spectroscopy. *J. Electrochem. Soc.* **151**, A1943–A1949 (2004).

250. Bai, L., Harrington, D. A. & Conway, B. E. Behavior of overpotential-deposited species in Faradaic reactions-II. ac Impedance measurements on H2 evolution kinetics at activated and unactivated Pt cathodes. *Electrochim. Acta* **32**, 1713–1731 (1987).

251. Harrington, D. A. & Conway, B. E. ac Impedance of Faradaic reactions involving electrosorbed intermediates—I. Kinetic theory. *Electrochim. Acta* **32**, 1703–1712 (1987).

252. Villalba, M., Del Pozo, M. & Calvo, E. J. Electrocatalytic hydrogenation of acetophenone and benzophenone using palladium electrodes. *Electrochim. Acta* **164**, 125–131 (2015).

Vita

Griffin Ruehl grew up in Sherwood, Oregon and went to Montana State University for his undergraduate studies. While there, he conducted research under the guidance of Dr. Stephen Sofie and Dr. Stephanie Wettstein, in various project exploring materials synthesis, catalysis, and biomass chemistry with applications in clean energy. He graduated in 2016 with a Bachelor of Science in Chemical Engineering, a Bachelor of Arts in Liberal Studies – Global and Multicultural Studies option, and an honors degree from the MSU Honors College. He specialized his global and multicultural studies degree in east Asian studies after studying abroad in Chiang Mai, Thailand.

He came to the University of Washington for graduate studies in Chemical Engineering in 2016, and joined the group of Dr. Charles T. Campbell. He initially conducted research in collaboration with the Chemical Transformations Initiative at Pacific Northwest National Laboratory, focusing on correlating molecular structure of representative molecules for biomass intermediates with observed trends and differences in catalytic activity on late-transition metal surfaces. He later shifted his focus to working on the single crystal adsorption calorimeter, Cal2, which has constituted the majority of his PhD research. This research has focused on the energetics of adsorption of molecules and molecular fragments on Pt(111) and Cu(111). He has been particularly interested in systems that are relevant to emergent technologies in clean energy and sustainability broadly.

Outside of the lab, Griffin has been involved in GRID, a student organization focused on developing best practices in off-grid solar installations for energy access and disaster recovery, with a focus on environmental justice and ethical practices. As part of this he coordinated and participated in two trips to several regions of Guatemala to install and study off-grid, single-

home solar systems. He eventually transitioned into the lead officer role and coordinated and managed multiple remote projects during the pandemic, including the development of a educational module in coding that was successfully run in partnership with a solar vocational training facility in Cameroon. He has also sat as the graduate representative for the Diversity, Equity, and Inclusion committee in the Chemical Engineering department, along with other similar focused efforts around campus. He also served as a teaching assistant for General Chemistry (162), Chemical Engineering Unit Operations Lab (436), Chemical Engineering Senior Design (485) twice, and Separations (435). He has authored two white papers, the first on utility side solutions for decreasing the grid impact of rapid charging of electric vehicles for the Seattle Chamber of Commerce, and the second on different carbon tax legislative measures put forth by the Washington State legislature for the Clean Energy Alliance.

Outside of lab Griffin enjoys getting out into the nature of the Pacific NW with his partner Tyler and their two dogs, Frankie and Blu. He enjoys exploring the intersections of culture, chemistry, sociology, and botany, and has become even more of an avid reader and gardener over the course of the pandemic.